

DEPARTMENT OF PHYSICS, UNIVERSITY OF JYVÄSKYLÄ

**JET TRANSVERSE MOMENTUM DISTRIBUTIONS  
MEASURED BY ALICE**

**BY  
TOMAS SNELLMAN**

PHD thesis

Supervisors: Jan Rak, Dong Jo Kim

Jyväskylä, Finland  
December, 2018

## **3** Contents

<b>4</b>	<b>1</b>	<b>Introduction</b>	<b>7</b>
5	1.1	Quantum chromodynamics . . . . .	8
6	1.1.1	Foundation of QCD . . . . .	8
7	1.1.2	Asymptotic Freedom . . . . .	9
8	1.2	Heavy ion physics . . . . .	13
9	1.2.1	History . . . . .	13
10	1.3	Features of Heavy-Ion Collisions . . . . .	15
11	1.3.1	Collision Geometry . . . . .	15
12	1.3.2	Nuclear Geometry . . . . .	16
13	1.3.3	Hydrodynamical Modelling . . . . .	19
14	1.4	Flow . . . . .	22
15	1.4.1	Anisotropic Flow . . . . .	23
16	1.4.2	High $p_T$ Phenomena . . . . .	24
17	1.5	Hard processes . . . . .	25
18	1.5.1	pQCD factorization . . . . .	25
19	1.5.2	Jet hadronisation . . . . .	27
20	1.5.3	Jet energy loss . . . . .	31
21	1.5.4	New paradigm of jet Quenching . . . . .	36
22	1.6	QGP in Small systems . . . . .	38
23	1.6.1	Collective phenomena . . . . .	38
24	1.6.2	Absence of jet quenching . . . . .	39
25	1.6.3	Centrality determination in small systems . . . . .	40
26	<b>2</b>	<b>Experimental Details</b>	<b>48</b>
27	2.1	CERN . . . . .	48
28	2.2	Large Hadron Collider . . . . .	48
29	2.2.1	LHC experiments . . . . .	50
30	2.3	ALICE . . . . .	51
31	2.3.1	Tracking . . . . .	52
32	2.3.2	TPC . . . . .	53
33	2.3.3	TPC upgrade . . . . .	54
34	2.3.4	Optical scanning . . . . .	56
35	2.3.5	Particle identification . . . . .	58
36	2.3.6	Electromagnetic Calorimeter . . . . .	59
37	2.3.7	Forward detectors . . . . .	59

38	2.3.8 Muon spectrometer . . . . .	61
39	2.3.9 Trigger . . . . .	61
40	<b>3 Event and track selection</b>	<b>62</b>
41	3.1 statistics . . . . .	63
42	<b>4 Analysis method</b>	<b>64</b>
43	4.1 Jet Finding . . . . .	64
44	4.1.1 Anti $k_T$ algorithm . . . . .	64
45	4.2 $j_T$ . . . . .	65
46	4.3 Unfolding . . . . .	67
47	4.3.1 Bayesian unfolding . . . . .	67
48	4.3.2 Toy Monte Carlo . . . . .	69
49	4.3.3 Pythia Response matrices . . . . .	70
50	4.3.4 Unfolding algorithm . . . . .	71
51	4.3.5 Unfolding closure test . . . . .	71
52	4.4 Background . . . . .	72
53	4.4.1 Perpendicular cone background . . . . .	73
54	4.4.2 Random background . . . . .	73
55	4.4.3 Auto-correlations . . . . .	76
56	4.4.4 Background methods . . . . .	76
57	4.5 Fitting . . . . .	77
58	<b>5 Systematic errors</b>	<b>79</b>
59	5.1 Background . . . . .	79
60	5.2 Unfolding . . . . .	81
61	5.2.1 Effect of number of iterations . . . . .	81
62	5.2.2 Effect of different prior . . . . .	81
63	5.2.3 Effect of $p_T$ truncation . . . . .	83
64	5.3 Tracking . . . . .	83
65	5.4 EMCAL . . . . .	83
66	5.5 Summary . . . . .	84
67	5.6 Comparison between A and C side . . . . .	85
68	5.7 Subtracted signal . . . . .	85
69	5.8 Combining systematics . . . . .	85
70	<b>6 Results</b>	<b>88</b>
71	6.1 Fitting . . . . .	88
72	6.1.1 RMS values from fitted distributions . . . . .	88
73	6.2 High multiplicity . . . . .	88

<sup>74</sup>	<b>7</b>	<b>Discussion</b>	<b>91</b>
<sup>75</sup>	7.1	Dihadron $j_T$ . . . . .	91
<sup>76</sup>	7.2	Comparing to dihadron and jet $j_T$ results . . . . .	92
<sup>77</sup>	7.2.1	Different $R$ parameters . . . . .	93
<sup>78</sup>	7.2.2	Leading tracks versus jet . . . . .	94
<sup>79</sup>	<b>8</b>	<b>Summary</b>	<b>96</b>

## <sup>80</sup> List of Figures

<sup>81</sup>	1	QCD phase diagram . . . . .	11
<sup>82</sup>	2	$\eta/s$ vs $(T - T_c)/T_c$ . . . . .	12
<sup>83</sup>	3	The definitions of the Reaction Plane and Participant Plane coordinate systems . . . . .	15
<sup>84</sup>	4	Interaction between partons in central and peripheral collisions. . . . .	16
<sup>85</sup>	5	An illustration of the multiplicity distribution in ALICE measurement with centrality classes. . . . .	17
<sup>86</sup>	6	The results of one Glauber Monte Carlo simulation. . . . .	20
<sup>87</sup>	7	Schematic representation of a heavy-ion collision . . . . .	21
<sup>88</sup>	8	Charged particle spectra . . . . .	22
<sup>89</sup>	9	Illustration of flow in momentum space in central and peripheral collisions. . . . .	23
<sup>90</sup>	10	QCD Leading Order . . . . .	25
<sup>91</sup>	11	Hard scattering . . . . .	25
<sup>92</sup>	12	Jet showering . . . . .	26
<sup>93</sup>	15	Measurements of the nuclear modification factor $R_{AA}$ in central heavy-ion collisions . . . . .	32
<sup>94</sup>	16	A comparison between observed $R_{AA}(\Delta\phi, p_T)$ and $R_{AA}$ using $v_2$ . . . . .	33
<sup>95</sup>	17	Elliptic flow, $v_2$ from $p_T = 1$ to 60 GeV/c . . . . .	42
<sup>96</sup>	18	Photon spectrum . . . . .	43
<sup>97</sup>	20	Calculations of the initial energy density in small collision systems at RHIC and the resulting hydrodynamic evolution. . . . .	45
<sup>98</sup>	21	Two-particle correlation results in PbPb, pPb, and pp collisions at the LHC []. . . . .	45
<sup>99</sup>	22	RpA in proton-lead collisions . . . . .	45
<sup>100</sup>	23	Distribution of the sum of amplitudes in the V0A hodoscopes (Pb-going), as well as the NBD-Glauber fit (explained in the text). Centrality classes are indicated by vertical lines. The inset shows a zoom-in on the most peripheral events. [1] . . . . .	46

110	24	Top: Scatter plot of number of participating nucleons versus impact parameter; Bottom: Scatter plot of multiplicity versus the number of participating nucleons from the Glauber fit for V0A. The quantities are calculated with a Glauber Monte Carlo of p-Pb (left) and Pb-Pb (right) collisions. [1] . . . . .	47
115	25	CERN collider complex . . . . .	49
116	26	ALICE . . . . .	51
117	27	ITS . . . . .	52
118	28	TPC . . . . .	54
119	29	An example image taken of a GEM foil with false colors. . . . .	57
120	30	Illustration of $\vec{j}_T$ . The jet fragmentation transverse momentum, $\vec{j}_T$ , is defined as the transverse momentum component of the track momentum, $\vec{p}_{\text{track}}$ , with respect to the jet momentum, $\vec{p}_{\text{jet}}$ . . . . .	65
121	31	Inclusive $j_T$ with background . . . . .	66
124	32	Results from unfolding in Toy Monte Carlo . . . . .	70
125	33	Jet $p_T$ in unfolding closure test . . . . .	72
126	34	$j_T$ Response matrices in single jet $p_T$ bins . . . . .	73
127	35	Pythia closure test results. Fake tracks include also tracks that do exist in the true dataset, but for one reason or another were not given $j_T$ values. $j_T$ is only calculated for tracks that are associated with jets . . . . .	74
131	36	Background estimation . . . . .	75
132	37	Flowchart representation of the perpendicular cone background procedure . . . . .	75
134	38	$j_T$ background with two different methods . . . . .	77
135	39	$j_T$ signal with random bacgkround subtraction fits in different jet $p_T$ bins . . . . .	80
137	40	Differences between perpendicular cone and random background subtraction in the resulting RMS values. . . . .	80
139	41	Differences between Bayesian and SVD unfolding in the resulting RMS values . . . . .	81
141	42	Unfolding with different number of iterations . . . . .	82
142	43	Effect of changing minimum jet $p_T$ used in unfolding from 5 to 10 GeV . . . . .	82
144	44	Effect of changing minimum jet $p_T$ used in unfolding from 5 to 10 GeV . . . . .	83
146	45	Results from PYTHIA simulations with Cluster energies scale up/down by 2 %. Additionally jet momenta were scaled by 2 % when determining the jet $p_T$ bin. . . . .	84
149	46	Relative systematic errors resulting from cluster energy uncertainty.	84

150	47	Comparison of inclusive $j_T$ distributions between A and C side for minimum bias and EMCAL triggered data. . . . .	86
151	48	$j_T$ signal with background subtracted . . . . .	87
152	49	Comparison of the effect of background method on $j_T$ signal. . . . .	87
153	50	$j_T$ signal fits in different jet $p_T$ bins . . . . .	88
154	51	RMS values extracted from the fits for the gaussian (narrow) and inverse gamma (wide) components . . . . .	89
155	52	RMS values extracted from the fits for the gaussian (narrow) and inverse gamma (wide) components . . . . .	89
156	53	$j_T$ distributions for high multiplicity p-Pb events . . . . .	90
157	54	Dihadron $j_T$ results . . . . .	91
158	55	RMS values of the narrow and wide $j_T$ components in the dihadron correlation analysis. Results from pp collisions at $\sqrt{s} = 7$ TeV (circular symbols) and from p-Pb collisions at $\sqrt{s_{NN}} = 5.02$ TeV (square symbols) are compared to PYTHIA 8 tune 4C simulations at $\sqrt{s} = 7$ TeV (short dashed line) and at $\sqrt{s} = 5.02$ TeV (long dashed line). Different panels correspond to different $x_{\parallel}$ bins with $0.2 < x_{\parallel} < 0.4$ on the left, $0.4 < x_{\parallel} < 0.6$ in the middle, and $0.6 < x_{\parallel} < 1.0$ on the right. The statistical errors are represented by bars and the systematic errors by boxes. [2] . . . . .	92
159	56	Jet $j_T$ results are compared to results obtained in the dihadron analysis. Dihadron trigger $p_T$ bins are converted to jet $p_T$ bins using observed mean $p_{T,jet}$ values in $p_{T,trigger}$ bins. Dihadron results are for $0.2 < x_{\parallel} < 0.4$ . . . . .	93
160	57	Pythia $R$ parameters $j_T$ . . . . .	94
161	58	Pythia $R$ parameters RMS . . . . .	95
162	59	Results of calculating $j_T$ with respect to the jet axis or the leading hadron. The assumption is that because the leading hadron is an imperfect estimate of the jet axis, low $j_T$ tracks should on average be shifted to higher $j_T$ . . . . .	95

# 180 1 Introduction

181 REWRITE At sufficiently high energies quarks and gluons are no longer bound to  
182 hadrons, but they form a deconfined state known as Quark-Gluon plasma (QGP).  
183 The main goal of heavy ion physics is the study of QGP and its properties. One  
184 of the experimental observables that is sensitive to the properties of QGP is the  
185 azimuthal distribution of particles in the plane perpendicular to the beam direc-  
186 tion.

187 When nuclei collide at non-zero impact parameter (non-central collisions), their  
188 overlap region is asymmetric. This initial spatial asymmetry is converted via multi-  
189 ple collisions into an anisotropic momentum distribution of the produced particles.  
190 For low momentum particles ( $p_T \lesssim 3$  GeV/c), this anisotropy is understood to  
191 result from hydrodynamically driven flow of the QGP [3–7].

192 One way to characterize this anisotropy is with coefficients from a Fourier se-  
193 ries parametrization of the azimuthal angle distribution of emitted hadrons. The  
194 second order coefficient,  $v_2$  which is also known as elliptic flow, shows clear depen-  
195 dence on centrality. The collision geometry is mainly responsible for the elliptic  
196 flow. Higher harmonics don't depend that much on centrality. These higher har-  
197 monics carry information about the fluctuations in collisions. The event-by-event  
198 fluctuations have an increasing importance in measurements and it has been ob-  
199 served that measurements of elliptic flow in central collisions and measurements  
200 of higher order harmonics are consistent with the assumption that flow in these  
201 cases is mainly due to fluctuations [8].

202 At LHC energies  $\sqrt{s_{NN}} = 2.76\text{GeV}$  it has been observed that in general there  
203 is little difference to flow at RHIC energies. The  $v_2$  coefficient is about 20% greater  
204 at LHC than at RHIC, depending on the centrality bin. The particle identified  
205  $v_2$  for kaons and pions follows the same trend. However it was observed that for  
206 proton  $v_2$  the quark number scaling does not work [9]. So far there is no agreement  
207 of why this scaling breaks down at LHC or why it works so well at RHIC energies.

208

209 **1.1 Quantum chromodynamics**

210 **1.1.1 Foundation of QCD**

211 There are four known basic interactions in the universe: gravity, electromagnetic,  
212 weak and strong interactions. The standard model of particle physics includes  
213 three of these, excluding the gravitational interaction. The theory of strong inter-  
214 actions is known as Quantum Chromodynamics (QCD).

215 The development of QCD began after the introduction of new powerful particle  
216 accelerators that were capable of particle physics research in the 1950s. Before this  
217 particles were mainly discovered from cosmic rays. Positrons, neutrons and muons  
218 were discovered in the 1930s and charged pions were discovered in 1947 []. The  
219 neutral pion was discovered in 1950 [10].

220 The Lawrence Berkeley National Laboratory started the Bevalac accelerator in  
221 1954, Super Proton Synchrotron (SPS) in CERN began operating in 1959 and the  
222 Alternating Gradient Synchrotron (AGS) at Brookhaven started in 1960. With  
223 an energy of 33 GeV AGS was the most powerful accelerator of that time. By  
224 the beginning of 1960s several new particles had been discovered. These included  
225 antiprotons, antineutrons,  $\Delta$ -particles and the six hyperons ( $\Xi^0$ ,  $\Xi^-$ ,  $\Sigma^\pm$ ,  $\Sigma^0$  and  
226  $\Lambda$ ).

227 Facing this avalanche of new particles, physicists started the search for symme-  
228 tries within them. Already in 1932 Heisenberg [11] had proposed an isospin model  
229 to explain similarities between the proton and the neutron. In 1962 Gell-Mann  
230 and Ne'eman presented that particles sharing the same quantum numbers (spin,  
231 parity) could be organised using the symmetry of SU(3). [12] Heisenberg's Isospin  
232 model followed the symmetry of SU(2). Using the SU(3) model known baryons  
233 and mesons could be presented as octets. This also lead to the discovery of the  
234  $\Omega^-$  particle since this was missing from the SU(3) decouplet that included heavier  
235 baryons.

236 The most simple representation of SU(3) was a triplet. Inside this triplet parti-  
237 cles would have electric charges  $2/3$  or  $-1/3$ . However, these had not been detected.  
238 In 1964 Gell-Mann [13] and Zweig proposed that baryons and mesons would be  
239 bound states of these three hypothetical triplet particles that Gell-Mann called  
240 quarks. Now we know that these are the  $u$ ,  $d$  and  $s$  quarks. This original quark  
241 model without colour was violating the Pauli exclusion principle. For example  
242 the  $\Omega^-$  particle is comprised of three  $s$  quarks which would have exactly the same  
243 quantum states.

244 The first one to present the idea of colour was Greenberg already in 1964 [14].  
245 In 1971 Gell-Mann and Fritsch presented their model, which solved the antisym-  
246 metry problem. They added a colour quantum number to quarks, which separated  
247 quarks of the same species. In the new colour model the baryonic wave function

248 became

$$(qqq) \rightarrow (q_r q_g q_b - q_g q_r q_b + q_b q_r q_g - q_r q_b q_g + q_g q_b q_r - q_b q_g q_r), \quad (1)$$

249 The colour model was also supported by experimental evidence. The decay  
250 rate of a neutral pion with the addition of colours is

$$\Lambda(\pi^0 \rightarrow \gamma\gamma) = \frac{\alpha^2}{2\pi} \frac{N_c^2}{3^2} \frac{m_\pi^3}{f_\pi^2}. \quad (2)$$

251 For  $N_c = 3$  this gives 7.75 eV and the measured value is  $(7.86 \pm 0.54)$  eV [15].

252 Another observable that combines the colour information also to the number  
253 of quark flavours is The Drell-Ratio  $R$  [16]

$$R = \frac{\sigma(e^+ + e^- \rightarrow \text{hadrons})}{\sigma(e^+ + e^- \rightarrow \mu^+ + \mu^-)} = N_c \sum_f Q_f^2. \quad (3)$$

254 This ratio has the numerical value 2 when including the three light quarks  $u$ ,  $d$   
255 and  $s$ . When the collision energy reaches the threshold of heavy quark ( $c$  and  
256  $b$ ) production processes this increases to  $^{10}/3$  (for  $f = u, d, s, c$ ) and  $^{11}/3$  (for  $f =$   
257  $u, d, s, c, b$ ). The threshold of  $t\bar{t}$  production,  $\sqrt{s} \approx 350$  GeV has not been reached  
258 so far by any  $e^+e^-$  colliders.

259 The colour model explained why no free quarks had been observed as only  
260 colour neutral states are possible. The simplest ways of producing a colour neu-  
261 tral object are the combination of three quarks, and the combination of a quark-  
262 antiquark pair. These are known as baryons and mesons.

263 After the addition of colour the main ingredients of QCD had been established.  
264 The final quantum field theory of Quantum Chromodynamics formed quickly be-  
265 tween 1972 and 1974. Main part of this was the work Gross, Wilczek, Politzer  
266 and George did for non-abelian gauge field theories [17–21]. Gross, Wilczek and  
267 Politzer received the Nobel Prize in Physics for their work. The role of gluons as  
268 a colour octet was presented by Fritzsch, Gell-Mann and Leutwyler in 1973 [22].  
269 The theory had now 8 massless gluons to mediate the strong interaction.

270 However, these gluons had not been discovered. Indirect evidence of the ex-  
271 istence had been seen as it was observed that only about half of the momentum  
272 of protons was transported by the quarks [23]. Direct evidence should be seen in  
273 electron-electron collisions as a third, gluonic, jet in addition to two quark jets.  
274 Three jet events were first seen in 1979 at the PETRA accelerator at DESY [24–26].

### 275 1.1.2 Asymptotic Freedom

276 In Quantum Electrodynamics (QED) the electric charge is screened. In the vicinity  
277 of a charge, the vacuum becomes polarized. Virtual charged particle-antiparticle

278 pairs around the charge are arranged so that opposing charges face each other.  
279 Since the pairs also include an equal amount opposite charge compared to the  
280 original charge the average charge seen by an observer at a distance is smaller.  
281 When the distance to the charge increases the effective charge decreases until the  
282 coupling constant of QED reaches the fine-structure constant  $\alpha = \frac{1}{137}$ .

283 Contrary to QED, QCD is a non-abelian theory. In other words the generators  
284 of the symmetry group of QCD, SU(3), do not commute. This has the practical  
285 consequence that gluons interact also with other gluons, whereas in QED the  
286 neutral carrier particles, photons, only interact with charged particles. There is  
287 screening also in QCD because of the colour charges, but in addition to that there  
288 is antiscreening because of the gluon interactions. In QCD the antiscreening effect  
289 dominates over screening. For larger distances to the colour charge the coupling  
290 constant is larger. This explains why no free colour charges can be observed. When  
291 the distance between charges increases the interaction strengthens until it is strong  
292 enough to produce a new quark-antiquark pair.

293 On the other hand, at very small distances the coupling constant approaches  
294 0. This is called asymptotic freedom. For large energies and small distances  
295 the coupling constant is negligible. In 1975 Collins [27] predicted a state where  
296 individual quarks and gluons are no longer confined into bound hadronic states.  
297 Instead they form a bulk QCD matter that Edward Shuryak called Quark-Gluon  
298 plasma in his 1980 review of QCD and the theory of superdense matter [28]. QGP  
299 can be seen as a separate state of matter. A schematic view of a phase diagram  
300 for QCD matter is shown in Fig. 1.

301 In the early universe at the age of  $10^{-6}$ s after the Big Bang the conditions  
302 preferred the existence of QGP instead of hadronic matter. Nowadays bulk QCD  
303 matter, its properties and its phase transitions between hadronic matter and the  
304 quark-gluon plasma (QGP) can be explored in the laboratory, through collisions  
305 of heavy atomic nuclei at ultra-relativistic energies. The study of QCD matter at  
306 high temperature is of fundamental and broad interest. The phase transition in  
307 QCD is the only phase transition in a quantum field theory that can be probed by  
308 any present or foreseeable technology.

309 One important property of the QGP is the shear viscosity to entropy ratio,  
310  $\eta/s$ . It is believed that this ratio has an universal minimum value of  $1/4\pi \approx 0.8$ ,  
311 which holds for all substances. This limit would be reached in the strong coupling  
312 limit of certain gauge theories [30]. The temperature dependance of the ratio is  
313 shown in Fig. 2. The minimum value of  $\eta/s$  is found in the vicinity of the critical  
314 temperature,  $T_c$  [31]. Finding the  $\eta/s$  values in QGP matter would therefore also  
315 provide a way of determining the critical point of QCD matter.

316 The  $\eta/s$  value for the matter created in Au-Au collisions at RHIC ( $\sqrt{s_{NN}}$ ) has  
317 been estimated to be  $0.09 \pm 0.015$  [31], which is very close to the lowest value for a

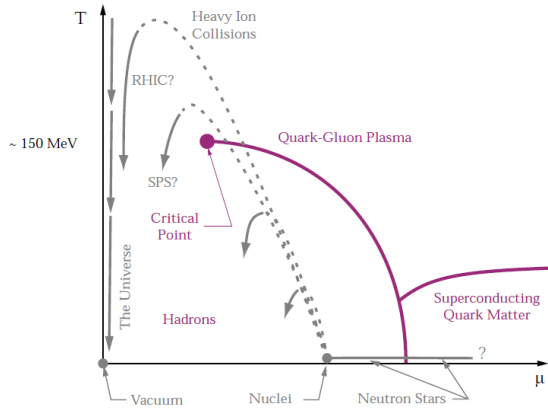


Figure 1: A schematic outline for the phase diagram of QCD matter at ultra-high density and temperature. The quark chemical potential  $\mu$  that is on the x-axis represents the imbalance between quarks and antiquarks. At zero temperature this corresponds to the number of quarks but at higher temperatures there are also additional pairs of quarks and antiquarks. Along the horizontal axis the temperature is zero, and the density is zero up to the onset transition where it jumps to nuclear density, and then rises with increasing  $\mu$ . Neutron stars are in this region of the phase diagram, although it is not known whether their cores are dense enough to reach the quark matter phase. Along the vertical axis the temperature rises, taking us through the crossover from a hadronic gas to the quark-gluon plasma. This is the regime explored by high-energy heavy-ion colliders. [29]

318 wide class of thermal quantum field theories [30] for all relativistic quantum field  
 319 theories at finite temperature and zero chemical potential. This suggests that the  
 320 the matter created goes through a phase where it is close to the critical point of  
 321 QCD.

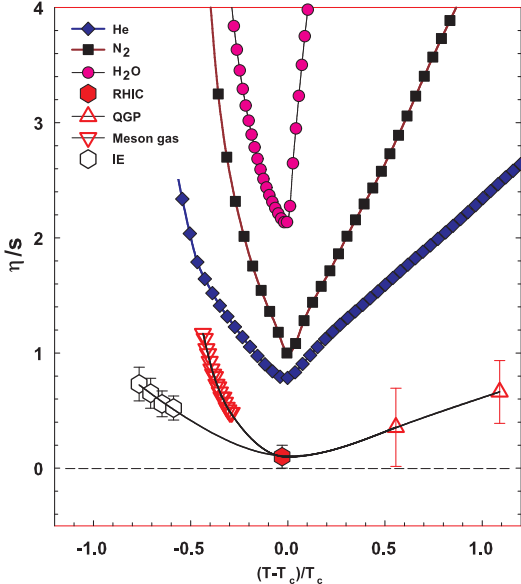


Figure 2:  $\eta/s$  as a function of  $(T - T_c)/T_c$  for several substances as indicated. The calculated values for the meson-gas have an associated error of  $\sim 50\%$ . The lattice QCD value  $T_c = 170$  MeV is assumed for nuclear matter. The lines are drawn to guide the eye. [31]

## **322 1.2 Heavy ion physics**

**323** The Quark Gluon Plasma (QGP) is experimentally accessible by colliding heavy  
**324** ions at high energies. Nowadays research of Heavy-Collisions is mainly performed  
**325** at two particle colliders; the The Relativistic Heavy Ion Collider (RHIC) at BNL  
**326** in New York, USA and he Large Hadron Collider (LHC) at CERN in Switzer-  
**327** land. Energy densities at these colliders should be enough to produce QGP and  
**328** convincing evidence of the creation has been seen at both colliders.

**329** The development of heavy ion physics is strongly connected to the development  
**330** of particle colliders. Experimental study of relativistic heavy ion collisions has been  
**331** carried out for three decades, beginning with the Bevalac at Lawrence Berkeley  
**332** National Laboratory (LBNL) [32], and continuing with the AGS at Brookhaven  
**333** National Laboratory (BNL) [33], CERN SPS [34], RHIC at BNL and LHC at  
**334** CERN. The first colliders could not produce enough energy to create QGP matter  
**335** so they could only probe the hadronic state.

**336** The collective motion of matter in a heavy-ion collision has been modeled using  
**337** several models e.g. the Blast wave Model [35] has been used successfully. Another  
**338** model growing in popularity is the hydrodynamical approach which is further  
**339** discussed in section 1.3.3.

### **340 1.2.1 History**

**341** The first heavy-ion collisions were done at the Bevalac experiment at the Lawrence  
**342** Berkeley National Laboratory [32] and at the Joint Institute for Nuclear Research  
**343** in Dubna [36] at energies up to 1GeV per nucleon. In 1986 the Super Pro-  
**344** ton Synchrotron (SPS) at CERN started to look for QGP signatures in O+Pb  
**345** collisions. The center-of-mass energy per colliding nucleon pair ( $\sqrt{s_{NN}}$ ) was  
**346** 19.4 GeV [34]. These experiments did not find any decisive evidence of the existence  
**347** of QGP. In 1994 a heavier lead (Pb) beam was introduced for new experiments at  
**348**  $\sqrt{s_{NN}} \approx 17$  GeV. At the same time the Alternating Gradient Synchrotron (AGS)  
**349** at BNL, Brookhaven collided ions up to  $^{32}\text{S}$  with a fixed target at energies up  
**350** to 28 GeV [33]. Although the discovery of a new state of matter was reported at  
**351** CERN, these experiments provided no conclusive evidence of QGP. Now SPS is  
**352** used with 400 GeV proton beams for fixed-target experiments, such as the SPS  
**353** Heavy Ion and Neutrino Experiment (SHINE) [37], which tries to search for the  
**354** critical point of strongly interacting matter.

**355** The Relativistic Heavy Ion Collider (RHIC) at BNL in New York, USA started  
**356** its operation in 2000. The top center-of-mass energy per nucleon pair at RHIC, 200  
**357** GeV, was reached in the following years. The results from the experiments at RHIC  
**358** have provided a lot of convincing evidences that QGP was created [3,4,38,39]. The  
**359** newest addition to the group of accelerators capable of heavy-ion physics is the

<sup>360</sup> Large Hadron Collider (LHC) at CERN, Switzerland. LHC started operating in  
<sup>361</sup> November 2009 with proton-proton collisions. First Pb-Pb heavy ion runs started  
<sup>362</sup> in November 2010 with  $\sqrt{s_{NN}} = 2.76$  TeV, over ten times higher than at RHIC.  
<sup>363</sup> Among the six experiments at LHC, the Large Ion Collider Experiment (ALICE)  
<sup>364</sup> is dedicated to heavy ion physics. Also CMS and ATLAS have active heavy ion  
<sup>365</sup> programs.

366 **1.3 Features of Heavy-Ion Collisions**

367 **1.3.1 Collision Geometry**

368 In contrast to protons atomic nuclei are objects with considerable transverse size.  
369 The properties of a heavy-ion collision depend strongly on the impact parameter  
370  $b$  which is the vector connecting the centers of the two colliding nuclei at their  
371 closest approach. One illustration of a heavy-ion collision is shown in Fig. 3.

372 Impact parameter defines the reaction plane which is the plane spanned by  $b$   
373 and the beam direction.  $\Psi_{RP}$  gives the angle between the reaction plane and some  
374 reference frame angle. Experimentally the reference frame is fixed by the detector  
375 setup. Reaction plane angle cannot be directly measured in high energy nuclear  
 collisions, but it can be estimated with the event plane method [40].

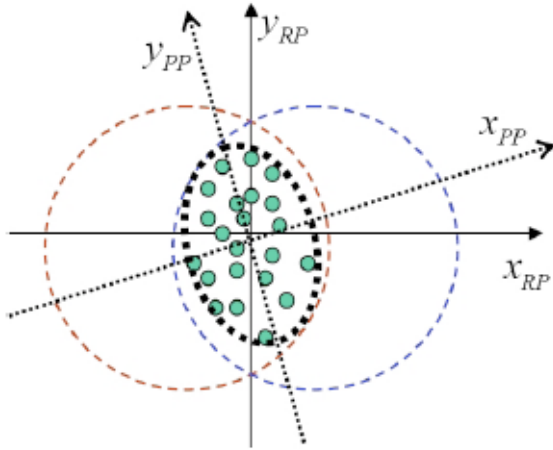


Figure 3: The definitions of the Reaction Plane and Participant Plane coordinate systems [41]. The dashed circles represent the two colliding nuclei and the green dots are partons that take part in the collision.  $x_{PP}$  and  $x_{RP}$  are the participant and reaction planes. The angle between  $x_{RP}$  and  $x_{PP}$  is given by Eq. (4).  $y_{PP}$  and  $y_{RP}$  are lines perpendicular to the participant and reaction planes.

376  
377 Participant zone is the area containing the participants. The distribution of  
378 nucleons in the nucleus exhibits time-dependent fluctuations. Because the nucleon  
379 distribution at the time of the collision defines the participant zone, the axis of  
380 the participant zone fluctuates and can deviate from the reaction plane. The angle  
381 between the participant plane and the reaction plane is defined by [42]

$$\psi_{PP} = \arctan \frac{-2\sigma_{xy}}{\sigma_y^2 - \sigma_x^2 + \sqrt{(\sigma_y^2 - \sigma_x^2)^2 + 4\sigma_{xy}^2}}, \quad (4)$$

382 where the  $\sigma$ -terms are averaged over the energy density.

$$\sigma_y^2 = \langle y^2 \rangle - \langle y \rangle^2, \sigma_x^2 = \langle x^2 \rangle - \langle x \rangle^2, \sigma_{xy} = \langle xy \rangle - \langle x \rangle \langle y \rangle \quad (5)$$

383 The impact parameter is one way to quantize the centrality of a heavy-ion  
 384 collision but it is impossible to measure in a collision. It can be estimated from  
 385 observed data using theoretical models, but this is always model-dependent and  
 386 to compare results from different experiments one needs an universal definition for  
 387 centrality. The difference between central and peripheral collisions is illustrated  
 388 in Fig. 4. In a central collision the overlap region is larger than in a peripheral  
 389 collision. Larger overlap region translates into a larger number of nucleons partici-  
 390 pating in the collision, which in turn leads to a larger number of particles produced  
 391 in the event.

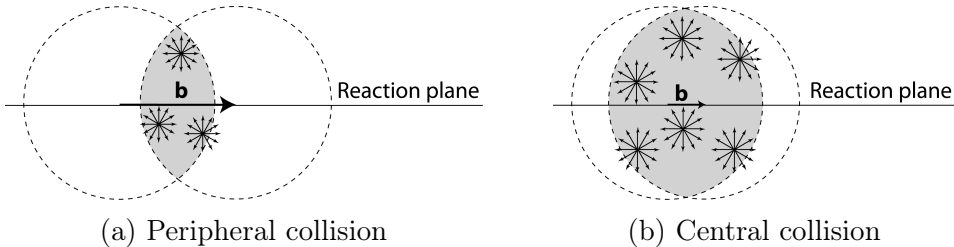


Figure 4: Interaction between partons in central and peripheral collisions. The snowflakes represent elementary parton-parton collisions. When the impact parameter  $b$  is large the number of elementary collisions is small. Particle production is small. Smaller impact parameter increases the number of elementary collisions. This increases particle production.

392 Usually centrality is defined by dividing collision events into percentile bins by  
 393 the number participants or experimentally by the observed multiplicity. Centrality  
 394 bin 0-5% corresponds to the most central collisions with the highest multiplicity  
 395 and higher centrality percentages correspond to more peripheral collisions with  
 396 lower multiplicities. A multiplicity distribution from ALICE measurements [43]  
 397 illustrating the centrality division is shown in Fig. 5. The distribution is fitted  
 398 using a phenomenological approach based on a Glauber Monte Carlo [44] plus a  
 399 convolution of a model for the particle production and a negative binomial distri-  
 400 bution.

#### 401 1.3.2 Nuclear Geometry

402 To model heavy-ion collisions one must first have a description as good as possible  
 403 of the colliding objects. Atomic nuclei are complex ensembles of nucleons. The  
 404 nuclei used in heavy-ion physics have in the order of 200 nucleons. Mostly used

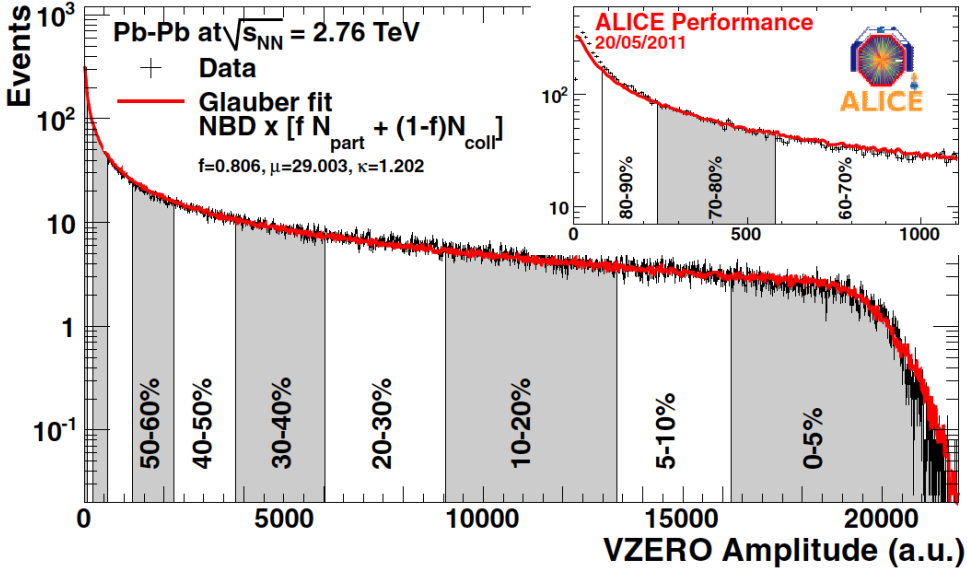


Figure 5: An illustration of the multiplicity distribution in ALICE measurements. The red line shows the fit of the Glauber calculation to the measurement. The data is divided into centrality bins [43]. The size of the bins corresponds to the indicated percentile.

405 nuclei are  $^{208}\text{Pb}$  at LHC and  $^{197}\text{Au}$  at RHIC. The distribution of these nucleons  
 406 within a nucleus is not uniform and is subject to fluctuations in time.

407 Nuclear geometry in heavy-ion collisions is often modelled with the Glauber  
 408 Model. The model was originally developed to address the problem of high energy  
 409 scattering with composite particles. Glauber presented his first collection of papers  
 410 and unpublished work in his 1958 lectures [45]. In the 1970's Glauber's work  
 411 started to have utility in describing total cross sections. Maximon and Czyz applied  
 412 it to proton-nucleus and nucleus-nucleus collisions in 1969 [46].

413 In 1976 [47] Białas, Bleszyński, and Czyz applied Glauber's approach to  
 414 inelastic nuclear collisions. Their approach introduced the basic functions used in  
 415 modern language including the thickness function and the nuclear overlap function.  
 416 Thickness function is the integral of the nuclear density over a line going through  
 417 the nucleus with minimum distance  $s$  from its center

$$T_A(s) = \int_{-\infty}^{\infty} dz \rho \left( \sqrt{s^2 + z^2} \right). \quad (6)$$

418 This function gives the thickness of the nucleus, i.e. the amount material seen by  
 419 a particle passing through it.

<sup>420</sup> Overlap function is an integral of the thickness functions of two colliding nuclei  
<sup>421</sup> over the overlap area. This can be seen as the material that takes part in the  
<sup>422</sup> collision. It is given as a function of the impact parameter  $b$

$$T_{AB}(b) = \int ds^2 T_A(\bar{s}) T_B(\bar{s} - \bar{b}) \quad (7)$$

<sup>423</sup> The average overlap function,  $\langle T_{AA} \rangle$ , in an A-A collisions is given by [48]

$$\langle T_{AA} \rangle = \frac{\int T_{AA}(b) db}{\int (1 - e^{-\sigma_{pp}^{inel} T_{AA}(b)}) db}. \quad (8)$$

<sup>424</sup> Using  $\langle T_{AA} \rangle$  one can calculate the mean number of binary collisions

$$\langle N_{coll} \rangle = \sigma_{pp}^{inel} \langle T_{AA} \rangle, \quad (9)$$

<sup>425</sup> where the total inelastic cross-section,  $\sigma_{pp}^{inel}$ , gives the probability of two nucleons  
<sup>426</sup> interacting. The number of binary collisions is related to the hard processes in a  
<sup>427</sup> heavy-ion collision. Each binary collision has equal probability for direct produc-  
<sup>428</sup> tion of high-momentum partons. Thus the number of high momentum particles is  
<sup>429</sup> proportional to  $\langle N_{coll} \rangle$ .

<sup>430</sup> Soft production on the other hand is related to the number of participants.  
<sup>431</sup> It is assumed that in the binary interactions participants get excited and further  
<sup>432</sup> interactions are not affected by previous interactions because the time scales are  
<sup>433</sup> too short for any reaction to happen in the nucleons. After the interactions ex-  
<sup>434</sup> cited nucleons are transformed into soft particle production. Production does not  
<sup>435</sup> depend on the number of interactions a nucleon has gone through. The average  
<sup>436</sup> number of participants,  $\langle N_{part} \rangle$  can also be calculated from the Glauber model

$$\begin{aligned} \langle N_{part}^{AB}(b) \rangle &= \int ds^2 T_A(\bar{s}) \left[ 1 - \left[ 1 - \sigma_{NN} \frac{T_B(\bar{s} - \bar{b})}{B} \right]^B \right] \\ &+ \int ds^2 T_B(\bar{s}) \left[ 1 - \left[ 1 - \sigma_{NN} \frac{T_A(\bar{s} - \bar{b})}{A} \right]^A \right]. \end{aligned} \quad (10)$$

<sup>437</sup> Glauber calculations require some knowledge of the properties of the nuclei.  
<sup>438</sup> One requirement is the nucleon density distribution, which can be experimen-  
<sup>439</sup> tally determined by studying the nuclear charge distribution in low-energy elec-  
<sup>440</sup> tron scattering experiments [44]. The nucleon density is usually parametrized by  
<sup>441</sup> a Woods-Saxon distribution

$$\rho(r) = \frac{\rho_0}{1 + \exp\left(\frac{r-R}{a}\right)}, \quad (11)$$

where  $\rho_0$  is the nucleon density in center of the nucleus,  $R$  is the nuclear radius and  $a$  parametrizes the depth of the skin. The density stays relatively constant as a function of  $r$  until around  $R$  where it drops to almost 0 within a distance given by  $a$ .

Another observable required in the calculations is the total inelastic nucleon-nucleon cross-section  $\sigma_{\text{inel}}^{\text{NN}}$ . This can be measured in proton-proton collisions at different energies.

There are two often used approaches to Glauber calculations. The optical approximation is one way to get simple analytical expressions for the nucleus-nucleus interaction cross-section, the number of interacting nucleons and the number of nucleon-nucleon collisions. In the optical Glauber it is assumed that during the crossing of the nuclei the nucleons move independently and they will be essentially undeflected.

With the increase of computational power at hand the Glauber Monte Carlo (GMC) approach has emerged as a method to get a more realistic description of the collisions. In GMC the nucleons are distributed randomly in three-dimensional coordinate system according to the nuclear density distributions. Also nuclear parameters, like the radius  $R$  can be sampled from a distribution. A heavy-ion collision is then treated as a series of independent nucleon-nucleon collisions, where in the simplest model nucleons interact if their distance in the plane orthogonal to the beam axis,  $d$ , satisfies

$$d < \sqrt{\sigma_{\text{inel}}^{\text{NN}}} \quad (12)$$

The average number of participants and binary collisions can then be determined by simulating many nucleus-nucleus collisions. The results of one GMC Pb-Pb event with impact parameter  $b = 9.8$  fm is shown in Fig. 6

### 1.3.3 Hydrodynamical Modelling

The relativistic version of hydrodynamics has been used to model the deconfined phase of a heavy-ion collision with success. Heavy-ion collisions produce many hadrons going into all directions. It is expected that tools from statistical physics would be applicable to this complexity [49]. The power of relativistic hydrodynamics lies in its simplicity and generality. Hydrodynamics only requires that there is local thermal equilibrium in the system. In order to reach thermal equilibrium the system must be strongly coupled so that the mean free path is shorter than the length scales of interest [50].

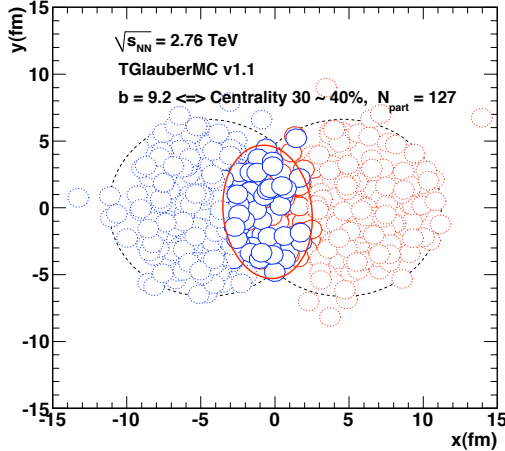


Figure 6: The results of one Glauber Monte Carlo simulation. Big circles with black dotted boundaries represent the two colliding nuclei. The participant zone is highlighted with the solid red line. Small red and blue circles represent nucleons. Circles with thick boundaries are participants i.e. they interact with at least one nucleon from the other nucleus. Small circles with dotted boundaries are spectators which do not take part in the collision.

475 The use of relativistic hydrodynamics in high-energy physics dates back to  
 476 Landau [51] and the 1950's, before QCD was discovered. Back then it was used  
 477 in proton-proton collisions. Development of hydrodynamics for the use of heavy-  
 478 ion physics has been active since the 1980's, including Bjorken's study of boost-  
 479 invariant longitudinal expansion and infinite transverse flow [?]. Major steps were  
 480 taken later with the inclusion of finite size and and dynamically generated trans-  
 481 verse size [?, ?], a part of which was done at the University of Jyväskylä. The role  
 482 of hydrodynamics in heavy-ion physics was strengthened when QGP was observed  
 483 to behave like a liquid by RHIC [3].

484 The evolution of a heavy-ion event can be divided into four stages. A schematic  
 485 representation of the evolution of the collisions is shown in Fig. 7. Stage 1 follows  
 486 immediately the collision. This is known as the pre-equilibrium stage. Hydrody-  
 487 namic description is not applicable to this regime because thermal equilibrium is  
 488 not yet reached. The length of this stage is not known but it is assumed to last  
 489 about  $1 \text{ fm}/c$  in proper time  $\tau$ .

490 The second stage is the regime where thermal equilibrium or at least near-  
 491 equilibrium is reached. In this stage hydrodynamics should be applicable if the  
 492 temperature is above the deconfinement temperature [50]. This lasts about  $5 -$   
 493  $10 \text{ fm}/c$  until the temperature of the system sinks low enough for hadronization to

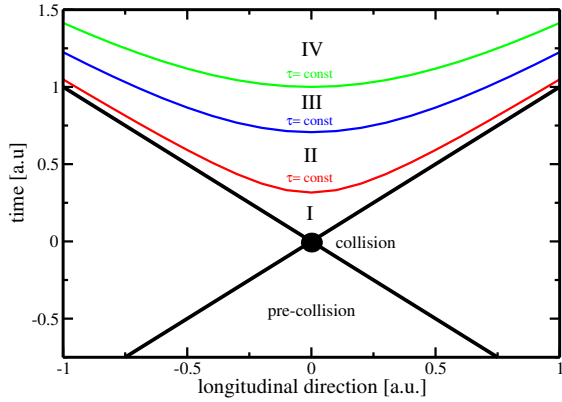


Figure 7: Schematic representation [50] of a heavy-ion collision as the function of time and longitudinal coordinates  $z$ . The various stages of the evolution correspond to proper time  $\tau = \sqrt{t^2 - z^2}$  which is shown as hyperbolic curves separating the different stages.

494 occur. Now the system loses its deconfined, strongly coupled, state and hydrodynamics  
 495 can no longer be used. The third stage is the hadron gas stage where the  
 496 hadrons still interact. This ends when hadron scattering becomes rare and they  
 497 no longer interact. In the final stage hadrons are free streaming and they fly in  
 498 straight lines until they reach the detector.

499 The hydrodynamical approach treats the ensemble of particles as a fluid. It  
 500 uses basic equations from hydrodynamics and thermodynamics but with a few  
 501 modifications to account for the relativistic energies. The calculation is based  
 502 on a collection of differential equations connecting the local thermal variables like  
 503 temperature, pressure etc. to local velocities of the fluid. One also needs equations  
 504 of state that connect the properties of the matter, e.g. temperature and pressure  
 505 to density. Given initial conditions and equations of state the calculation gives the  
 506 time-evolution of the system.

507 At first only ideal hydrodynamics was used. Ideal hydrodynamics does not  
 508 include viscosity but it is a relatively good approximation and it could predict  
 509 phenomena like elliptic flow. For more detailed calculations also viscosity must be  
 510 considered and viscosity itself is an interesting property of QGP.

## 511 1.4 Flow

512 In a heavy-ion collision the bulk particle production is known as flow. The pro-  
 513 duction is mainly isotropic but a lot of studies including my thesis focus on the  
 514 small anisotropies. After the formation of the QGP, the matter begins to expand  
 515 as it is driven outwards by the strong pressure difference between the center of the  
 516 collision zone and the vacuum outside the collision volume. The pressure-driven  
 517 expansion is transformed into flow of low-momentum particles in the hadroniza-  
 518 tion phase. Since the expansion is mainly isotropic the resulting particle flow is  
 519 isotropic with small anisotropic corrections that are of the order of 10% at most.  
 520 The isotropic part of flow is referred to as radial flow.

521 The transverse momentum spectra  $dN/dp_T$  in heavy-ion collisions is shown

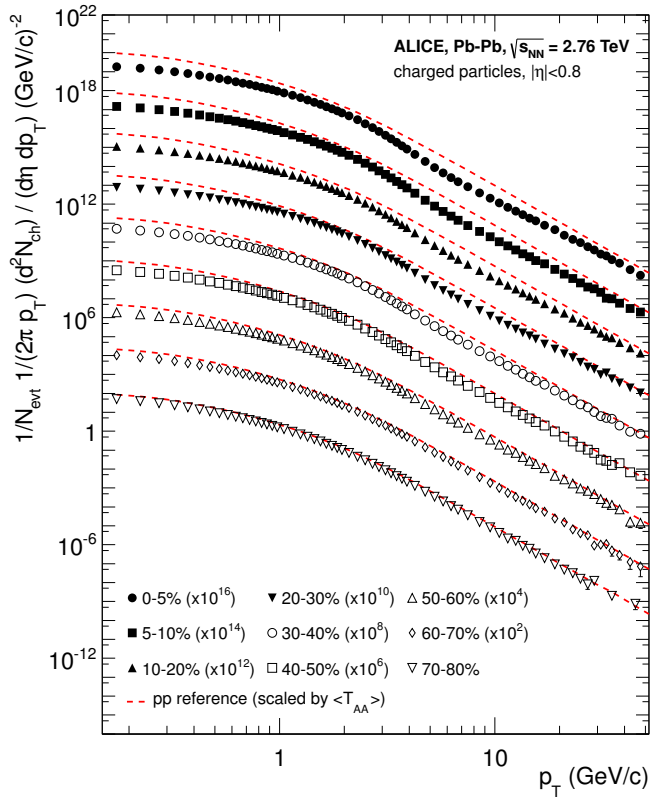


Figure 8: Charged particle spectra measured by ALICE [54] for the 9 centrality classes given in the legend. The distributions are offset by arbitrary factors given in the legend for clarity. The distributions are offset by arbitrary factors given in the legend for clarity. The dashed lines show the proton-proton reference spectra scaled by the nuclear overlap function determined for each centrality class and by the Pb-Pb spectra scaling factors [54].

522 in Fig. 8. The vast majority of produced particles have small  $p_T$ . The difference  
 523 between the yield of 1 GeV/c and 4 GeV/c particles is already 2-3 orders of mag-  
 524 nitude. Any observables that are integrated over  $p_T$  are therefore dominated by  
 525 the small momentum particles.

#### 526 1.4.1 Anisotropic Flow

527 In a non-central heavy-ion collision the shape of the impact zone is almond-like.  
 528 In peripheral collisions the impact parameter is large which means a strongly  
 529 asymmetric overlap region. In a central collision the overlap region is almost  
 530 symmetric in the transverse plane. In this case the impact parameter is small.  
 531 Collisions with different impact parameters are shown in Fig. 4.

532 The pressure gradient is largest in-plane, in the direction of the impact pa-  
 533 rameter  $b$ , where the distance from high pressure, at the collision center, to low  
 534 pressure, outside the overlap zone, is smallest. This leads to stronger collective  
 535 flow into in-plane direction, which in turn results in enhanced thermal emission  
 536 through a larger effective temperature into this direction, as compared to out-of-  
 537 plane [5, 6, 55]. The resulting flow is illustrated in Fig. 9. Flow with two maxima  
 538 in the direction of the reaction plane is called elliptic flow. This is the dominant

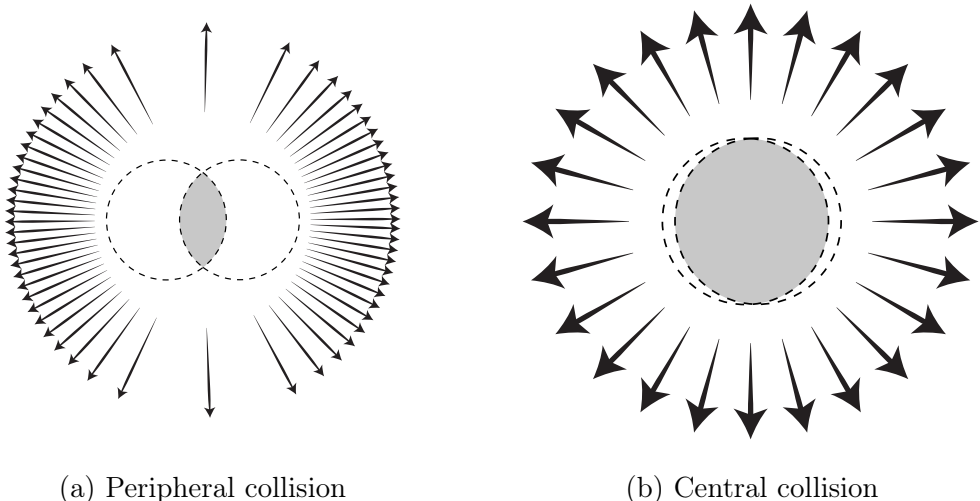


Figure 9: Illustration of flow in momentum space in central and peripheral collisions. The density of the arrows represent the magnitude of flow seen at a large distance from the collision in the corresponding azimuthal direction. In a peripheral collision momentum flow into in-plane direction is strong and flow into out-of-plane direction is weak. In a central collision anisotropy in flow is smaller, but the total yield of particles is larger.

part of anisotropic flow. Also more complex flow patterns can be identified. The most notable of these is the triangular flow, which is mainly due to fluctuations in the initial conditions.

Flow is nowadays usually quantified in the form of a Fourier composition

$$E \frac{d^3N}{dp^3} = \frac{1}{2\pi p_T} \frac{d^2N}{dp_T d\eta} \left( 1 + \sum_{n=1}^{\infty} 2v_n(p_T, \eta) \cos(n(\phi - \Psi_n)) \right), \quad (13)$$

where the coefficients  $v_n$  give the relative strengths of different anisotropic flow components and the overall normalisation gives the strength of radial flow. Elliptic flow is represented by  $v_2$  and  $v_3$  represents triangular flow. The first coefficient,  $v_1$ , is connected to directed flow. This will however in total be zero because of momentum conservation. It can be nonzero in some rapidity or momentum regions but it must be canceled by other regions.

The first approaches to quantifying the anisotropy of flow did not use the Fourier composition. Instead they approached the problem with a classic event shape analysis using directivity [56] or sphericity [5, 57] to quantify the flow.

The first experimental studies of anisotropy were performed at the AGS [58] in 1993. They noted that the anisotropy of particle production in one region correlates with the reaction plane angle defined in another region.

The first ones to present the Fourier decomposition were Voloshin and Zhang in 1996 [59]. This new approach was useful for detecting different types of anisotropy in flow, since the different Fourier coefficients give different harmonics in flow. They also show the relative magnitude of each harmonic compared to radial flow.

Some parts of the Fourier composition approach were used for Au-Au collisions at  $\sqrt{s_{NN}} = 11.4\text{GeV}$  at AGS in 1994 [60]. This analysis still focused on event shapes but they constructed these shapes using Fourier composition from different rapidity windows.

#### 1.4.2 High $p_T$ Phenomena

The measurement of anisotropic flow coefficients can be extended to very high transverse momenta  $p_T$ . High  $p_T$  measurements of  $v_2$  from CMS [61] are shown in Fig. 17. For high transverse momenta  $v_2$  values are positive and they decrease slowly as a function of  $p_T$ . At high transverse momentum the  $v_2$  values don't, however, represent flow.

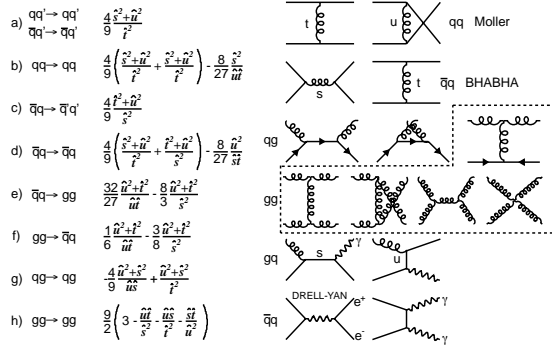


Figure 10: The basic pQCD processes and their quadratic matrix elements

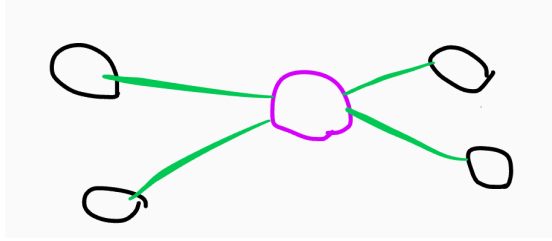


Figure 11: Schematic view of hard scattering process of  $p + p \rightarrow 2 \text{jets}$

## 569 1.5 Hard processes

### 570 1.5.1 pQCD factorization

571 The term Hard Scattering is used in connection with the scattering of two point-like constituents (partons) of colliding nucleons, when the momentum transfer  $Q^2$   
 572 is large ( $Q \gg \Lambda_{\text{QCD}}$ ). Figure ?? shows the incoming partons, quarks or gluons, as  
 573 they exchange a space-like virtual gluon and produce two highly virtual outgoing  
 574 partons. The outgoing partons will eventually fragment into collimated showers of  
 575 partons, referred to as jets

577 Jet fragmentation can be factorised into three components; the parton distribution functions  $f_a, f_b$  that give the probability of getting a parton with momentum fraction  $x$  of the proton, the cross section of the elementary scattering  $ab \rightarrow cd$  (Fig. 10) and the fragmentation functions that give the probability of getting hadron  $h$  from the parton.

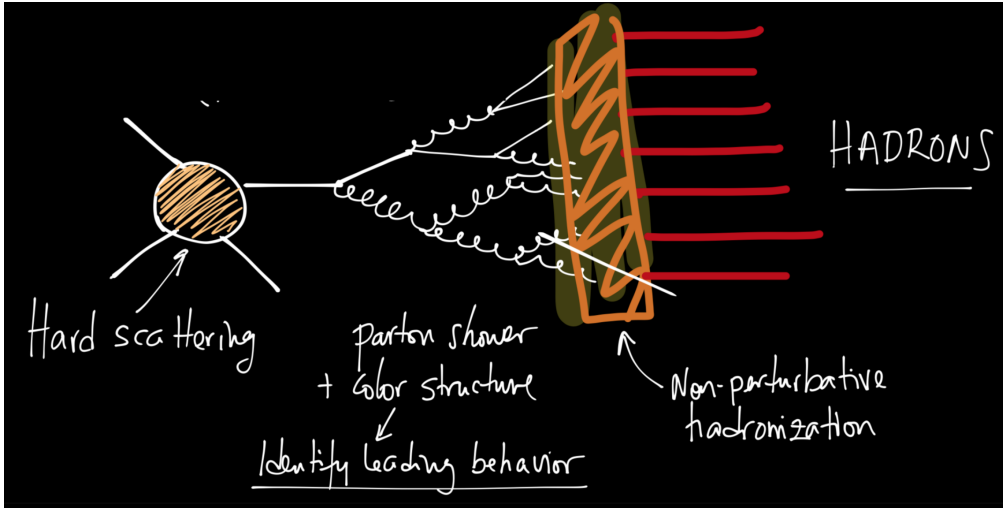


Figure 12: REPLACE FIGURE An illustration of jet showering. The highly virtual parton from the hard scattering will produce a shower of softer partons. When the virtuality is low enough the shower will go through a hadronisation process that produces the hadrons, which will be eventually observed in the detector.

$$\frac{d\sigma_{pp}^h}{dy d^2 p_T} = K \sum_{abcd} \int dx_a dx_b f_a(x_a, Q^2) f_b(x_b, Q^2) \frac{d\sigma}{dt} (ab \rightarrow cd) \frac{D_{h/c}^0}{\pi z_c}$$

$$x_a = \frac{|p_a|}{|p_{proton}|}$$

## 582 Parton Distribution Function

583 Parton Distribution Functions (PDFs) are essential to calculate the scattering cross  
584 section. They are extracted from comprehensive global analysis of experimental  
585 results from a variety of fixed-target and collider experiments. PDFs  $f_a(x)$  give the  
586 differential probability for parton  $a$  to carry momentum fraction  $x$  of the proton  
587 momentum.

588 PDFs cannot be calculated from first principles. In practice the PDFs are  
589 measured in Deeply Inelastic Scattering (DIS) experiments and are extrapolated  
590 to the relevant momentum scales at LHC using the Dokshitzer-Gribov-Lipatov-  
591 Altarelli-Parisi (DGLAP) evolution scheme [?] 14.

$$\mu_F^2 \frac{\partial f_i(x, \mu_F^2)}{\partial \mu_F^2} = \sum_j \frac{\alpha_s(\mu_F)}{2\pi i} \int_x^1 \frac{dz}{z} P_{ij}(z) f_j\left(\frac{x}{z}, \mu_F^2\right), \quad (14)$$

592 where  $\mu_F$  is a factorization scale. The splitting functions  $P_{ij}$  describe a probability to radiate parton  $i$  from parton  $j$  as a function of the momentum fraction  $z$  carried away by the offspring parton.

593 The final component in the factorization, fragmentation functions, describe  
594 the distribution of the fractional momenta of particles radiated from the outgoing  
595 parton. Fragmentation function are given with respect to the momentum fraction  
596  $z$  which is defined as the longitudinal momentum fraction of jet momentum  $p_{\text{jet}}$   
597 carried away by the jet fragment  $p_{\text{part}}$

$$z = \frac{\bar{p}_{\text{part}} \cdot \bar{p}_{\text{jet}}}{p_{\text{jet}}^2} = \frac{p_{\text{part}}}{p_{\text{jet}}} \Big|_{\bar{p}_{\text{part}} \times \bar{p}_{\text{jet}} = 0} \quad (15)$$

600 Fragmentation function  $D(z)$  then gives the average multiplicity  $m$  of jet fragments having  $z > z_0$  [].

$$m(z_0) = \int_{z_0}^1 D(z) dz \Rightarrow m(0) \equiv \langle m \rangle = \int_0^1 D(z) dz \quad (16)$$

602 Because of momentum conservation the sum of all jet fragments must be equal  
603 to the jet momentum, i.e.

$$\sum p_{i,\text{part}} = p_{\text{jet}} \Rightarrow \sum z_i = 1 \Rightarrow \int_0^1 z D(z) dz = 1 \quad (17)$$

604 A natural consequence is that the average momentum fraction is the inverse of  
605 the average multiplicity

$$\langle z \rangle = \frac{\int_0^1 z D(z)}{\int_0^1 D(z)} = \frac{1}{\langle m \rangle} \quad (18)$$

### 606 1.5.2 Jet hadronisation

607 When the parton shower reaches a scale close to  $\Lambda_{\text{QCD}}$ , the perturbative description  
608 is no longer valid. Thus the hadronisation stage must be described in a  
609 non-perturbative manner. One simple scenario that is used in several theory calculations  
610 is the so-called local parton-hadron duality [62]. In the local parton-hadron  
611 duality hypothesis it is assumed that there exists a low virtuality scale  $Q_0$  in which  
612 the hadronisation happens, that is independent of the scale of the primary hard  
613 process. At this scale the partons are transformed into hadrons, assuming that the  
614 flow of momentum and quantum numbers for the hadrons can be directly obtained  
615 from those of partons introducing only small normalising constants.

616 Hadronisation is assumed to be universal, i.e. it shouldn't depend on the  
617 collision energy or system.

618 **Lund string model**

619 One common implementation in MC generators is the Lund string fragmentation  
 620 algorithm [63]. The string model is based on the fact that in QCD linear confine-  
 621 ment is expected over large distances [64]. This can be modelled by imagining a  
 622 colour flux tube being stretched between the outgoing partons. The left side of  
 623 Fig. 14 illustrates this point for a  $q\bar{q}$ -pair. The tube is assumed to have a uniform  
 624 fixed transverse size of about 1 fm along its length, which leads to a linearly rising  
 625 potential  $V(r) = \kappa r$ , where the string constant  $\kappa$  describes the amount of energy  
 626 per unit length. A value of  $\kappa \approx 1\text{GeV}/\text{fm} \approx 0.2\text{GeV}^2$  can be obtained from hadron  
 627 mass spectroscopy.

628 The evolution of string fragmentation is illustrated schematically on the right  
 629 side of Fig. 14. This figure is drawn in a light cone presentation, so the initial  
 630 quark and antiquark are going to separate directions at the speed of light, which  
 631 assumes them as massless. The string between them, illustrated in the figure by  
 632 the red line, stretches until its potential energy becomes high enough that it can  
 633 break, forming a new quark-antiquark pair. If the original pair was  $q\bar{q}$  and the  
 634 new pair  $q'\bar{q}'$ , now two new pairs  $q\bar{q}'$  and  $q'\bar{q}$  have formed. As these particles  
 635 are also moving away from each other, the strings between them can stretch and  
 636 break, creating yet more pairs. The process continues until the invariant mass of  
 637 the system connected by the string becomes small enough and a final state meson  
 638 is formed.

639 To mathematically model the string one can use a massless relativistic string  
 640 with no transverse degrees of freedom. The gluons are represented as energy and  
 641 momentum carrying kinks on the string with incoherent sums of one colour charge  
 642 and one anticolour charge. When this string breaks, it is classically required that  
 643 the created quark and antiquark are produced at a certain distance if they are to  
 644 have any mass or transverse momentum. However, taking into account quantum  
 645 mechanics, the pair must be created at one point and then tunnel out to the  
 646 classically allowed region. Thus the probability to create a new quark-antiquark  
 647 pair becomes proportional to the tunnelling probability [63].

$$P_{\text{tunnelling}} \propto \exp\left(\frac{-\pi m_\perp^2}{\kappa}\right) = \exp\left(\frac{-\pi m^2}{\kappa}\right) \left(\frac{-\pi p_\perp^2}{\kappa}\right), \quad (19)$$

648 where the transverse mass  $m_\perp$  is defined as  $m_\perp^2 = m^2 + p_\perp^2$ . The transverse  
 649 momentum is now defined to be transverse to the string axis. This formula gives  
 650 flavour-independent Gaussian  $p_\perp$ -distribution for the created  $q\bar{q}$  pairs.

651 As explained above the string fragmentation would only produce mesons in  
 652 the final state, but we know that also baryons are created in the process. In the  
 653 string fragmentation model baryon production is included by adding a probability  
 654 that a diquark-antidiquark pair is created instead of a quark-antiquark pair when

655 a string breaks.

656 The kinematics of each string breaking are determined iteratively. Since there  
657 is no natural ordering, the string breaking can be considered in any order and  
658 the answer obtained must be the same. One can start from the q leg and work  
659 one's way to the  $\bar{q}$  leg, or vice versa. This give a left-right symmetry of the  
660 string fragmentation. In the Lund model this is taken into account by defining a  
661 symmetric fragmentation function

$$f(z) \propto \frac{1}{z} (1-z)^a \exp\left(-\frac{bm_{\perp}^2}{z}\right) \quad (20)$$

662 to break the string into a hadron and a remainder system. In the function  $z$  is  
663 the fraction of light-cone momentum  $p^+$  given to the hadron in the string breaking,  
664  $m_{\perp}$  is the transverse mass of the hadron and  $a$  and  $b$  are tuneable parameters of  
665 the model. For heavy quarks this has to be modified as

$$f(z) \propto \frac{1}{z^{1+bm_Q^2}} (1-z)^a \exp\left(-\frac{bm_{\perp}^2}{z}\right) \quad (21)$$

666 The process can be thought as follows: first start from the q-leg of a  $q\bar{q}$  system  
667 and choose to consider the breaking to new  $q'\bar{q}'$  pair closest to this leg. Now the  
668 breaking will produce a hadron  $q\bar{q}'$  and a remainder system spanning from  $q'\bar{q}$ .  
669 Then the process is continued until the  $\bar{q}$ -leg is reached. A small detail here is  
670 that in equation (20) it is assumed that the mass of the remainder system is large.  
671 Thus some patching up is needed for the last two hadrons coming from a string.  
672 The patching up is done such that the place where it happens looks as closely like  
673 any other string break as possible.

674 One additional possibility one must consider is that a string can have such a  
675 low mass that it cannot break at all. In this case a single hadron is generated out  
676 of the string and if necessary energy and momentum are exchanged with other  
677 partons in the event.

678 After all the hadrons are produced, the short-lived ones can still decay before  
679 the set of final state particles in the simulation is obtained []

## 680 Cluster model

681 Instead of a string model HERWIG [] uses a cluster model [65] for hadronisation.  
682 The advantage of cluster models is that they require a smaller number of param-  
683 eters than string models. The model is based on the preconfinement property of  
684 parton showers, i.e. the colour structure of the shower at any evolution scale  $Q_0$  is  
685 such that colour singlet combinations of partons can be formed with an asymptot-  
686 ically universal invariant mass distribution. The invariant mass does not depend

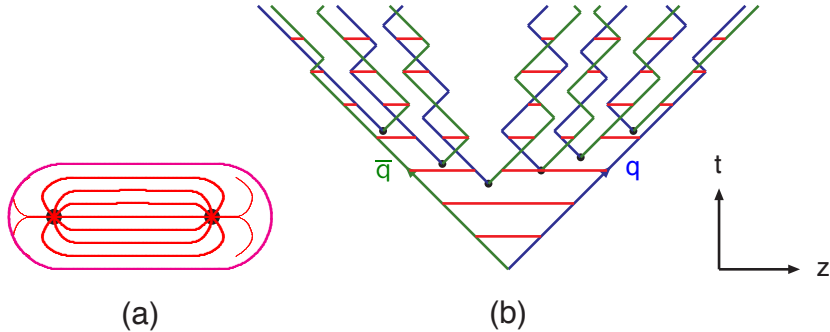


Figure 13: (a) A flux tube spanned between a quark and an antiquark. (b) The motion and breakup of a string system, with the two transverse degrees of freedom suppressed (diagonal lines are (anti)quarks, horizontal ones snapshots of the string field). [64]

on the initial hard process scale  $Q$ , but only on  $Q_0$  and the QCD scale  $\Lambda_{\text{QCD}}$ , when  $Q \gg Q_0$ .

The cluster model starts from transforming all gluons non-perturbatively into  $q\bar{q}$  pairs, which requires that the gluons get a mass, which must be at least twice the lightest quark mass. After the gluons are transformed into quarks, the adjacent colour lines can be clustered together to colour singlet states with mesonic quantum numbers. The momentum of these clusters is defined to be the sum of the momenta of the clustering partons. According to preconfinement, the mass distribution of these clusters is independent of the details of the hard scattering. Additionally the clusters can be regarded as highly excited hadron resonances and decayed into the final state hadrons.

Some of these initial clusters are too heavy to reasonably describe an excited state of a hadron. These must be split before they are allowed to decay. The cluster  $C$  is split if its mass fulfills the condition []

$$M_C^p \geq M_{\max}^p + (m_1 + m_2)^p, \quad (22)$$

where  $m_{1,2}$  are the masses of the constituents partons of the cluster and  $M_{\max}$  and  $p$  are the main parameters of the model. These have to be chosen separately for clusters containing light, charmed and bottom quarks. When a cluster is split, a pair of light quarks is generated from the vacuum and two new clusters are made, both containing one quark from the original cluster and one from the newly generated pair. The splitting is continued until no clusters with masses  $M_C$  fulfilling the equation 22 remains.

When the clusters are light enough, they decay into final state hadrons. If the mass of the cluster is high enough for decaying into a baryon-antibaryon pair,

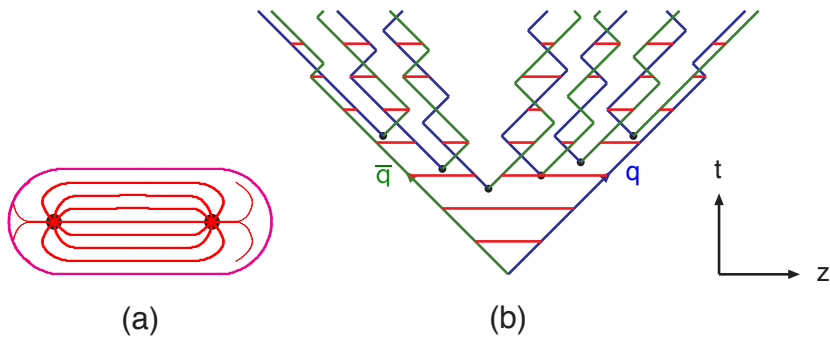


Figure 14: Colour structure of a parton shower to leading order in  $N_c$ . [64]

there is a parameter deciding whether the cluster undergoes mesonic or baryonic decay. For a mesonic decay a quark-antiquark pair is created from the vacuum and for the baryonic decay a diquark-antidiquark pair is made. Then the exact decay products are chosen and the cluster decays isotropically in the rest frame of the cluster. If there are partons produced in the perturbative phase involved in the decay, they retain their original direction in the cluster rest frame, up to some Gaussian smearing. If the cluster mass is too low to decay into a pair of mesons, it decays into the lightest possible hadron and some energy and momentum is exchanged with the adjacent clusters. At the end we are left with the final state hadrons, some of which might still decay until the end of the simulation if they are very short-lived. []

### 1.5.3 Jet energy loss

#### Discovery of jet quenching via leading hadron suppression

First evidence of jet quenching comes from observing high  $p_T$  tracks, i.e. the leading hadrons.

Jet quenching in heavy-ion collisions is usually quantized with the nuclear modification factor  $R_{AA}$ , which is defined as

$$R_{AA}(p_T) = \frac{(1/N_{AA}^{evt}) dN^{AA}/dp_T}{\langle N_{coll} \rangle (1/N_{pp}^{evt}) dN^{pp}/dp_T} \quad (23)$$

where  $dN^{AA}/dp_T$  and  $dN^{pp}/dp_T$  are the yields in heavy-ion and proton-proton collisions, respectively and  $\langle N_{coll} \rangle$  is the average number of binary nucleon-nucleon collisions in one heavy-ion event. The number of binary collisions can be calculated from the Glauber model as shown in Sec. 1.3.2. From the point of view of direct production a heavy-ion collision can be estimated relatively well to be only a series of proton-proton collisions.

If the medium has no effect on high  $p_T$  particles the nuclear modification factor should be 1. At RHIC and LHC this has been observed to be as low as 0.2 because of jet quenching. Measurements of  $R_{AA}$  from different sources are shown in Fig. 15

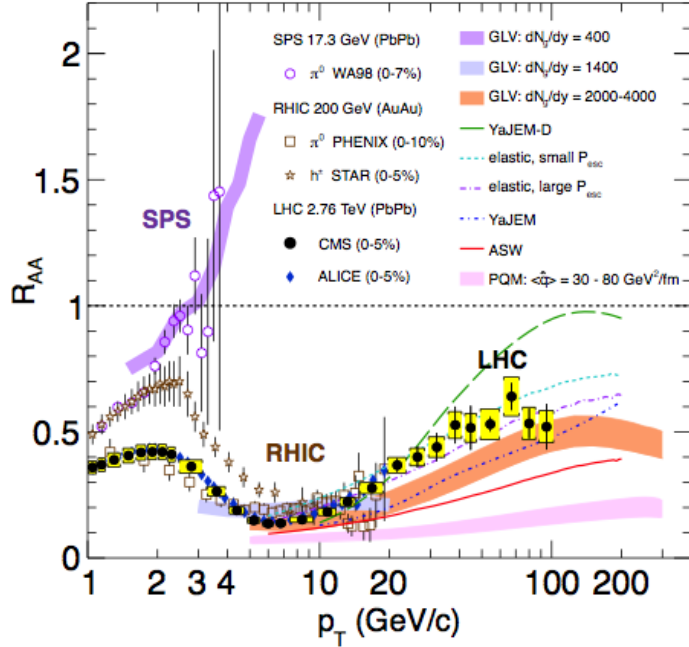


Figure 15: Measurements of the nuclear modification factor  $R_{AA}$  in central heavy-ion collisions at three different center-of-mass energies, as a function of  $p_T$ , for neutral pions ( $\pi^0$ ), charged hadrons ( $h^\pm$ ), and charged particles [66–70], compared to several theoretical predictions [34, 71–75]. The error bars on the points are the statistical uncertainties, and the yellow boxes around the CMS points are the systematic uncertainties. The bands for several of the theoretical calculations represent their uncertainties [76].

The nuclear modification factor can also be used to quantify anisotropy. In the study of anisotropy  $R_{AA}$  in-plane and out-of-plane can be compared. The distance traveled through medium is largest out-of-plane which leads to stronger suppression in this direction. The nuclear modification factor as a function of  $\Delta\phi = \phi - \psi_n$  is given by

$$\begin{aligned}
 R_{AA}(\Delta\phi, p_T) &= \frac{(1/N_{AA}^{evt}) d^2 N^{AA}/d\Delta\phi dp_T}{\langle N_{coll} \rangle (1/N_{pp}^{evt}) dN^{pp}/dp_T} \approx \frac{dN^{AA}/dp_T (1 + 2 \cdot v_2 \cos(2\Delta\phi))}{\langle N_{coll} \rangle dN^{pp}/dp_T} \\
 &= R_{AA}^{incl}(p_T) (1 + 2 \cdot v_2 \cos(2\Delta\phi)). \tag{24}
 \end{aligned}$$

741 The yield of proton-proton collisions is independent of the reaction plane and  
 742 the yield in heavy-ion collisions is modulated by the second harmonics. In Eq. (24)  
 743  $R_{AA}$  is approximated only up to the second harmonics. From Eq. (24) it follows  
 744 that

$$\frac{R_{AA}(0, p_T) - R_{AA}(\pi/2, p_T)}{R_{AA}^{incl}(p_T)} \approx \frac{R_{AA}^{incl}(p_T) (1 + 2 \cdot v_2 - (1 - 2 \cdot v_2))}{R_{AA}^{incl}(p_T)} = 4 \cdot v_2 \quad (25)$$

745 The observed  $R_{AA}(\Delta\phi, p_T)$  from PHENIX measurements in Au-Au collisions at  
 746  $\sqrt{s} = 200\text{GeV}$  [77] is compared to  $R_{AA}$  using  $v_2$  via Eq. (24) in Fig. 16. They  
 agree very well within the statistical errors for all centrality and  $p_T$  bins.

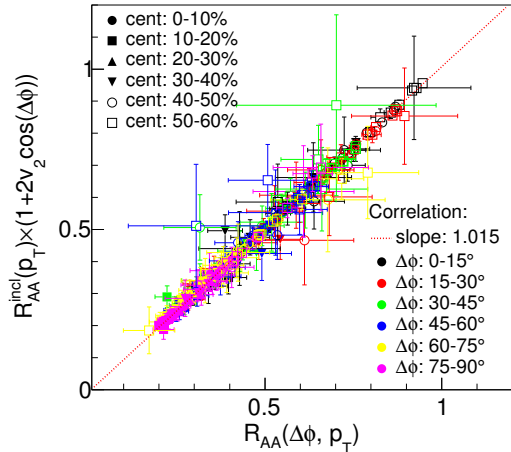


Figure 16: A comparison between observed  $R_{AA}(\Delta\phi, p_T)$  and  $R_{AA}$  using  $v_2$  from PHENIX measurements of Au-Au collisions at  $\sqrt{s} = 200\text{GeV}$ . On the X-axis is the measured  $R_{AA}(\Delta\phi, p_T)$ . On the y-axis is the inclusive  $R_{AA}$  multiplied by  $1 + 2v_2 \cos(\Delta\phi)$  [77].

747  
 748 At high- $p_T$ , the pQCD processes are dominant, hence the  $v_n$  (or  $R_{AA}(\Delta\phi, p_T)$ )  
 749 characterize the pathlength-dependence of the energy loss process.

750 Jet quenching is not the only high  $p_T$  phenomenon studied in heavy-ion colli-  
 751 sions. Another property is jet fragmentation. The high momentum parton created  
 752 in the initial collision fragments into a number of partons with smaller  $p_T$ . Jet  
 753 fragmentation occurs also in proton-proton collisions in the vacuum, but it can  
 754 be modified due to the presence of the medium. In order to study the jet frag-  
 755 mentation function ( $D(z)$ , where  $z = p_T^h/p_T^{part}$ ) modification due the medium, we  
 756 use the two-particle correlations. The particle yield can be extracted from the

correlation function. The background from the flow processes is correlated and needs to be subtracted to get the particle yield associated only with the jet. The ratio of the jet yields in Au-Au and p-p collision  $I_{AA} = Y^{Au+Au}/Y^{p+p}$  characterizes the jet fragmentation modification [78].  $I_{AA}$  probes the interplay between the parton production spectrum, the relative importance of quark-quark, gluon-gluon and quark-gluon final states, and energy loss in the medium.

### Theory of jet quenching

High momentum particles are very rare and they are only produced in the initial collisions. After they are created they escape the medium before a thermal equilibrium is reached. Thus they are not part of the pressure-driven collective expansion. Instead high momentum yield is suppressed because of energy loss in the medium. When propagating through the medium these partons lose energy as they pass through the medium. This is referred to as jet quenching. Jet quenching depends on the path lengths through the medium. Thus anisotropy in this region is mainly dependent on the collision geometry and density of medium.

The energy loss of partons in medium is mainly due to QCD bremsstrahlung and to elastic scatterings between the parton and the medium.

The radiative energy loss mechanism is given in terms of the transport coefficient  $\langle \hat{q} \rangle$ , which describes the average momentum transfer between the medium and parton [79]. The exact definition of this depends on the theoretical formalism used to describe the energy loss mechanism.

Many of the energy loss models exploit the analogy between the QCD interaction of parton propagating through the colored medium and the QED energy loss of electron propagating through material. An electron propagating through matter loses its energy by photon Bremsstrahlung radiation. In the simplest case, each individual scattering center results in a single emission of a photon. This is known as the Bethe-Heitler regime [80]. The energy spectrum of radiated photons  $dN/dE$  is, in this case, proportional to  $1/E$ . However, the Bremsstrahlung photon, can be radiated only when the distance between the scattering centers is larger than the formation length. In the limit, when the scattering centers are closer than the formation length, the Bremsstrahlung process is suppressed. This phenomenon is known as the Landau-Pomeranchuk-Migdal (LPM) [81, 82] suppression. The radiated spectrum in this regime is proportional to  $1/\sqrt{E}$ .

Lower energy photons are further suppressed by the destructive interference leading to the suppression of Bremsstrahlung photons of  $E < \gamma\omega_p$ , where  $\omega_p$  is the plasma frequency of the radiator. This is known as Dielectric suppression. The photon energy distribution in this regime is proportional to the energy of the photon. A schematic view of the effect of these three regimes is shown in Fig. 18.

The simplest energy loss process is elastic QCD scattering off the medium par-

796 tons. In elastic scatterings the recoil energy of the scattered partons are absorbed  
797 by the thermal medium, which reduces the energy of the initial parton. The mean  
798 energy loss from elastic scatterings can be estimated by

$$\langle \Delta E \rangle_{\text{el}} = \sigma \rho L \langle E \rangle_{\text{scatt}} \propto L, \quad (26)$$

799 where  $\sigma$  is the interaction cross section and  $\langle E \rangle_{\text{scatt}}$  is the mean energy transfer  
800 of one individual scattering [84]. This assumption holds if the mean energy is  
801 independent of the total energy of the parton ( $E$ ). The transport coefficient of  
802 elastic scattering,  $\langle \hat{q}_{\text{el}} \rangle = \langle \Delta E \rangle / L$ , is defined as the mean energy los per unit path  
803 length.

804 Another energy loss mechanism is medium-induced radiation. In QCD this  
805 radiation is mainly due to the elementary splitting processes,  $q \rightarrow qg_r$  and  $g \rightarrow gg_r$ .  
806 Assuming that the parton is moving with the speed of light radiation energy loss  
807 can be estimated by

$$\langle \Delta E \rangle_{\text{rad}} \propto T^3 L^2, \quad (27)$$

808 where  $L$  is the length of the medium and  $T$  is its temperature [85]. The differ-  
809 ent exponents of  $L$  in equations 26 and 27 indicate that radiative energy loss is  
810 dominant over elastic energy loss.

811 There are several models that attempt to describe the nature of the energy loss  
812 mechanism. The most used models can be divided into four formalisms.

813 In the Gyulassy-Levai-Vitev (GLV) [86] opacity expansion model the radiative  
814 energy loss is consiered on a few scattering centers  $N_{\text{scatt}}$ . The radiated gluon  
815 is constructed by pQCD calculation as summing up the relevant scattering am-  
816 plitudes in terms of the number of scatterings. Another approach into opacity  
817 expansion is the ASW model by Armesto, Salgado and Wiedermann [87].

818 Thermal effective theory formulation by Arnold, Moore and Yaffe (AMY) [88]  
819 uses dynamical scattering centers. It is based on leading order pQCD hard thermal  
820 loop effective field theory. This model assumes that because of the high temper-  
821 ature of the plasma the strong coupling constant can be treated as small. The  
822 parton propagating through the medium will lose energy from soft scatterings and  
823 hard scatterings.

824 The above models calculate the energy loss while the parton propagates through  
825 the medium, focusing on the pQCD part. The higher twist (HT) approach by Wang  
826 and Guo [89] implements the energy loss mechanism in the energy scale evolution  
827 of the fragmentation functions.

828 The last category is formed by the Monte Carlo methods. The PYTHIA event  
829 generator [90] is widely used in high-energy particle physics. Two Monte Carlo  
830 models based on PYTHIA describing the energy loss mechanism are PYQUEN [91]

831 and Q-Pythia [92]. Other Monte Carlo models include JEWEL [93] and Ya-  
832 JEM [94].

#### 833 1.5.4 New paradigm of jet Quenching

834 As described in the previous section there have been many experimental evi-  
835 dences of jet energy loss, such as the suppression of inclusive hadron spectra at  
836 high transverse momentum [?, ?, ?, ?, ?], the modification of back-to-back hadron-  
837 hadron [?, 78] and direct photon-jet correlations [?], and the modification of recon-  
838 structed jet spectra [?] and jet substructure [?, ?, ?], as compared to the expecta-  
839 tions from elementary proton-proton collisions.

840 The first indications of jet quenching, such as  $R_{AA}$ , looked essentially at the  
841 leading hadrons of jets, the hard part, ignoring the soft scale part of jet phenomena.  
842 However, experimental methods have since improved; jet reconstruction algorithms  
843 have become reliable in the LHC era. Instead of the leading hadron we can study  
844 the entire jet shower.

845 -Jet RAA -Jetscape

846 Thus the new paradigm in jet quenching in heavy-ion collisions involves multi-  
847 scale problems [?, 95]. The elementary scattering and the subsequent branching  
848 process down to non-perturbative scales are dominated by hard scales in the vac-  
849 uum as well as in the medium. Soft scales, of the order of the temperature of  
850 the medium, characterise the interactions of soft partons produced in the shower  
851 with the QGP. Soft scales also rule hadronisation, which is expected to take place  
852 in vacuum for sufficiently energetic probes, even though some modifications can  
853 persist from modifications of color flow [?, ?, ?]. Understanding the contributions  
854 from the different processes to the jet shower evolution in medium and their scale  
855 dependence is crucial to constrain the dynamics of jet energy loss in the expend-  
856 ing medium, the role of colour coherence [?], and fundamental medium properties  
857 like temperature dependent transport coefficient [?, ?].

#### 858 Lund diagram

859 The different momentum and angular scales are subject to different physical phe-  
860 nomena. Figure 19 shows the relevant medium modification phenomena for differ-  
861 ent regions of the phase space at time  $t$ , when a jet propagates through a thermal  
862 cloud of temperature  $T$ . As in practice jets propagate over a finite path-length  
863  $L$  in QCD matter, Fig. 19 can be taken as a representation of the distribution of  
864 partonic jet fragments at moment  $t \approx L$ , when the jet escapes the medium.

865 The region marked as DGLAP is dominated by the primary vacuum splittings.  
866 This region is determined by  $\theta > \theta_{\text{vac}}$  with

$$\theta_{\text{vac}} \propto 1/\sqrt{pt}. \quad (28)$$

867 Medium-induced parton branching fills the log  $p$ -log- $\theta$ -plane from the bottom  
 868 up (in  $p$ ) and from the inside out (in  $\theta$ ). This is because transverse momentum is  
 869 acquired by Brownian motion in the medium,  $k_\perp^2 \propto \hat{q}t$ . Then the formation time  
 870 constraint  $t \geq p/k_\perp^2 \approx p/\hat{q}t$  implies that medium-induced quanta can be formed in  
 871 the region  $p \leq k_{\text{form}}$  where

$$k_{\text{form}}(t) = \hat{q}t^2$$

872 .  
 873 The probability of finding a splittee with a momentum  $p$  with  $p < k_{\text{form}}$  is

$$\frac{dP_{\text{find}}(t)}{d \log p} \propto \alpha_s t/t_{\text{form}}(p) \propto \alpha_s \hat{q}^{nicefrac{1}{2}} p^{-1/2} t \quad (29)$$

874 Not all quanta will stay where they were created. Those modes that have time  
 875 to lose a significant fraction of their energy will cascade to a significantly lower  
 876 scale  $p$ . For LPM-type radiation, the splitting that degrades energy the most is  
 877 the hardest splitting.

878 The  $\log p$  distribution has the same  $\frac{1}{\sqrt{p}}$  dependence as in the LPM region

$$\frac{dn}{d \log p} = \frac{1}{p} \frac{d\epsilon}{d \log p} \approx \alpha_s \frac{\sqrt{\hat{q}t}}{\sqrt{p}} \quad (30)$$

879 Also the quanta originating from the DGLAP region will undergo medium  
 880 interactions that will make the quanta radiate and split. The distribution of radi-  
 881 ation is the same as from any other mode. Above a certain momentum scale  $k_{\text{split}}$   
 882 the distribution of originating daughters is

$$\frac{dP_{\text{find}}}{d \log p d \log \theta} \approx \alpha_s \frac{t}{t_{\text{split}}(p)}, \quad (31)$$

883 Note that the ratio  $t/t_{\text{split}}$  is smaller than 1 for nodes above  $k_{\text{split}}$  and therefore  
 884 the number of daughters is smaller than the number of vacuum splitted quanta.  
 885 Below  $k_{\text{split}}$  the cascade is similar to the medium cascade and the number of quanta  
 886 become

$$\frac{dn}{d \log p d \log \theta} \approx \alpha_s \frac{t}{t_{\text{split}}(p)}, \text{ for } p < k_{\text{split}}(p) \quad (32)$$

887 The angular distribution is driven by two mechanisms; Multiple soft scatterings  
 888 give rise to transverse Brownian motion, which determines the distribution at small  
 889 angles. The typical angle reached in the LPM region is

$$\theta_{\text{BR}}(p) \approx \frac{\sqrt{\hat{q}t}}{p}, \text{ for } k_{\text{form}} > p > k_{\text{split}}, \quad (33)$$

890 while in the medium cascade region of the phase space this becomes

$$\theta_{\text{BR}}(p) \approx \left(\frac{T}{p}\right)^{\frac{3}{4}} \quad (34)$$

891 Large angular scales cannot be reached by Brownian motion, but can arise from  
892 rare large angle scatterings, described by Molière [].

## 893 1.6 QGP in Small systems

894 After the existence of QGP in heavy ion collisions has been established, attention  
895 has been turned to small systems. Proton-proton (pp) and proton-Lead (pPb)  
896 collisions have been studied at LHC and RHIC has studied a host of different  
897 collision systems; namely proton-Gold (pAu), deuteron-Gold (dAu) and Helium<sup>3</sup>-  
898 Gold (He<sup>3</sup>Au) collisions starting in 2000.

899 Already before the era of modern colliders, collective behaviour in proton-  
900 proton collisions was considered by names like Heisenberg, Fermi and Bjorken. [96]  
901 Eventually there were some experimental searches of QGP in pp and  $p\bar{p}$  collisions  
902 in E735 at Tevatron [97] and MiniMAX [98]. However no conclusive evidence was  
903 found.

904 In the early years of RHIC these small systems were mostly considered as con-  
905 trol measurement, for example in constraining nuclear modified parton distribution  
906 functions (nPDFs) that determine the initial gluon distributions that determine  
907 the first epoch of heavy ion collisions [99, 100].

908 In 2010 ultrahigh-multiplicity pp collisions were studied at CMS. The study  
909 found that particles had a weak but clear preference to be emitted along a com-  
910 mon transverse  $\phi$  angle across all rapidities [101]. This seemed like behaviour  
911 were similar to AA collisions, but it was argued that it could as well come from  
912 momentum correlations present in the earliest moments of the collision.

913 In 2012 LHC ran its first pPb data taking period. Around the same time  
914 dAu data was reexamined at RHIC. Now it was revealed that most of the flow  
915 signatures attributed to hydrodynamic expansion in AA collisions also existed in  
916 smaller systems.

917 -Sub nucleonic structure needed to describe intial conditions in pA, pp

### 918 1.6.1 Collective phenomena

919 The most rugged analysis of collective behaviour concerns the two (or more) parti-  
920 cle correlations, often parametrised via the relative azimuthal angle and pseudora-

921 pidity differences,  $\Delta\phi$  and  $\Delta\eta$  respectively. Figure 21 shows two-particle correla-  
922 tions measurements in PbPb, pPb and pp collisions at the LHC. In PbPb collisions  
923 long-range correlations dominate over short-range phenomena. This shows in the  
924 two ridges at  $\Delta\phi = 0$  and  $\Delta\phi = \pi$ . At  $\Delta\phi \approx \Delta\eta \approx 0$ , there is a peak coming from  
925 single jet fragmentation. Since the away-side jet can be spread out in  $\Delta\eta$ , this  
926 contribution disappears when compared to the flow contribution at the away side  
927 ridge. In pPb, and pp the near side peak is more distinguished and the away-side  
928 jet contribution starts to show. Still, one can see long-range correlations that seem  
929 like flow-like collective behaviour in both systems.

930 In addition to the two particle correlations, correlations have been observed in  
931 the form of  $v_n$  coefficients both at LHC and at RHIC. The results have also been  
932 described with hydrodynamical models, although the applicability of said models  
933 is questionable, because of the large Reynolds numbers in small systems. Figure  
934 20 shows results for  $v_2$  in different collisions systems at RHIC as measured by  
935 PHENIX. These different systems provide also different initial geometries. dAu  
936 collisions naturally have an ellipsoidal form, while a He3 collision has a triangular  
937 form and thus produces larger triangular flow,  $v_3$  components.

938 Other observations that produce flow-like results include mass ordered  $v_2$  coeffi-  
939 cients and higher order harmonics coming from fluctuations in the initial geometry.  
940 Thus all the major collective flow phenomena observed in heavy-ion collisions have  
941 been also identified in small systems.

942 One open question is identifying the point the point, where flow-like correla-  
943 tions end. The question has proved challenging since low multiplicity events are  
944 dominated by non-flow phenomena. This makes observations in low multiplicity  
945 events model/method dependant. Different methods assess non-flow contributions  
946 differently. Thus some methods fail to observe a signal in cases, where others do  
947 and it is unclear whether this is true collective motion or it comes from non-flow  
948 contributions.

#### 949 1.6.2 Absence of jet quenching

950 In A+A collisions, an important confirmation of the standard model comes from  
951 the energy loss of high  $p_T$  partons traversing the medium, referred to as jet quench-  
952 ing [102–104]. In 2003 the jet quenching effect was observed to disappear in d+Au  
953 collisions. This was taken as an indication that no QGP was created. Similarly at  
954 LHC no jet modification has been observed in pPb collisions. Fig. 22 shows the  
955 nuclear modification factor  $R_{pA}$  in pPb collisions as measured at the LHC.

956 The lack of jet modification seems surprising considering the multitude of flow  
957 observations supporting the existence of QGP in small systems. One possible  
958 explanation is simply the size of medium. In PbPb collision partons traversing  
959 through the medium lose energy to the medium. If the medium is very small there

960 is limited time for interaction with the medium.

961 Calculations indicate that there should be modification in the most central  
962 pPb collisions, but selecting these in the analysis is complicated. In PbPb colli-  
963 sions most of the particle production comes from the medium and thus the total  
964 multiplicity is a good indicator of centrality. In pPb collisions, however the total  
965 multiplicity is smaller and is more strongly influenced by jet phenomena. Events  
966 with jets have naturally larger multiplicities and are more likely to be classified as  
967 central events.

968 So far the only observable indicative of jet quenching in pPb collisions is the  
969 high  $p_T v_2$ . In heavy-ion collisions this is not explained by hydrodynamics. Instead  
970 it is assumed to come from jet quenching with different path lengths through the  
971 medium in different directions. In Fig.22 ATLAS and CMS measurements of  $v_2$  in  
972 pPb and PbPb collisions are shown. The pPb results seem to follow a very similar  
973 pattern. But

Table 1: Summary of observations in small system

Observable	PbPb	pPb	pp
Jet RpA/RAA	Modified	No modification	-
Hadron RpA/RAA	Modified	No modification	-
Heavy flavors			
Jet shape	Broadening	No observations	-
Two-particle correlations	Ridge	Ridge	Ridge
$v_2$	Observed	Observed	Observed
Mass ordered flow			
Higher ordered harmonics			
High $p_T v_2$	Observed	Maybe	-

### 974 1.6.3 Centrality determination in small systems

975 In lead-lead collisions the total multiplicity of the event is a good indicator of the  
976 centrality of the collision. In proton-lead collisions the connection of multiplicity  
977 and centrality is less clear. In p–Pb collisions the impact parameter is only  
978 loosely correlated to  $N_{\text{part}}$  or  $N_{\text{coll}}$ . Hence, although one uses traditionally the  
979 term centrality to refer to these measurements, the relevant parameters are  $N_{\text{part}}$   
980 and  $N_{\text{coll}}$  [1].

981 The Glauber model [?] is generally used to calculate geometrical quantities of  
982 nuclear collisions (A–A or p–A). In this model, the impact parameter  $b$  controls the  
983 average number of participating nucleons  $N_{\text{part}}$  and the corresponding number of  
984 collisions  $N_{\text{coll}}$ . It is expected that variations of the amount of matter overlapping

985 in the collision region will change the number of produced particles, and parameters  
986 such as  $N_{\text{part}}$  and  $N_{\text{coll}}$  have traditionally been used to describe those changes  
987 quantitatively, and to relate them to ppcollisions.

988 The problem in p–Pb collisions, is that fluctuations in multiplicity coming from  
989 for example hard scatterings are of the same order as the differences in multiplicity  
990 between centrality classes. In Pb–Pb collisions these multiplicity fluctuations have  
991 little influence on the centrality determination, the range of  $N_{\text{part}}$  or  $N_{\text{coll}}$  is large  
992 and  $P(M|v)$  converges quickly to a Gaussian with a small width relative to the  
993 range of  $v$ .

994 Thus in practice selecting high multiplicity one chooses not only large average  
995  $N_{\text{part}}$ , but also positive multiplicity fluctuations leading to deviations from the  
996 binary scaling of hard processes. These fluctuations are partly related to qualita-  
997 tively different types of collisions. High multiplicity nucleon-nucleon collisions  
998 show a significantly higher particle mean transverse momentum. They can be  
999 understood as harder collisions with larger momentum transfer  $Q^2$  or as nucleon-  
1000 nucleon collisions where multiple parton-parton interactions (MPI) take place.  
1001 This is illustrated in Fig. 24.

1002 Of particular interest are estimators from kinematic regions that are causally  
1003 disconnected after the collision. The measurement of a finite correlation between  
1004 them unambiguously establishes their connection to the common collision ge-  
1005 ometry. Typically these studies are performed with observables from well sep-  
1006 arated pseudorapidity ( $\eta$ ) intervals, e.g. at zero-degree (spectators, slow-nucleons,  
1007 deuteron break-up probability) and multiplicity in the rapidity plateau.

1008 One centrality selection that is argued not to induce a bias on the binary scaling  
1009 of hard processes is provided by the energy measurement with the Zero Degree  
1010 Calorimeters (ZDC) in ALICE, due to their large  $\eta$ -separation from the central  
1011 barrel detectors. They detect the "slow" nucleons produced in the interaction by  
1012 nuclear de-excitation processes or knocked out by wounded nucleons.

1013 Additional kinematic biases exist for events containing high- $p_{\text{T}}$  particles, which  
1014 arise from the fragmentation of partons produced in parton-parton scattering with  
1015 large momentum transfer. Their contribution to the overall multiplicity increases  
1016 with increasing parton energy and thus can introduce a trivial correlation between  
1017 the centrality estimator and the presence of a high- $p_{\text{T}}$  particle in the event. For the  
1018 very peripheral collisions, the multiplicity range that governs the centrality for the  
1019 bulk of soft collisions can represent an effective veto on hard processes. For the  
1020 nuclear modification factor this would lead to  $R_{\text{pPb}} < 1$ .

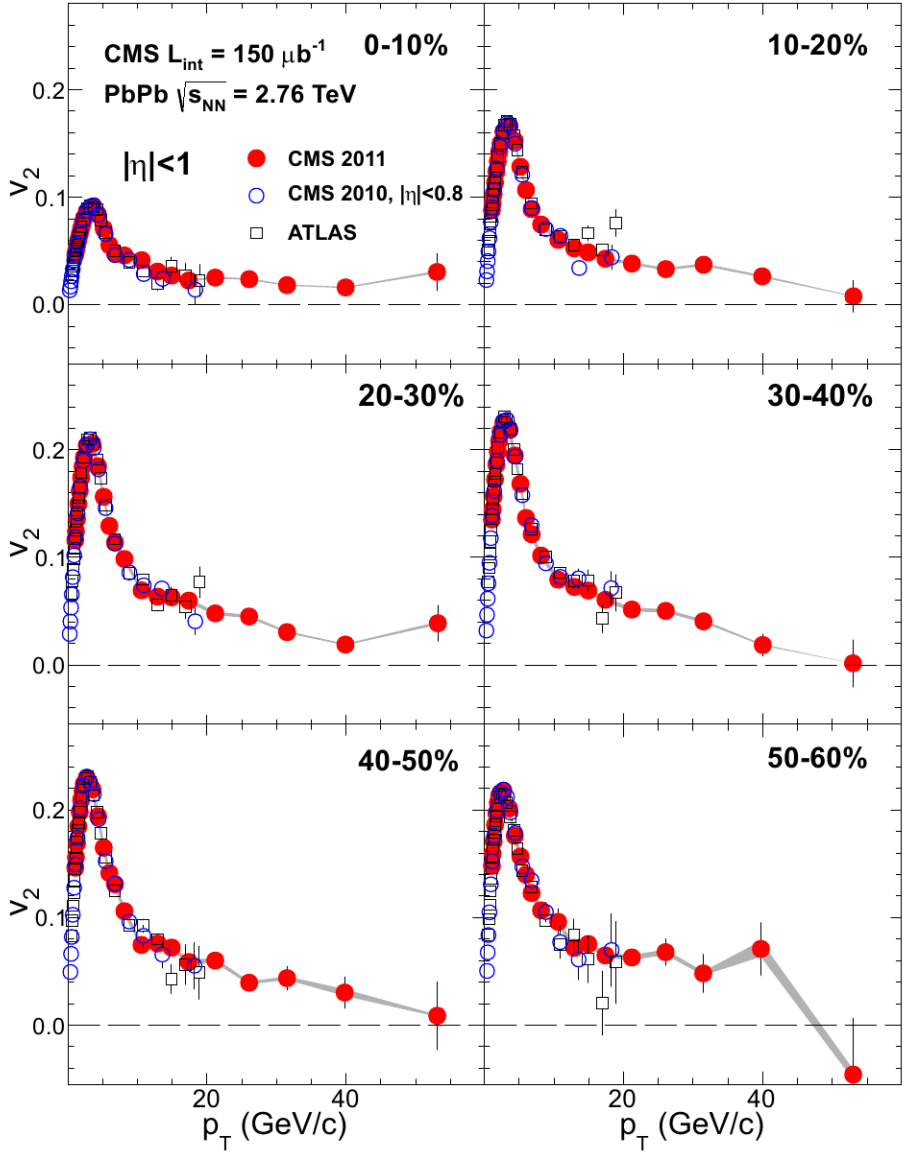


Figure 17: Elliptic flow,  $v_2$ , as a function of the charged particle transverse momentum from 1 to 60  $\text{GeV}/c$  with  $|\eta| < 1$  for six centrality ranges in Pb-Pb collisions at  $\sqrt{s_{NN}} = 2.76 \text{ TeV}$ , measured by the CMS experiment. [61].

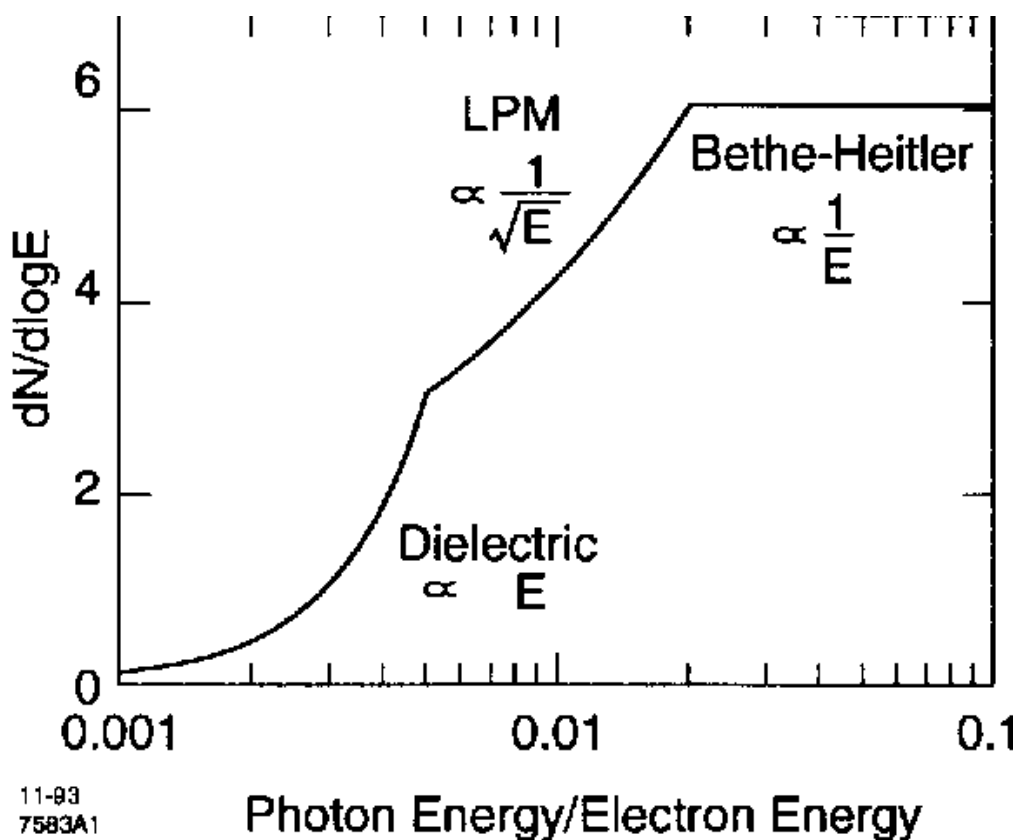


Figure 18: The expected bremsstrahlung spectrum for a electron propagating through material. [83].

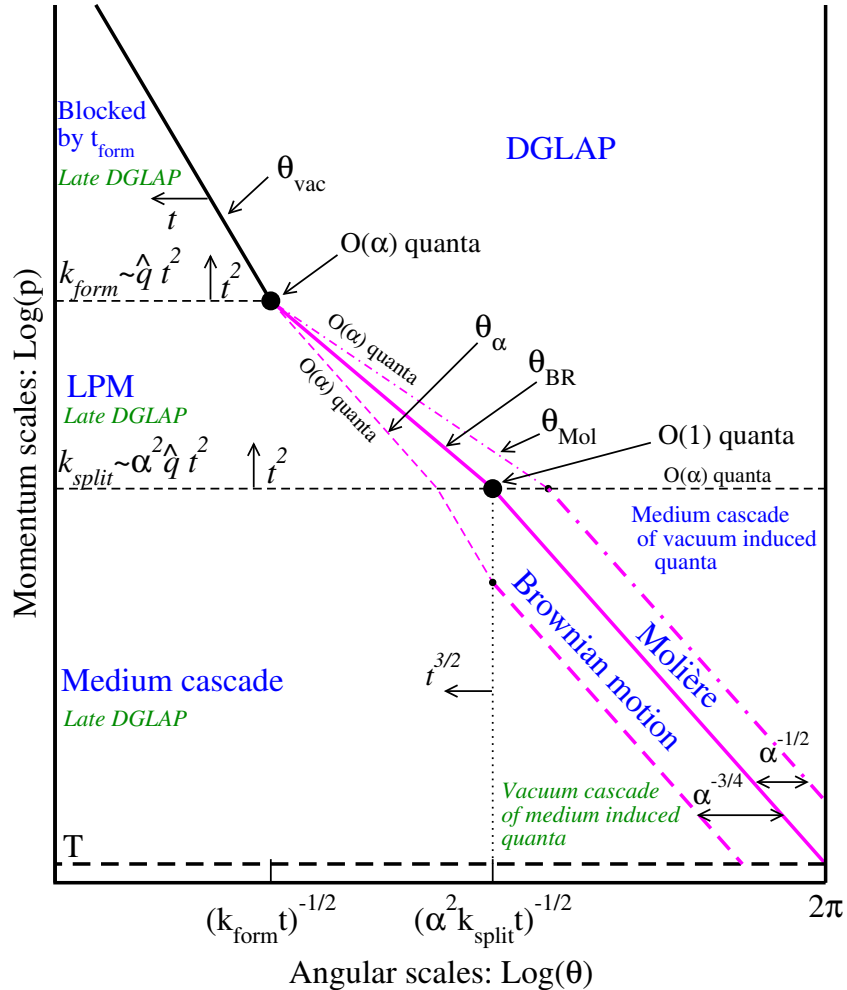


Figure 19: Parametrically accurate picture of how a medium-modified parton cascade fills the phase space. At time  $t$ , quanta can be formed up to momentum scale  $k_{\text{form}}$  and they are formed with  $O(1)$  probability per  $\log p$  at lower scale  $k_{\text{split}}$ . Quanta below  $k_{\text{split}}$  split further and their energy cascades to the thermal scale  $T$  in less than an epoch  $t$ . Transverse Brownian motion moves quanta up to the angle  $\theta_{\text{BR}}(p)$  denoted by the thick purple line. The Molière region at larger  $\theta$  is dominated by rare large angle scattering. At even larger angle, there are  $O(\alpha_s)$  quanta per double logarithmic phase space from DGLAP ‘vacuum’ radiation, and for momenta below  $k_{\text{split}}$  these cascade within time  $t$  to  $T$ . After the jet escapes the medium, the jet and the emitted fragments will undergo vacuum radiation. This late time vacuum radiation emitted by the original parton dominates at sufficiently small  $\log \theta$  (regions marked “late DGLAP” and bounded by  $\theta_{\text{vac}}$  and  $\theta_\alpha$ ), whereas the late time radiation of the fragments dominates in the region denoted by “Vacuum cascade of the medium induced quanta”. [95].

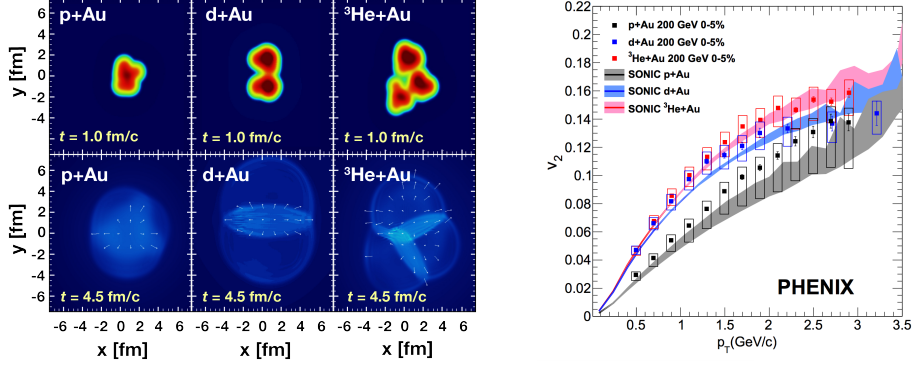


Figure 20: Calculations of the intial energy density in small collision systems at RHIC and the resulting hydrodynamic evolution.

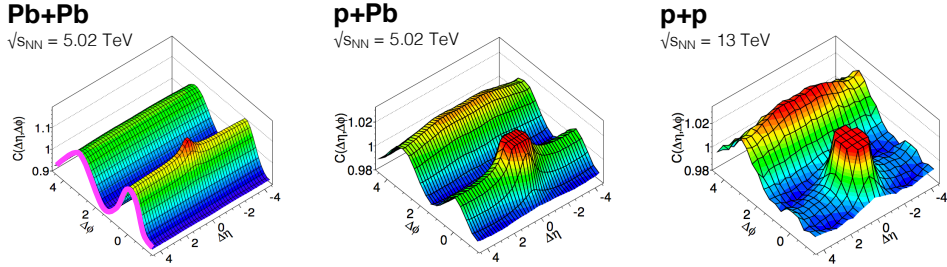


Figure 21: Two-particle correlation results in PbPb, pPb, and pp collisions at the LHC [1].

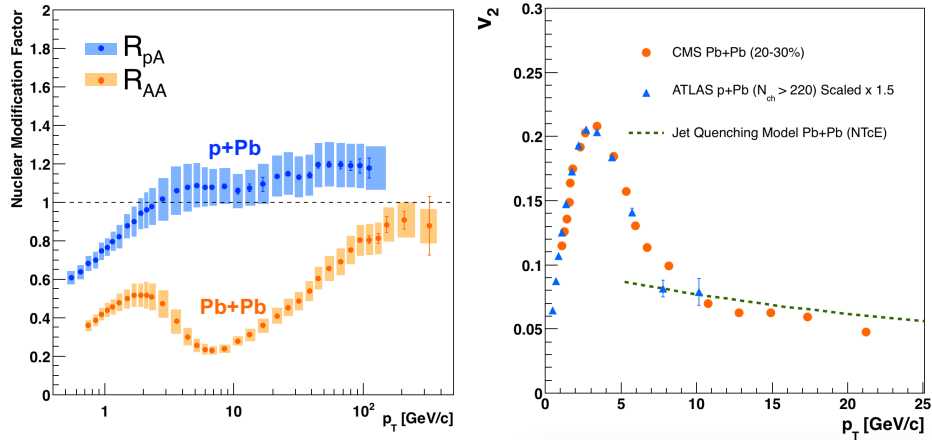


Figure 22: RpA in proton-lead collisions

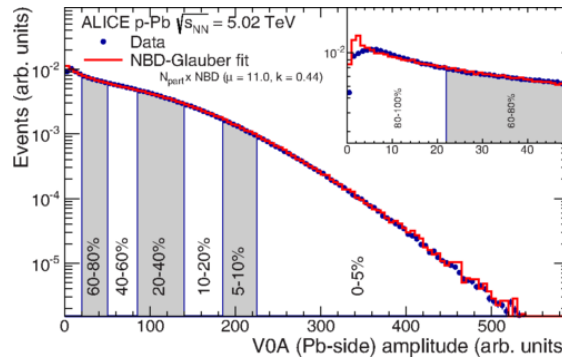


Figure 23: Distribution of the sum of amplitudes in the V0A hodoscopes (Pb-going), as well as the NBD-Glauber fit (explained in the text). Centrality classes are indicated by vertical lines. The inset shows a zoom-in on the most peripheral events. [1]

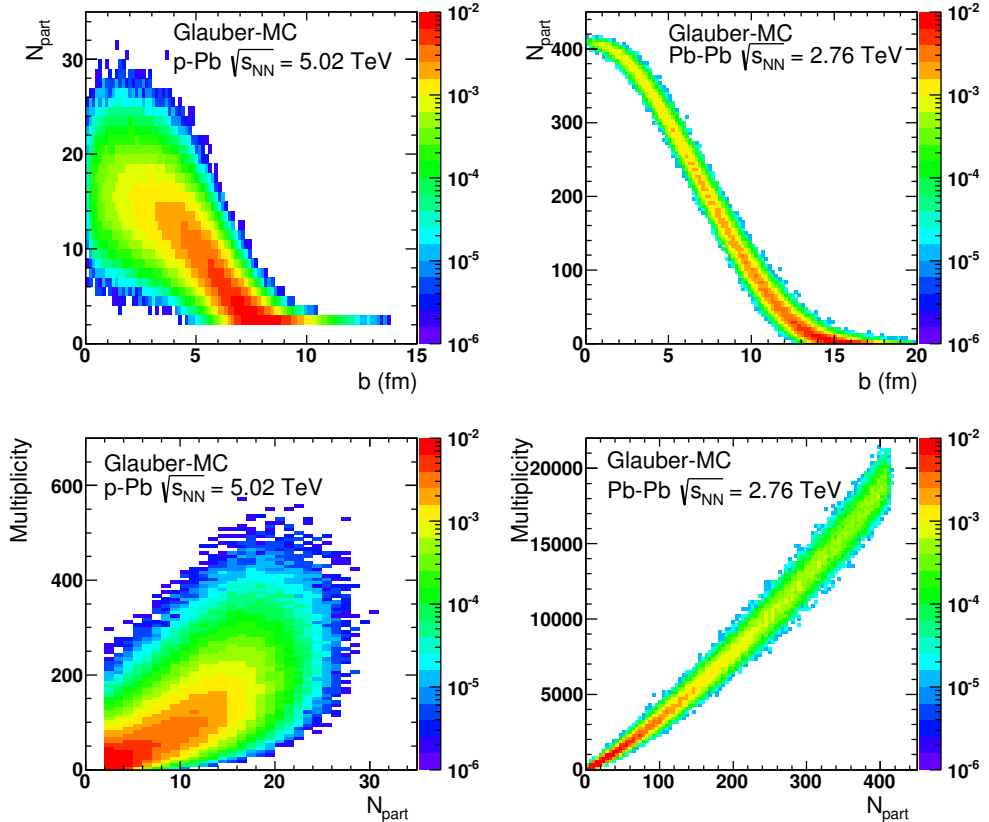


Figure 24: Top: Scatter plot of number of participating nucleons versus impact parameter; Bottom: Scatter plot of multiplicity versus the number of participating nucleons from the Glauber fit for V0A. The quantities are calculated with a Glauber Monte Carlo of p-Pb (left) and Pb-Pb (right) collisions. [1]

## 1021 2 Experimental Details

### 1022 2.1 CERN

1023 The European Organization for Nuclear Research (CERN) is the largest particle  
1024 physics laboratory in the world. CERN was founded in 1954. In 2019 CERN  
1025 consists of 22 member states. Additionally CERN has contacts with a number  
1026 of associate member states and various individual institutions. Some 12000 vis-  
1027 iting scientists from over 600 institutions in over 70 countries come to CERN for  
1028 their research. CERN itself is located near Geneva at the border of France and  
1029 Switzerland and itself employs about 2500 people.

1030 The laboratory includes a series of accelerators, which are used to accelerate  
1031 the particle beams used. A schematic view of the complex as of 2019 is shown  
1032 in Figure ???. In the framework of this thesis the main component is the Large  
1033 Hadron Collider (LHC), the largest collider at CERN. LHC will be discussed in  
1034 the chapter in more detail. Other accelerators in the series are used to inject the  
1035 particle beam into LHC, but they are also used in itself for various experimental  
1036 studies.

1037 The second largest accelerator is the super proton synchrotron (SPS). It is final  
1038 step before the particle beam is injected into LHC. Commissioned in 1976, it was  
1039 the largest accelerator at CERN until the the Large Electron-Positron Collider  
1040 (LEP) was finished in 1989. Originally it was used as a proton-antiproton collider  
1041 and as such provided the data for the UA1 and UA2 experiments, which resulted in  
1042 the discovery of the W and Z bosons. At the moment there are several fixed target  
1043 experiments utilising the beam from SPS. These study the structure (COMPASS)  
1044 and properties (NA61/SHINE) of hadrons, rare decays of kaons (NA62) and radi-  
1045 ation processes in strong electromagnetic fields (NA63). Additionally the AWAKE  
1046 and UA9 experiments are used for accelerator research and development.

1047 -PS

### 1048 2.2 Large Hadron Collider

1049 The Large Hadron Collider (LHC) is the largest accelerator at CERN and the  
1050 largest particle collider ever built. The LHC is designed to accelerate protons  
1051 up to an energy of 8 TeV and lead ions up to 2.76 TeV per nucleon [?]. The design  
1052 luminosity of the LHC is  $10^{34} \text{ cm}^{-2} \text{s}^{-1}$ . In 20xx it achieved a record peak luminosity  
1053 of xxx. For lead beams the design luminosity is xxx. All this is achieved with a  
1054 ring of 26.7 km, that consists of 1232 superconducting dipole magnets that keep  
1055 particles in orbit.

1056 The particles are accelerated through the use of radio-frequency (RF) cavities.  
1057 The RF are build such that the electromagnetic waves become resonant and build

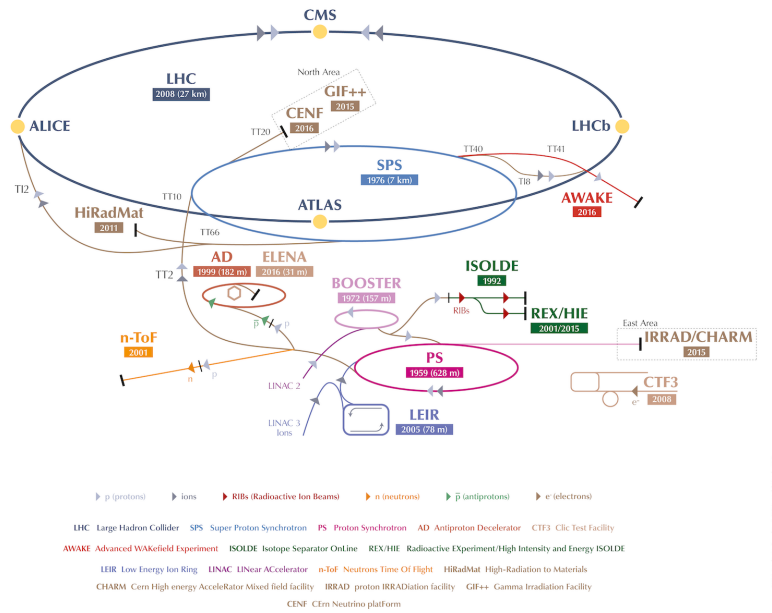


Figure 25: A schematic view of the accelerator complex at CERN. Before particles can be injected into the LHC they require a series of preliminary? acceletarors. Until 2018 protons start their journey in LINAC2 (Linear Accelerator) and continue through the Booster, Proton Synchrotron (PS) and Super Proton Synchrotron (SPS). Between 2019 and 2020 LINAC2 will be replaced by LINAC4 [105]

1058 up inside the cavity. Charges passing through the cavity feel the overall force  
1059 and are pushed forward along the accelerator. As they consist of electromagnetic  
1060 waves, the field in the RF cavity oscillates. Thus particles must enter the cavity at  
1061 the correct phase of oscillation to receive a forward push. When timed correctly,  
1062 the particles will feel zero accelerating voltage when they have exactly the correct  
1063 energy. Particles with higher energies will be decelerated and particles with lower  
1064 energies will be accelerated. This focuses particles in distinct bunches. The RF  
1065 oscillation frequency at the LHC is 400.8 MHz. Thus RF "buckets" are separated  
1066 by 2.5 ns. However only 10 % are actually filled with particles, so the bunch  
1067 spacing in the LHC is 25 ns, at a bunch frequency of 40 MHz.

1068 With 7 TeV proton beams the dipole magnets used to bend the beam must  
1069 produce a magnetic field of 8.33 T. This can be only achieved through making  
1070 the magnets superconducting, which requires cooling them down with helium to a  
1071 temperature of 1.9 K. The 1232 dipole magnets make up roughly 2/3 of the LHC  
1072 circumference. The remaining part is made up of RF cavities, various sensors and  
1073 higher multipole magnets used to keep the beam focused. The most notable of  
1074 these are the 392 quadrupole magnets.

1075 The LHC is divided into octants, where each octant has a distinct function.  
1076 Octants 2 and 8 are used to inject beam into the LHC from SPS. The 2 beams  
1077 are crossed in octants 1,2,5 and 8. The main experiments are built around these  
1078 crossing points. Octants 3 and 7 are used for beam cleansing. This is achieved  
1079 through collimators that scatter particles with too high momentum or position  
1080 offsets off from the beam. The RF cavities used for acceleration are located in  
1081 octant 4 and octant 6 is used for dumping the beam. The beam dump is made  
1082 up of two iron septum magnets, one for each beam, that will kick the beam away  
1083 from machine components into an absorber when needed.

### 1084 2.2.1 LHC experiments

1085 As of 2018 there are four main experiments at the LHC; ALICE, ATLAS, CMS  
1086 and LHCb and three smaller ones LHCf, TOTEM and MoEDAL. ALICE will be  
1087 covered in section 2.3.

1088 ATLAS (A Toroidal LHC ApparatuS) and CMS (Compact Muon Solenoid) are  
1089 the two largest experiments at the LHC. They are both multipurpose experiments  
1090 designed to be sensitive to many different possible new physics signals. The biggest  
1091 discovery made by these so far is the discovery of the Standard Model Higgs boson,  
1092 which was simultaneously published by the experiments in 2012 [?,?].

1093 The LHCb (LHC beauty) experiment [?] is made for studying the bottom  
1094 (beauty) quark. Main physics goals include measurement of the parameters of CP  
1095 violation with decays of hadron containing the bottom quark. One of the most  
1096 important results published by LHCb is the first measurement of  $B_s^0 \rightarrow \mu^+ \mu^-$

1097 decay, which was found to be in line with the Standard Model.

1098 In addition to the four large experiments there are three smaller experiments  
1099 along the LHC ring. LHCf (LHC forward) is located at interaction point 1 with  
1100 ATLAS. It aims to simulate cosmic rays by the particles thrown forwards by the  
1101 collisions in ATLAS.

1102 TOTEM (TOTal Elastic and diffractive cross section Measurement) is located  
1103 near the CMS experiment at point 5. This allows it to measure particles emerging  
1104 from CMS with small angles. The main goals is to measure the total, elastic and  
1105 inelastic cross-sections in pp collisions [?].

1106 The MoEDAL (Monopole and Exotics Detector At the LHC) experiment is  
1107 located at the interaction point 8 together with the LHCb experiment. MoEDAL  
1108 tries to measure signatures of hypothetical particles with magnetic charge, mag-  
1109 netic monopoles.

## 1110 2.3 ALICE

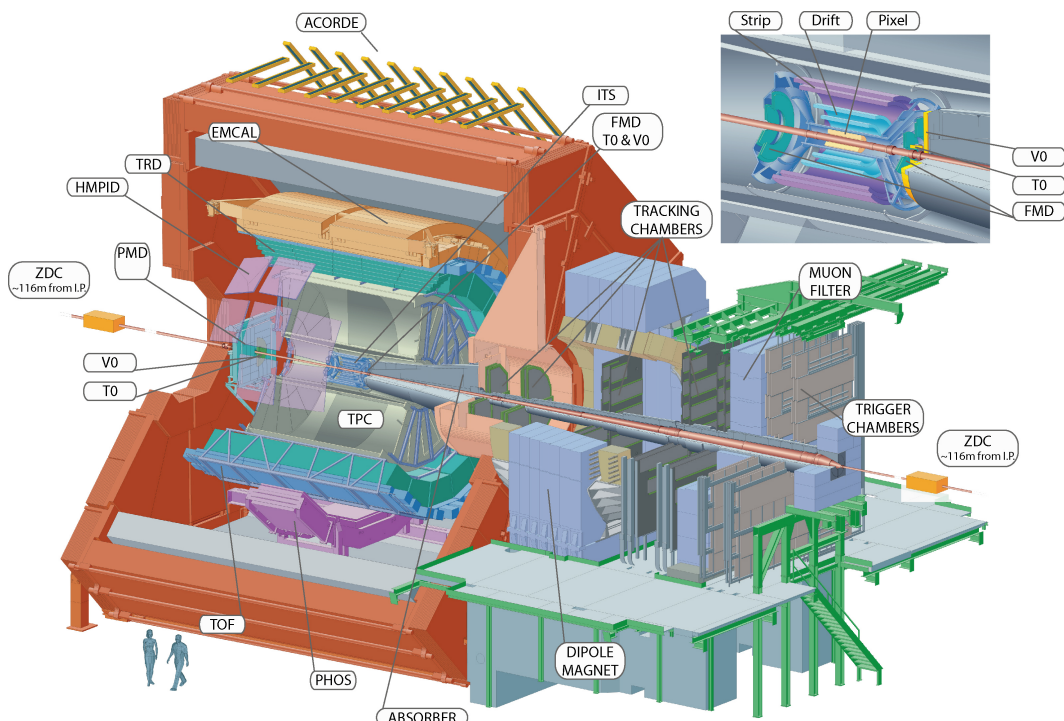


Figure 26: Schematic view of ALICE

1111 ALICE (A Large Ion Collider Experiment) [106] is the dedicated heavy ion  
1112 experiment at the LHC. ALICE was designed to cope with the expected very high  
1113 multiplicity environment of heavy ion collisions. The design allows measurement

of a large number of low momentum tracks. The different detector subsystems are optimised to provide high momentum resolution and excellent particle identification capabilities over a broad range of momentum.

A schematic view of the ALICE detector in 2018 is presented in Figure 26. This section will go through the composition of ALICE as it has been during run 2 between 2014 and 2018. The detector will go through significant upgrades during Long Shutdown 2 in 2019-2020. As in all the major high energy physics experiments the positioning of the detectors follows a layered structure. Closest to the interaction point are the tracking detectors. The main task of these detectors is to locate the position of the primary interaction vertex accurately and to record the tracks of charged particles. To achieve this they need a very good spatial resolution close to the interaction point. Tracking detectors do not significantly alter the tracks of traversing particles. Thus they can be located in the innermost layers.

Calorimeters are designed to stop any particles hitting them and use the absorption to measure the energy of the particles. Thus they must be located behind the tracking detectors. ALICE has two separate calorimeter systems, the electromagnetic calorimeters measure mainly electrons and photons, while the muon detection system measures muons.

### 2.3.1 Tracking

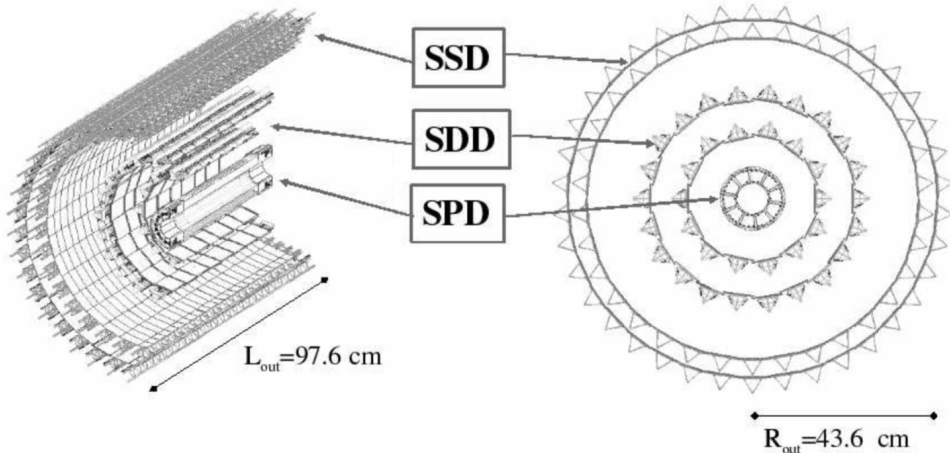


Figure 27: Schematic view of ALICE Inner Tracking System

The main design guideline for the tracking detectors in ALICE was the requirement to have good track separation and high granularity in the high multiplicity environment of heavy ion collisions. Before LHC was built the wildest estimates

1137 put the particle density at 8000 charged particles per unit of rapidity ].. In real-  
1138 ity the particle density turned out to be significantly smaller, about 1600 charged  
1139 particles per rapidity unit. ]

1140 The main tracking detector in ALICE is the Time Projection Chamber (TPC),  
1141 discussed in more detail in section 2.3.2

1142 Between TPC and the beam pipe there is an array of six layers of silicon detec-  
1143 tors, called the inner tracking system (ITS) [?]. The main tasks of the ITS are to  
1144 locate the primary vertex with a resolution better than  $100\ \mu m$ , to reconstruct the  
1145 secondary vertices from decaying particles, to track and identify particles with mo-  
1146 mента below 200 MeV and to compliment the momentum and angle measurements  
1147 of TPC. During long shutdown 2 in 2019-2020 the entire ITS will be replaced [?].  
1148 As of 2018 the two innermost layers are made of the silicon pixel detector (SPD).  
1149 As it's the closest detector to the interaction point it requires are very high spatial  
1150 resolution. Thus the choice of pixel technology is natural. In heavy ion collisions  
1151 the particle density is around 50 particles per  $cm^2$ .

1152 The next two layers are the silicon drift detector (SDD), which is made out of  
1153 homogeneous neutron transmutation doped silicon. It is ionized when a charged  
1154 particle goes through the material. The generated charge then drifts to the col-  
1155 lection anodes, where it is measured. The maximum drift time in SDD is about 5  
1156  $\mu s$  This design gives very good multitrack capabilities and provides two out of the  
1157 four  $dE/dx$  samples in the ITS.

1158 The two remaining layers in the ITS are the silicon strip detector (SSD). The  
1159 strips work in a similar way as silicon pixels, but by itself one layer only provides  
1160 good resolution in one direction. Combining two crossing grids of strips provides 2  
1161 dimensional detection. Each charged particle will hit two intervening strips. The  
1162 position of the hit can be deduced from the place where the strips cross each other.

### 1163 2.3.2 TPC

1164 Time projection chamber (TPC) is a cylindrical detector filled with  $88m^3$  of  
1165 Ne – CO<sub>2</sub> (90/10 %) gas mixture. The gas is contained in a field cage that provides  
1166 an uniform electric field of  $400V/cm$  along the z-axis (along the beam direction).  
1167 Charged particles traversing through the TPC volume will ionise the gas along  
1168 their path. This liberates electors that drift towards the end plates of the cylin-  
1169 der.

1170 The field cage is separated into two detection volumes by the central high  
1171 voltage electrode. Both sides have a drift length of 2.5 m and inner/outer diameters  
1172 of 1.2/5 m. This means the central electrode must provide a maximum potential  
1173 of 100 kV to achieve the design field magnitude. The maximum time required for  
1174 electrons to drift through the chamber is about 90  $\mu s$ .

1175 When electrons reach the end of the main cylinder they enter the readout

1176 chambers. The readout section of both sides consists of 18 outer chambers and  
1177 18 inner chambers. Each of them are made of multiwire proportional chambers  
1178 with cathode pad readout. This design is used in many TPCs before. During  
1179 Long Shutdown 2 in 2019-2020, the multiwire chambers will be replaced by Gas  
1180 Electron Multipliers (GEMs, see section 2.3.3).

1181 The relatively slow drift time of  $90 \mu\text{s}$  is the limiting factor for the luminosity  
1182 ALICE can take. The occupancy of the TPC must be kept in a manageable level.

1183 **2.3.3 TPC upgrade**

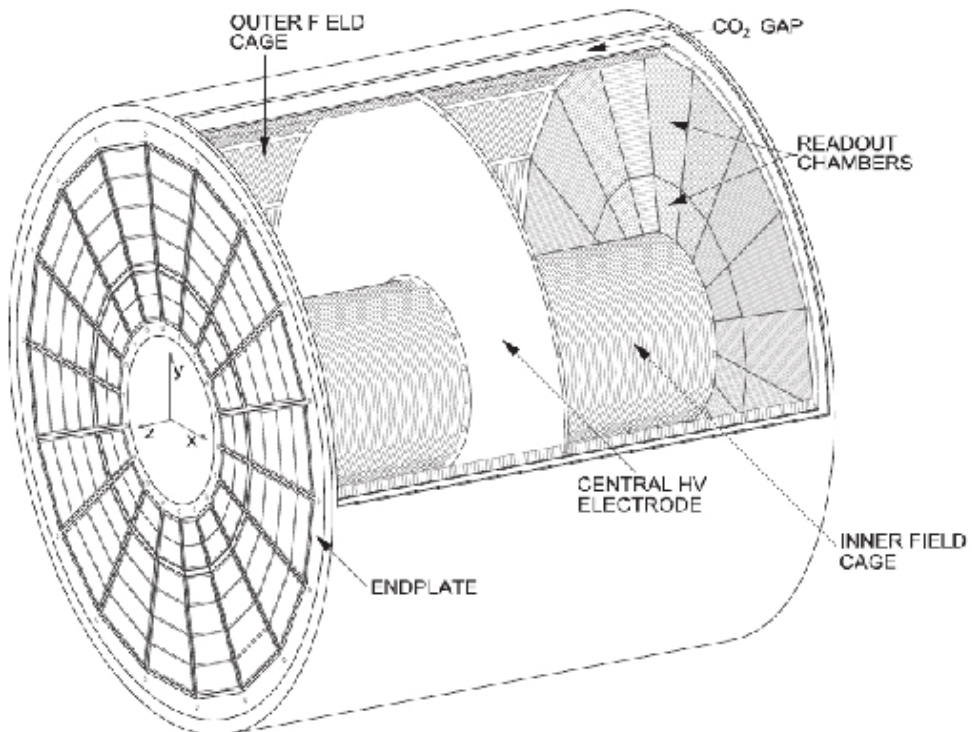


Figure 28: Schematic view of ALICE Time Projection Chamber

1184 During long shutdown 2 in 2019-2020 ALICE will go through significant modi-  
1185 fications. The goal is to be able have continuous readout [?] in heavy ion collisions  
1186 at an interaction rate of 50 kHz. I have made a personal contribution to the quality  
1187 assurance of the new GEM readout of TPC.

1188 ALICE will add a new Forward Interaction trigger (FIT) to replace the V0 and  
1189 T0 detectors.

1190     Additionally the current inner tracking system (ITS) will be completely re-  
1191 placed. The current layered structure with three different technologies will be  
1192 replaced by an all pixel detector with significantly reduced pixel size. Additionally  
1193 the first layer will be brought closer to the beam pipe. The new ITS will have  
1194 better tracking efficiency and better impact parameter resolution.

1195     The muon detection will be complimented by the Muon Forward Tracker (MFT) [?].  
1196 Based on the same technology as the new ITS, MFT will be placed before the  
1197 hadron absorber that sits in front of the existing muon spectrometer. MFT should  
1198 significantly increase the signal/background ratio in heavy quark measurements.

1199     Many subdetectors will make small improvements to enhance the readout rate.  
1200 The central trigger processor will be replaced and ALICE will introduce a new  
1201 framework  $O^2$  that combines both online data acquisition and offline analysis.

1202     The detector restricting the readout the most at the moment is the TPC. The  
1203 current wire chamber based system limits the readout rate to 3.5 kHz. To achieve  
1204 the 50 kHz readout rate goal the wire chambers will be replaced by a Gas Electron  
1205 Multiplier (GEM) based system.

1206     TPC has a total of 36 inner and 36 outer readout chambers. Each of these will  
1207 consist of 4 layers of GEM foils. The inner chambers will only have one foil for  
1208 each layer. The outer chambers are separated into three sections, each with its  
1209 own layer of foils. Each gem foil is made up of a 50  $\mu\text{m}$  thick resistive capton layer,  
1210 coated on both sides by 5  $\mu\text{m}$  thick layers of copper. Each foils is separated into a  
1211 number (20-24) of distinct active areas. The active areas are pierced quite densely,  
1212 they have 50-100 holes in the area of a single  $\text{mm}^2$ . The density of holes changes  
1213 from layer to layer. The two middle layers of foils have a larger (double) pitch  
1214 (smaller hole density) while the top and bottom layers have a smaller (normal)  
1215 pitch (larger hole density).

1216     The holes have a conical shape which they acquire during a two step chemical  
1217 etching process.

1218     The working principle of these foils is based on electrodynamics. **elaborate** There  
1219 is a large potential difference (140-400 V) applied to the two sides of the foil, which  
1220 results in large field in each hole. This acts both as a lens and an amplifier for  
1221 the electrons. The amplification happens inside the holes where the field is the  
1222 strongest.

1223     As opposed to wire chambers, which typically have one voltage setting, a GEM-  
1224 based detector requires several independent voltage settings: there is a drift voltage  
1225 which drives the electrons from the ionisation point to the GEM, an amplification  
1226 voltage, and an extraction voltage that brings electrons from the GEM exit to the  
1227 readout plane.

1228     The GEMs are designed to minimise ion backflow to allow continuous, ungated  
1229 and untriggered readout.

1230 The purpose of the multilayered structure is to reduce the ion backflow []; not  
1231 only one layer of GEM foils will be installed, but a 4 layer stack. In the stack there  
1232 are 2 standard pitch GEM foils, where the pitch size, i.e. the separation of the  
1233 holes inside a foil is around  $140 \mu\text{m}$ , and 2 large pitch GEM foils, there the hole  
1234 spacing is two times larger,  $280 \mu\text{m}$ . The two outer layers will have standard pitch  
1235 and the two middle layers have large pitch. The middle layers with large pitch  
1236 serve as extra insulator against the ion backflow. Additionally the setup allows  
1237 operating individual GEM foils at lower voltages and still have an increase in the  
1238 gain of a few orders of magnitude.

1239 [107]

#### 1240 Quality Assurance of the GEM foils

1241 The GEM foils are produced at CERN, where they will undergo a basic QA (QA-B)  
1242 procedure, that includes

- 1243 • Coarse optical inspection to see any major defects, holes, cuts and dis-  
1244 coloured regions
- 1245 • Short-term leakage current measurement

1246 Any problems found in the basic inspection are documented for later cross-  
1247 checking.

1248 The advanced quality assurance (QA-A) is performed in two centers, one in  
1249 the Helsinki Institute of Physics (HIP) and one in the Wigner Research Centre in  
1250 Budapest. The QA-A procedure includes the following measurements

- 1251 • Long-term leakage current measurement
- 1252 • High-resolution optical scanning
- 1253 • Gain uniformity check (In Budapest)

1254 In the procedure foils are classified according to a traffic light system. Red  
1255 means the foil didn't pass the basic selection criteria and thus cannot be used.  
1256 Yellow means it might be usable and green means that the foil passed all evalua-  
1257 tions.

##### 1258 2.3.4 Optical scanning

1259 The etching process is a delicate one; many things can go wrong, that are not visible  
1260 by eye in the coarse optical inspection. It is expected that the hole parameters are  
1261 connected with the foil's electric properties [], so a precise optical measurement

Figure 29: An example image taken of a GEM foil with false colors.

can help in classifying the foils. For example, smaller holes create more intense and focused fields, which would result in larger amplification of their avalanche electrons, i.e. the local gain would be larger.

The foils are scanned with the help of a scanning robot. The setup along with most of the software was developed at the Detector Laboratory of the University of Helsinki []

Each image is a false colour superposition of two images, one with foreground illumination and one with background illumination. In this way one can observe the three relevant diameters of the foil, the top, middle and bottom diameters. The background light highlights the middle holes, while the foreground illumination captures either the top or the bottom depending on the orientation of the foil as the foils are scanned from both sides. Fig. 29

The setup takes images with area about  $11.3\text{ mm} \times 8.5\text{ mm}$ , corresponding to 2560 by 1920 pixels, resulting in a total of 2000-3500 individual images for both sides of a GEM foil, depending on its type. The images are fed into neural network classifier, which identifies the holes, finds defects and extracts the hole parameters by fitting ellipses to the recognised contours. Thus every individual hole can be measured, which otherwise would be completely unfeasible as even the smallest of foils has about 10 million holes.

### Long term HV measurement of the GEM foils

After the optical scanning, the foils are subjected to a long term ( 5-12 hours) high voltage leakage current measurement. Each segment of the GEM foil is connected to a high voltage and the leakage current is measured separately for each segment, by the connected picoamper-meter (pA-meter) []. The accepted leakage current in each segment is 0.16 nA, foils with larger values are discarded.

### Gain scan

A small subset of the foils were put through a gain scan. The gain scan could only be performed in the QA-A centre of Budapest. As the time required to scan 1 foil was several days, the gain scan couldn't be performed even for all foils in Budapest.

The gain scan uses charged particles provided by a  $^{55}\text{Fe}$  source, which was placed above the foil. It emits X-ray photons with an energy of 5.9 keV. The photons will convert to electrons in the gain scanner's Ar + CO<sub>2</sub> gas mixture,

either via photoelectric effect or via Compton Scattering. There electrons travel a few microns in the gas, ionising the gas along their path.

Below the GEM frame, there is a multiwire proportional pad, with perpendicular wires with a resolution of 4 mm in  $x$  and 3 mm in  $y$ . Amplification is measured both with (HV) and without (reference) voltage over the GEM foil. The HV measurement is divided with the reference measurement, which results in the gain map of the GEM.

## Gain correlations

### 2.3.5 Particle identification

One guiding principle in the design of ALICE was to achieve good particle identification (PID) over a large part of phases space and for several different particle types. In ALICE there are several detectors taking part in the identification of particles.

One of the particle identification detectors is the transition radiation detector (TRD) [?]. Its main task is identifying electors with momenta larger than 1 GeV. Transition radiation is produced when highly relativistic particles traverse the boundary between two media having different dielectric constants. The average energy of the emitted photon is approximately proportional to the Lorentz factor  $\gamma$  of the particle, which provides an excellent way of discriminating between electrons and pion. ALICE TRD is made of a composite layer of foam and fibres. The emitted photons are then measured in six layers of Xe/CO<sub>2</sub> filled time expansion wire chambers.

The time of flight (TOF) detector uses a very simple physics principle, i.e. calculating the velocity of the particle using the time of flight between two points. Combining this with the momentum of particle, obtained from the tracking detectors, one can calculate the mass of the particle, which identifies particles. The TOF detector consists of multigap resistive wire chambers. These are stacks of resistive plates spaced equally. They allow time of flight measurements in large acceptance with high efficiency and with a resolution better than 100 ps.

The third specific particle identification detector is the high momentum particle identification (HMPID) detector. The HMPID uses a ring imaging Cherenkov counter to identify particles with momenta larger than 1 GeV. Particles moving through a material faster than the speed of light in the material will produce Cherenkov radiation. The velocity of the particle determines the angle at which the radiation is emitted. Measuring this angle gives the velocity of the particle. This can be again used to calculate the mass of the particle, if the momentum is known. In HMPID the material is a liquid radiator and the photons are measured with multiwire proportional chambers in conjunction with photocathodes.

1333 In addition to the specific particle identification detectors, the general purpose  
1334 tracking detectors can be used for identification through the use of specific energy  
1335 loss of charged particles traversing through a medium and the transition radiation  
1336 emitted by charged particles when crossing the boundary between two materials.

1337  $dE/dx$  measurements are provided by the last four layers of the ITS detector, i.e.  
1338 the SDD and the SSD, thanks to their analog readout. [108] ITS provides particle  
1339 identification in the low  $p_T$  region, up to 1GeV, and pions reconstructed in the  
1340 standalone mode can be identified down to 100 MeV. Similar to ITS the TPC  
1341 detector provides specific energy loss measurements. TPC can identify charged  
1342 hadrons up to  $p_T$  1 – 2GeV as well as light nuclei, He3 and He4.

### 1343 2.3.6 Electromagnetic Calorimeter

1344 Calorimeters are designed to measure the energy of particles. Electromagnetic  
1345 calorimeters specialise in detecting particles that interact primarily through the  
1346 electromagnetic interaction, namely photons and electrons. They are required in  
1347 many neutral meson and direct photon analyses. In addition the energy informa-  
1348 tion enhance jet measurements.

1349 ALICE has two electromagnetic calorimeters, the photon spectrometer (PHOS) [109]  
1350 and the electromagnetic calorimeter (EMCal) [?]. PHOS is a homogeneous calorime-  
1351 ter that consists of scintillating PbWO<sub>4</sub> crystals, which generate a bremsstrahlung  
1352 shower and produce scintillation light. The energy of the particle determines the  
1353 amount of light produced. To improve the charged particle rejection, PHOS in-  
1354 cludes a charged particle veto detector (CPV) [?]. PHOS is built to have a very  
1355 fine granularity, making it well suited for measuring direct photons and neutral  
1356 mesons.

1357 EMCal is a sampling calorimeter. It consists of layers of lead and scintilla-  
1358 tor tiles. The lead tiles produce the shower and scintillator tiles the light. The  
1359 signal is then read with wavelength shifting fibres. The acceptance of EMCal in  
1360 the azimuthal angle is  $80 \text{ deg} < \phi < 187 \text{ deg}$ . During long shutdown 1 in 2013-  
1361 2015, EMCal was extended with the di-jet calorimeter (DCal) [110], giving an  
1362 additional acceptance region of  $260 \text{ deg} < \phi < 320 \text{ deg}$ . This provides partial  
1363 back-to-back coverage. In comparison to PHOS, EMCal has coarser granularity,  
1364 but a significantly larger acceptance, making it suitable for jet physics.

### 1365 2.3.7 Forward detectors

1366 ALICE includes a few small and specialised detectors of importance. The event  
1367 time is determined with very good precision ( $< 25 \text{ ns}$ ) by the T0 detector [?]. T0  
1368 consists of two sets of Cherenkov counters that are mounted around the beam pipe  
1369 on both sides of the interaction point. T0 gives the luminosity measurement in

1370 ALICE.

1371 Another small detector in the forward direction is the V0 detector [?]. This  
1372 consists of two arrays of segmented scintillator counters located at  $-3.7 < \eta <$   
1373  $-1.7$  and  $2.8 < \eta < 5.1$ . V0 is used as a minimum bias trigger and for rejection  
1374 of beam-gas background. Particle multiplicity in the forward direction can be  
1375 related to the event centrality. Thus V0 is the main detector used in centrality  
1376 determination in PbPb collisions.

1377 The multiplicity measurement of V0 is complimented by the forward multi-  
1378 plicity detector (FMD) [?]. FMD includes five rings of silicon strip detectors that  
1379 make up the FMD. FMD gives acceptance in the range  $-3.4 < \eta < -1.7$  and  
1380  $1.7 < \eta < 5.0$ .

1381 During long shutdown 2 in 2019-2020, V0 and T0 will be replaced by the Fast  
1382 Interaction Trigger (FIT) detector [?]. For historical reasons elements of FIT are  
1383 also referred to as V0+ and T0+. FIT will allow centrality, event plane, luminosity  
1384 and interaction time determination in the continuous readout mode, that ALICE  
1385 will operate in after 2020.

1386 For photon multiplicity measurement ALICE has the photon multiplicity de-  
1387 tector (PMD) [?]. PMD uses two planes of gas proportional counters with a  
1388 cellular honeycomb structure. PMD gives the multiplicity and spatial distribution  
1389 of photons in the region  $2.3 < \eta < 3.7$ .

1390 On top of the ALICE magnet there is an array of 60 large scintillators called  
1391 the ALICE cosmic ray detector (ACORDE) [?]. ACORDE is used as a trigger  
1392 for cosmic rays for calibration and alignment.

1393 The only hadronic calorimeters in ALICE are the zero degree calorimeters  
1394 (ZDC) [?], which are located next to the beam pipe in the machine tunnel about  
1395 116 m from the interaction point. There are two sets of calorimeters. One is  
1396 made of tungsten, specialising in measuring neutrons, while the other, made of  
1397 brass, is specialised in measuring protons. In heavy ion and especially in proton-  
1398 lead collisions, ZDC gives information about the centrality of the event. ZDC is  
1399 meant to detect spectators, i.e. parts of the colliding ions that do not take part  
1400 in the interaction. If there are more spectators, the collisions is likely to be more  
1401 peripheral.

1402 A new detector installed during the long shutdown 1 is the ALICE diffractive  
1403 detector (AD) [?]. AD consists of two assemblies, one in each side of the interaction  
1404 point, both made of two layers of scintillators. These assemblies are situated about  
1405 17 m and 19.5 m away from the interaction points. The pseudorapidity coverage is  
1406  $-6.96 < \eta < -4.92$  and  $4.78 < \eta < 6.31$ . AD greatly enhances ALICE's capability  
1407 for diffractive physics measurements that require a large pseudorapidity gap.

1408 **2.3.8 Muon spectrometer**

1409 Outside the main magnet, ALICE has a spectrometer dedicated to measuring  
1410 muons [?]. In heavy ion physics muons are mainly used to measure the production  
1411 of the heavy quark resonances  $J/\psi$ ,  $\Psi'$ ,  $\Upsilon$ ,  $\Upsilon'$  and  $\Upsilon''$ .

1412 The muon spectrometer consists of three parts, the absorber, the muon tracker  
1413 and the muon trigger. The absorber is meant to remove the hadronic background  
1414 as efficiently as possible. After the absorber there are ten plates of thin cathode  
1415 strip tracking stations with high granularity, the muon tracker. After the muon  
1416 tracker there is a layer of iron to filter out any remaining particles, other than  
1417 muons. The muon trigger is located behind this layer. The trigger consists of four  
1418 resistive plate chambers.

1419 **2.3.9 Trigger**

1420 **EMCAL trigger**

### **3 Event and track selection**

The  $\sqrt{s_{\text{NN}}} = 5.02$  TeV p–Pb ( $1.3 \cdot 10^8$  events,  $\mathcal{L}_{\text{int}} = 620 \text{ nb}^{-1}$ ) collisions were recorded in 2013 by the ALICE detector [111]. The details of the performance of the ALICE detector during LHC Run 1 (2009–2013) are presented in Ref. [112].

The analysis uses charged tracks that are reconstructed with the Inner Tracking System (ITS) [113] and the Time Projection Chamber (TPC) [114]. These detectors are located inside the large solenoidal magnet, that provides a homogeneous magnetic field of 0.5 T. Tracks within a pseudorapidity range  $|\eta| < 0.9$  over the full azimuth can be reconstructed. The ITS is made up of the innermost Silicon Pixel Detector (SPD), the Silicon Drift Detector (SDD) and the outermost Silicon Strip Detector (SSD). Each of these consists of two layers. The TPC is a cylinder filled with gas. Gas is ionised along the path of charged particles. Liberated electrons drift towards the end plates of the cylinder where they are detected. Combining the information from the ITS and the TPC provides a resolution ranging from 1 to 10 % for charged particles with momenta from 0.15 to 100 GeV/c. For tracks without the ITS information, the momentum resolution is comparable to that of ITS+TPC tracks below transverse momentum  $p_T = 10 \text{ GeV}/c$ , but for higher momenta the resolution reaches 20 % at  $p_T = 50 \text{ GeV}/c$  [112, 115].

Neutral particles used in jet reconstruction are reconstructed by the Electromagnetic Calorimeter (EMCAL) [116]. The EMCAL covers an area with a range of  $|\eta| < 0.7$  in pseudorapidity and 100 deg in azimuth. EMCAL is complimented with the Dijet Calorimeter (DCal) [110] and Photon Spectrometer (PHOS) [109] that are situated opposite of the EMCAL in azimuth. PHOS covers 70 degrees in azimuth and  $|\eta| < 0.12$ . The DCal is technologically identical to EMCal. The DCal coverage spans over 67 degrees in azimuth, but in pseudorapidity the mid region is occupied by the PHOS. In between PHOS and DCal active volumes, there is a gap of 10 cm. DCal is fully back-to-back with EMCal.

The combination of charged tracks with  $p_T > 0.15 \text{ GeV}/c$  and neutral particles with  $p_T > 0.30 \text{ GeV}/c$  is used to construct jets.

The V0 detector [117] provides the information for event triggering. The V0 detector consists of two scintillator hodoscopes that are located on either side of the interaction point along the beam direction. It covers the pseudorapidity region  $-3.7 < \eta < -1.7$  (V0C) and  $2.8 < \eta < 5.1$  (V0A). For the 2013 p–Pb collisions events are required to have signals in both V0A and V0C. This condition is used later offline to reduce the contamination of the data sample from beam-gas events by using the timing difference of the signal between the two stations [112].

EMCAL is also used to provide the jet trigger used in triggered datasets. EMCAL can be used to trigger on single shower deposits or energy deposits integrated over a larger area. Latter case is used for jet triggers. The EMCAL trigger definition in the 2013 p–Pb collisions requires an energy deposit of either 10 GeV for the

1461 low threshold trigger or 20 GeV for the high threshold trigger in a  $32 \times 32$  patch  
1462 size.

1463 In p–Pb collisions the tracks are selected following the hybrid approach [118]  
1464 which ensures a uniform distribution of tracks as a function of azimuthal angle  
1465 ( $\varphi$ ). The momentum resolutions of the two classes of particles are comparable up  
1466 to  $p_T \approx 10$  GeV/ $c$ , but after that, tracks without ITS requirements have a worse  
1467 resolution [112, 115].

### 1468 3.1 statistics

1469 Number of jets in different datasets and with different jet finders is shown in table  
1470 2. Background statistics for number of background cones (number of jets minus  
1471 number of discarded cones) are shown in table 3. Ratio of background cones to  
1472 number of jets is shown in table 4. The likelihood of having to discard a jet from  
background calculation is about 1-2%.

Table 2: Number of found jets by dataset and jet  $p_T$  bin

Jet $p_T$	5-10	10-20	20-30	30-40	40-60	60-80	80-100	100-150	150-500
MBFullR04	4969393	621753	32552	5584	1974	310	90	37	5
MBFullR05	4750567	826598	42373	5543	1719	276	73	29	3
MBChargedR04	3144538	673419	37783	4121	1009	148	36	12	1
MBChargedR05	2229247	175763	7961	1270	410	61	12	3	
TriggeredFullR04	187557	115927	78138	51317	39262	8621	2409	1167	171
TriggeredFullR05	99991	77147	48612	34325	28104	6342	1726	794	104
TriggeredChargedR04	37411	29945	18186	13148	11142	2517	675	326	44
TriggeredChargedR05	433155	175031	54789	19776	10626	1983	457	194	15

1473

Table 3: Number of background cones used in perpendicular cone background calculation

Jet $p_T$	5-10	10-20	20-30	30-40	40-60	60-80	80-100	100-150	150-500
MBFullR04	4947583	617895	32357	5548	1965	310	90	37	5
MBFullR05	4710217	815461	41584	5439	1698	273	73	29	3
MBChargedR04	3117495	661106	36739	4014	988	144	36	12	1
MBChargedR05	2195286	172919	7860	1249	406	61	12	3	
TriggeredFullR04	186574	115376	77949	51216	39196	8603	2405	1167	171
TriggeredFullR05	99102	76462	48320	34216	28038	6334	1722	794	103
TriggeredChargedR04	37160	29543	17988	13099	11129	2515	675	326	44
TriggeredChargedR05	313421	140707	45229	16243	8709	1604	377	154	14

Table 4: Ratio of background cone number to number of jets

MBFullR04	99.56%	99.38%	99.40%	99.36%	99.54%	100.00%	100.00%	100.00%	100.00%
MBFullR05	99.15%	98.65%	98.14%	98.12%	98.78%	98.91%	100.00%	100.00%	100.00%
MBChargedR04	99.14%	98.17%	97.24%	97.40%	97.92%	97.30%	100.00%	100.00%	100.00%
MBChargedR05	98.48%	98.38%	98.73%	98.35%	99.02%	100.00%	100.00%	100.00%	100.00%
TriggeredFullR04	99.48%	99.52%	99.76%	99.80%	99.83%	99.79%	99.83%	100.00%	100.00%
TriggeredFullR05	99.11%	99.11%	99.40%	99.68%	99.77%	99.87%	99.77%	100.00%	99.04%
TriggeredChargedR04	99.33%	98.66%	98.91%	99.63%	99.88%	99.92%	100.00%	100.00%	100.00%
TriggeredChargedR05	72.36%	80.39%	82.55%	82.13%	81.96%	80.89%	82.49%	79.38%	93.33%

## 1474 4 Analysis method

### 1475 4.1 Jet Finding

1476 The analysis uses reconstructed jets as estimates of the original parton. Essentially  
1477 when reconstructing jets, nearby tracks are combined into jets. Collisions between  
1478 hadrons are never as clean as electron-electron collisions. Even for a proton-proton  
1479 collision there are participant partons, that will produce a soft background in ad-  
1480 dition to the hard scattering products. Jet reconstruction must deal with this soft  
1481 background. The reconstruction is never perfect, one can have uncorrelated tracks  
1482 that get included in the jet and some tracks originating from the parton are missed  
1483 by the reconstruction. There are several methods to perform the reconstruction,  
1484 all of which require some kind of size parameter, which cuts out jet participants  
1485 too far from the jet axis. The tracks that are grouped into a jet are referred to as  
1486 jet constituents.

1487 The analysis is performed by analysing jet constituents. In each collision event,  
1488 the jets are reconstructed using FastJet [119] with the anti- $k_T$  algorithm [120].  
1489 Jets for  $R=0.4$  are selected in  $|\eta| < 0.25$  to satisfy the fiducial acceptance of the  
1490 EMCal. In jet reconstruction both charged tracks with  $p_T > 0.15 \text{ GeV}/c$  and  
1491 neutral clusters with  $p_T > 0.30 \text{ GeV}/c$  are considered. In the analysis, results are  
1492 presented in terms of the jet transverse momentum  $p_{T\text{jet}}$ .

#### 1493 4.1.1 Anti $k_T$ algorithm

1494 Jets are reconstructed using the anti- $k_T$  algorithm [120]. The algorithm works by  
1495 trying to undo the splittings through combining protojets. The algorithm creates  
1496 a list of protojets. At the beginning the list is populated by converting each track  
1497 in the event into a protojet. Then the algorithm proceeds by combining these  
1498 protojets.

1499 The algorithm calculates distance measures for each individual protojet and  
1500 for each possible pair of protojets. For individual protojets this depends only on  
1501 the transverse momentum of the track.

$$k_{T,i}^2 = p_{T,i}^{2p}$$

1502 For each pair of protojets the distance measure is calculated as

$$k_{T,(i,j)}^2 = \min(p_{T,i}^{2p}, p_{T,j}^{2p}) \frac{\Delta R_{i,j}^2}{D^2},$$

1503 where

$$R_{i,j} = (\phi_i - \phi_j)^2 + (y_i - y_j)^2$$

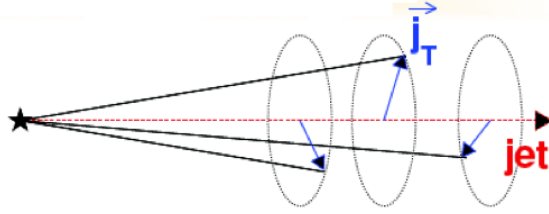


Figure 30: Illustration of  $\vec{j}_T$ . The jet fragmentation transverse momentum,  $\vec{j}_T$ , is defined as the transverse momentum component of the track momentum,  $\vec{p}_{\text{track}}$ , with respect to the jet momentum,  $\vec{p}_{\text{jet}}$ .

If  $k_{T,i}$  is the smallest quantity then the protojet is a jet and it is removed from further consideration. If  $k_{T,(i,j)}$  is the smallest quantity the two protojets are merged. This is iterated until no protojets are left.

The choice of the power  $p$  in the distance measure depends on the algorithm used

- $p = 1$ :  $k_T$  algorithm
- $p = 0$ : Cambridge Aachen algorithm
- $p = -1$ : anti- $k_T$  algorithm

With the choice  $p = -1$  in anti- $k_T$  algorithm, the softest splittings are undone first. One consequence of the power choice in the anti- $k_T$  algorithm is that reconstructed jets have a shape close to circular.

## 4.2 $j_T$

The jet fragmentation transverse momentum,  $j_T$ , is defined as the component of the constituent particle momentum,  $\vec{p}_a$ , transverse to the jet momentum,  $\vec{p}_{\text{jet}}$ . The resulting  $\vec{j}_T$  is illustrated in Fig. 30. The length of the  $\vec{j}_T$  vector is

$$j_T = \frac{|\vec{p}_{\text{jet}} \times \vec{p}_{\text{track}}|}{|\vec{p}_{\text{jet}}|}. \quad (35)$$

It is commonly interpreted as a transverse kick with respect to the initial hard parton momentum that is given to a fragmenting particle during the fragmentation process, which is a measure of the momentum spread of the jet fragments [].

The reconstructed jet axis is used for  $j_T$  reference. Any charged track within a fixed cone with radius  $R$  is taken as a jet constituent, as opposed to using the

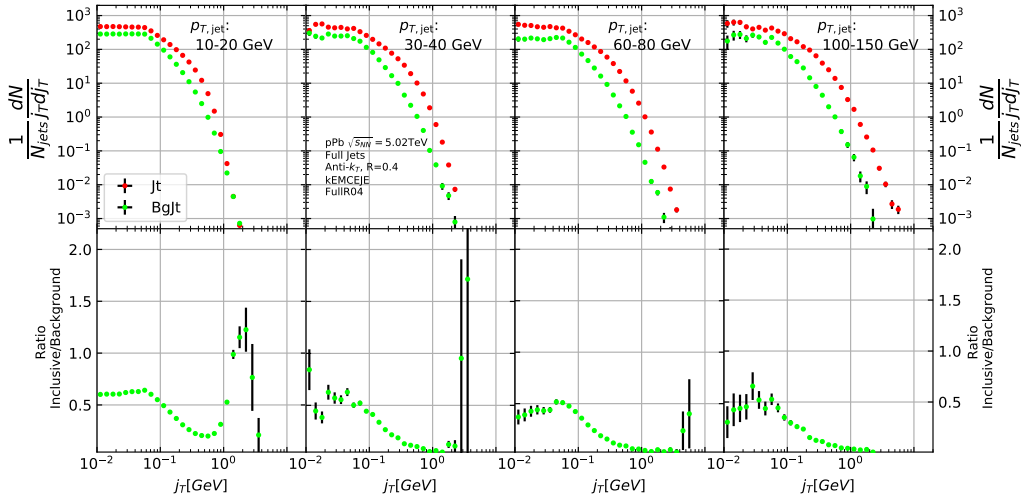


Figure 31: Inclusive  $j_T$  with background

constituent list provided by the jet algorithm. Anti- $k_T$  produces jets that are very circular in shape. Thus this doesn't change the constituent list considerably. Neutral tracks are used only in jet reconstruction.

$j_T$  results are shown as

$$\frac{1}{j_T} \frac{dN}{dj_T} \quad (36)$$

distributions. The logic behind this is that  $j_T$  is inherently a two-dimensional observable, comprised of  $j_{Tx}$  and  $j_{Ty}$  components. So the actual physical observable would be

$$\frac{d^2N}{dj_{Tx} dj_{Ty}} \quad (37)$$

Changing into polar coordinates with  $j_{Tr} = j_T$  and  $\theta$  gives

$$\frac{d^2N}{j_T dj_T d\theta}, \quad (38)$$

where  $j_T$  over the azimuth  $\theta$  should stay constant and it can be integrated over, which gives

$$\frac{1}{2\pi} \frac{dN}{j_T dj_T}. \quad (39)$$

Results of the raw inclusive  $j_T$  distribution in four  $p_{T,jet}$  bins with background are shown in figure 31. Background is further discussed in Sec. 4.4

1536 **4.3 Unfolding**

1537 **Extend unfolding**

1538 The raw inclusive  $j_T$  distributions are corrected for the detector inefficiency  
1539 using the unfolding method. The response matrix for the unfolding is obtained  
1540 from a PYTHIA [121] simulation.

Measured distributions are affected by two main factors; Limited acceptance -  
The probability to observe a given event is less than one and limited resolution -  
Quantity  $x$  cannot be determined exactly, but there is a measurement error. True  
 $f(x)$  and measured  $g(y)$  distributions are connected by a convolution integral.  
Including statistical fluctuations this becomes

$$\hat{g}(y) = \int_a^b A(y, x) f(x) dx + \epsilon(y),$$

where  $A$  is the detector response obtained by (for example) Monte Carlo simulations and  $\epsilon(y)$  is the term coming from statistical fluctuations. If  $x$  and  $y$  are discrete variables we have

$$\hat{g}_i = \sum_{j=1}^m A_{ij} f_j + \epsilon_i,$$

Or in matrix form

$$\hat{g} = Af + \epsilon$$

If the only detector effect is limited acceptance,  $A$  is a diagonal matrix. In a general discrete case the (naive) solution is obtained by the inverse matrix

$$\hat{f} = A^{-1}\hat{g}$$

1541 However this usually leads to oscillating solutions and determining the inverse  
1542 matrix can be difficult.

1543 Two common methods to perform this inversion are Bayesian and SVD unfolding  
1544 methods. Often the solution requires some additional *a priori* information.  
1545 For example the solution should be smooth in most cases.

1546 **4.3.1 Bayesian unfolding**

The bayesian (iterative) method is based on the Bayes formula [].

$$P(C_i|E_j) = \frac{P(E_j|C_i) P_0(C_i)}{\sum_{l=1}^{n_C} P(E_j|C_l) P_0(C_l)},$$

1547 i.e. the probability of Cause ("truth")  $C_i$  given Effect ("observed")  $E_j$  is proportional  
1548 to the probability of observing  $E_j$  given  $C_i$  (response matrix) and the  
1549 truth distribution  $P_0(C_i)$ .

At first  $P_0$  is given some starting distribution, either a uniform distribution or some guess of the final distribution. Taking into account the inefficiency this gives

$$\hat{n}(C_i) = \frac{1}{\epsilon_i} \sum_{j=1}^{n_E} n(E_j) P(C_i|E_j),$$

where

$$P(C_i|E_j) = \frac{P(E_j|C_i) P_0(C_i)}{\sum_{l=1}^{n_C} P(E_j|C_l) P_0(C_l)},$$

and

$$\hat{n}(C_i) = \frac{1}{\epsilon_i} \sum_{j=1}^{n_E} n(E_j) P(C_i|E_j). \quad (40)$$

First  $P(C_i|E_j)$  is calculated with the uniform distribution or best guess of the shape of the distribution. This is then used to calculate the new distribution  $\hat{P}(C_i)$

$$\hat{N}_{true} = \sum_{i=1}^{n_C} \hat{n}(C_i), \quad \hat{P}(C_i) = P(C_i|n(E)) = \frac{\hat{n}(C_i)}{\hat{N}_{true}}$$

$P_0$  is then replaced with  $\hat{P}$  and the procedure is repeated until an acceptable solution is found.

The bayesian procedure alongside with the SVD unfolding method are implemented in the RooUnfold package [122], which is used to perform the unfolding in practice. In RooUnfold the number of iterations is given beforehand. In practice this requires some trial and error. The number of iterations should be as low as possible, as the errors increase when going further in the iterations, but the number of iterations must be high enough so that the correct distribution is extracted.

### Error propagation in the Bayesian procedure

The measured distribution has some statistical uncertainty, this should be reflected in the unfolded distribution. Additionally the response matrix may have some uncertainty if the statistics used in the Monte Carlo simulation were limited.

For errors originating from the measured distribution RooUnfold uses the error propagation matrix

$$\frac{\partial \hat{n}(C_i)}{\partial n(E_j)} = M_{ij} + \frac{\hat{n}(C_i)}{n_0(C_i)} \frac{\partial n_0(C_i)}{\partial n(E_j)} - \sum_{k=1}^{n_E} \sum_{l=1}^{n_C} \frac{n(E_k) \epsilon_l}{n_0(C_l)} M_{ik} M_{lk} \frac{\partial n_0(C_l)}{\partial n(E_j)}, \quad (41)$$

where  $\hat{n}(C_i)$  is the unfolded result from Eq. 40. This depends upon the matrix  $\frac{\partial n_0(C_i)}{\partial n(E_j)}$ , which is  $\frac{\partial \hat{n}(C_i)}{\partial n(E_j)}$  from the previous iteration. In the first iteration,  $\frac{\partial n_0(C_i)}{\partial n(E_j)} = 0$  and  $\frac{\partial \hat{n}(C_i)}{\partial n(E_j)} = M_{ij}$ .

1568      The error propagation matrix  $V$  is used to obtain the covariance matrix on the  
1569 unfolded distribution

$$V(\hat{n}(C_k), \hat{n}(C_l)) = \sum_{i,j=1}^{n_E} \frac{\partial \hat{n}(C_k)}{\partial n(E_i)} V(\hat{n}(E_i), \hat{n}(E_j)) \frac{\partial \hat{n}(C_l)}{\partial n(E_j)}, \quad (42)$$

1570      where  $V(\hat{n}(E_i), \hat{n}(E_j))$  is the covariance matrix of the measurements. In  
1571 counting experiments common in particle physics, each bin is independently Pois-  
1572 son distributed, with

$$V(\hat{n}(E_i), \hat{n}(E_j)) = n(E_i) \delta_{ij} \quad (43)$$

1573      The error propagation matrix for the response matrix is

$$\begin{aligned} \frac{\partial \hat{n}(C_i)}{\partial P(E_j|C_k)} &= \frac{1}{\epsilon_i} \left( \frac{n_0(C_i) n(E_j)}{f_j} - \hat{n}(C_i) \right) \delta_{ik} - \frac{n_0(C_k) n(E_j)}{f_j} M_{ij} + \\ &\frac{\hat{n}(C_i)}{n_0(C_i)} \frac{\partial n_0(C_i)}{\partial P(E_j|C_k)} - \frac{\epsilon_i}{n_0(C_i)} \sum_{l=1}^{n_E} \sum_{r=1}^{n_C} n(E_l) M_{il} M_{rl} \frac{\partial n_0(C_r)}{\partial P(E_j|C_k)}, \end{aligned} \quad (44)$$

1574      where  $\frac{\partial n_0(C_i)}{\partial P(E_j|C_k)}$  is the error propagation matrix from the previous iteration,  
1575  $\frac{\hat{n}(C_i)}{\partial P(E_j|C_k)}$ . From the first iteration, this is zero and the final two terms in Eq. 44  
1576 disappear.

1577      The covariance matrix due to these errors is given by

$$V(\hat{n}(C_k), \hat{n}(C_l)) = \sum_{j,s=1}^{n_E} \sum_{i,r=1}^{n_C} \frac{\partial \hat{n}(C_k)}{\partial P(E_j|C_i)} V(P(E_j|C_i), P(E_s|C_r)) \frac{\partial \hat{n}(C_l)}{\partial P(E_s|C_r)}, \quad (45)$$

1578      where  $V(P(E_j|C_i), P(E_s|C_r))$  can be taken as multinomial, Poisson or other  
1579 distribution.

### 1580 4.3.2 Toy Monte Carlo

remove? A toy Monte Carlo simulation was performed to see the performance in an ideal case. Sample jet  $p_T$  values from observed  $p_T$  distribution. Starting from this  $p_T$  start creating tracks with

$$p_{\text{track}} = z_{\text{track}} p_{T,\text{jet}}$$

1581 where  $z_{\text{track}}$  is sampled from the observed  $z$  distribution. All tracks below 0.15GeV  
1582 are discarded. Sampling is continued until the sum of the track transverse momenta

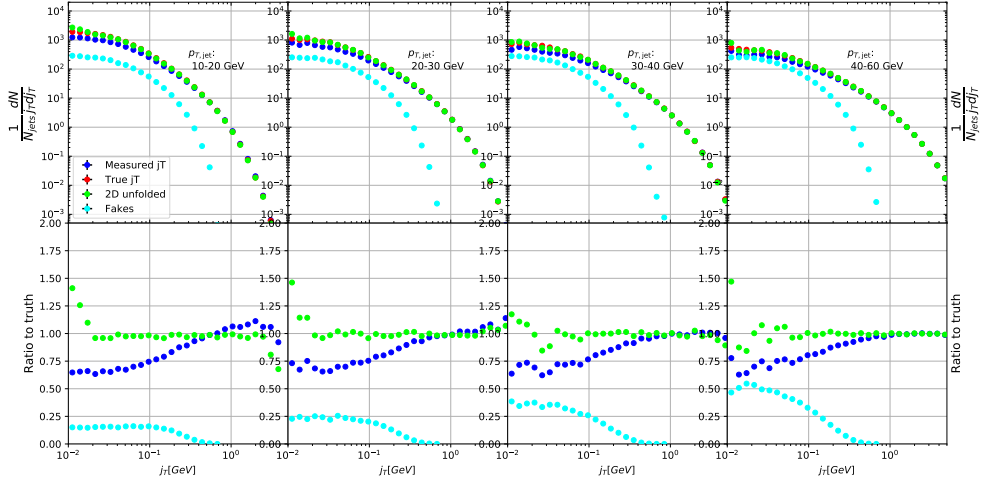


Figure 32: Results from unfolding in Toy Monte Carlo

1583 exceeds the jet transverse momentum. Jet is then defined as the sum of the track  
 1584 momenta.

1585 Simultaneously a  $p_T$  dependant observation efficiency is applied to the tracks  
 1586 and a separate observed jet is calculated using only the observed tracks. Addi-  
 1587 tionally a set of fake tracks is added to the observed jet. Tracks are always either  
 1588 observed or not at the true momentum. No smearing is added to the observed  
 1589 momentum.

Afterwards the tracks are looped over for  $j_T$  calculation. For observed tracks we calculate  $j_T$  with respect to both the true jet axis and the observed jet. 2D Response matrix is filled with

$$(j_{T,\text{obs}}, p_{T,\text{jet},\text{obs}}, j_{T,\text{true}}, p_{T,\text{jet},\text{true}})$$

1590 In practice this is done with a set of 3D histograms, where  $p_{T,\text{jet},\text{true}}$  determines  
 1591 the histogram index and the remaining three values the bin in the 3D histogram.

1592 After creating the response matrices, an identical procedure is carried out the  
 1593 create testing data. Now instead of filling response matrices, 2D histograms are  
 1594 filled with  $(j_{T,\text{obs}}, p_{T,\text{jet},\text{obs}})$  and  $(j_{T,\text{true}}, p_{T,\text{jet},\text{true}})$

1595 The observed distributions are unfolded using RooUnfold's 2D Bayesian (iter-  
 1596 ative) algorithm. Results are shown in figure 32.

### 1597 4.3.3 Pythia Response matrices

1598 A PYTHIA6 simulation was carried out to determine the response matrices. [Details](#)  
 1599 [of the simulation](#)

Table 5:  $j_T$  and  $p_T$  ranges used in unfolding. The same ranges are used for detector and truth level.

	$j_T$	$p_{T\text{jet}}$
Min	0.01	5
Max	20	500

1600 Response matrices are filled through correlation between MC detector and  
 1601 particle level jets and tracks.

1602 The ranges of both  $j_T$  and  $p_{T\text{jet}}$  extend the ranges in end results. These are  
 1603 shown in Tab. 5. The ranges are the same in detector and particle level.

1604 When calculating  $j_T$  for MC particles the code checks whether a corresponding  
 1605 detector level track exists and if that track had a  $j_T$  value. Additionally the code  
 1606 checks for detector level tracks that don't have corresponding particle level track  
 1607 or that track does not have  $j_T$  value.

1608 Possible cases:

- We find a corresponding track with a  $j_T$  value, response matrix is filled normally with  $(j_T^{obs}, p_T^{obs}, j_T^{true}, p_T^{true})$
- We don't find a corresponding track. Record  $(j_T^{true}, p_T^{true})$  as a miss
- We find a corresponding track, but it didn't have  $j_T$  value. Most likely because it was not part of a jet. Similary record  $(j_T^{true}, p_T^{true})$  as a miss
- For detector level tracks that have no correspondence in particle level set the code records  $(j_T^{obs}, p_T^{obs})$  as a fake

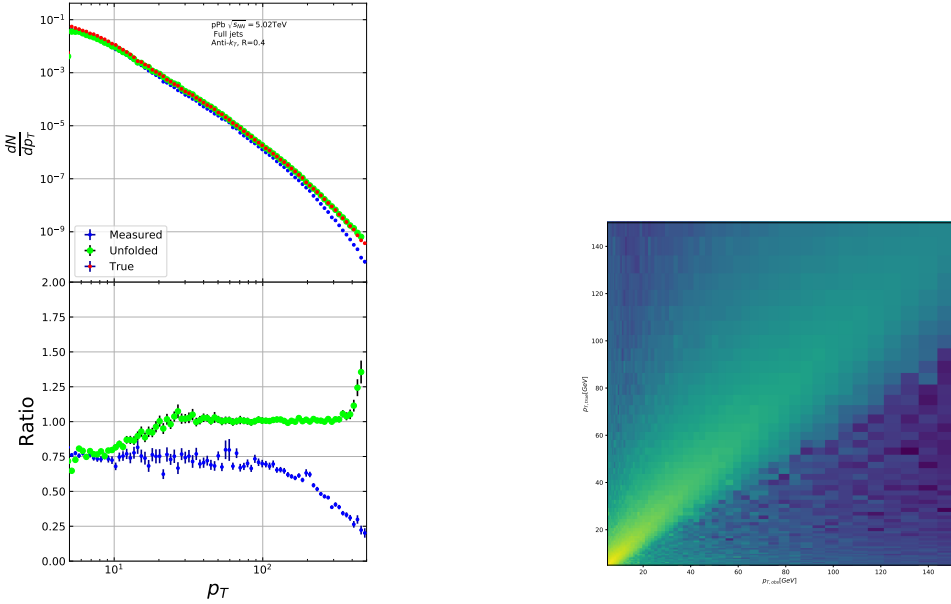
1616 In the analysis code the response matrix is made of an array of 3 dimensional  
 1617 histograms, with  $(j_{T,obs}, p_{T,obs}, j_{T,true})$  as axes. The histogram index gives the  $p_{T,true}$   
 1618 value.

#### 1619 4.3.4 Unfolding algorithm

1620 As a primary method unfolding is performed with an iterative (bayesian) algorithm  
 1621 using the RooUnfold [122] package. The number of iterations used is 4.

#### 1622 4.3.5 Unfolding closure test

1623 Pythia set is divided in 2 halves. First is used to fill the response matrices, as well  
 1624 as record missed and fake tracks. Second half is used to test the effectiveness of  
 1625 the unfolding method. Jet  $p_T$  distributions are shown in figure 33a and response  
 1626 matrix are shown in figure 33b.



(a) Unfolded jet  $p_T$  distribution in PYTHIA closure test (b) Jet  $p_T$  response matrix from unfolding closure test

Figure 33: Jet  $p_T$  in unfolding closure test

Response matrices within single jet  $p_T$  bins are shown in figure 34. Results from the closure test are shown in figure 35. In the lowest jet  $p_T$  bins unfolding fails to recover the true distribution. The lowest jet  $p_T$  bins are dominated by combinatorial jets and thus the true detector response is likely not retrieved.

Above jet  $p_T$  30-40 GeV the distribution is recovered well in the mid  $j_T$  region. At  $j_T < 0.1$  there is clear discrepancy. The final results are shown only for  $j_T > 0.1$ . Additionally there is some discrepancy at very high  $j_T$ . This is taken into account in the unfolding systematics. (TODO: Show this)

#### 4.4 Background

When calculating  $j_T$  distribution for jet constituents there is a contribution from underlying event (UE), i.e. tracks that just happen to be close to the jet axis. To find the signal coming from the actual jet we need to subtract the background (UE) contribution. On a jet-by-jet basis this is impossible, so one must estimate the background contribution in the inclusive distribution. A schematic view of the background contribution is shown in Fig. 36.

We have two methods for background estimation. In the first we look at the direction perpendicular to the jet. This is assumed to be the region least likely to

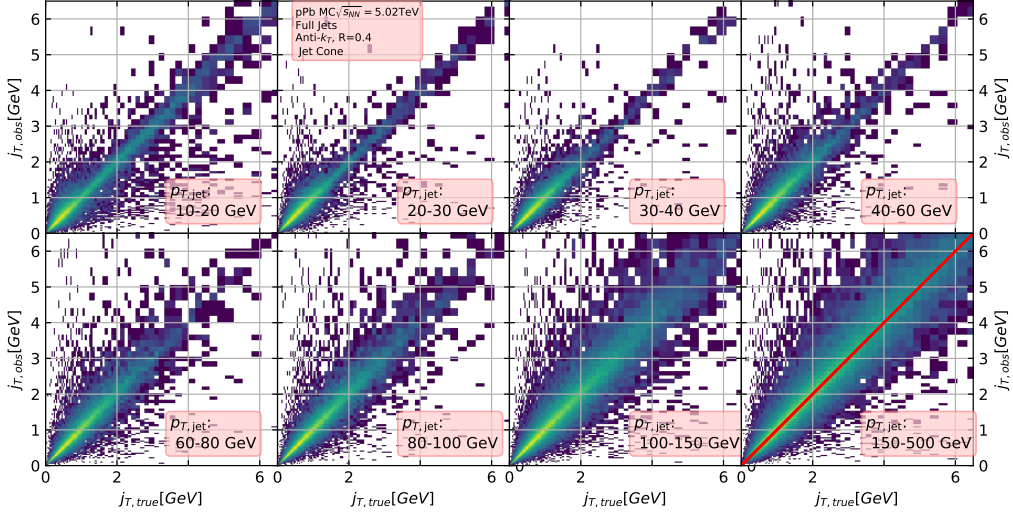


Figure 34:  $j_T$  Response matrices in single jet  $p_T$  bins

1644 contain jet contributions. In the second method we randomly assign the tracks of  
 1645 event new  $\phi$  and  $\eta$  values. The result is guaranteed to be uncorrelated.

#### 1646 4.4.1 Perpendicular cone background

1647 As a primary method to estimate the background we look at regions of the detector  
 1648 where there are no tracks from jets, but only uncorrelated tracks from the under-  
 1649 lying event. The underlying event is thus estimated by looking at an imaginary  
 1650 jet cone perpendicular to the observed jet axis ( $\frac{\pi}{2}$  Rotation in  $\phi$ ).

1651 After calculating the  $j_T$  values for tracks in the jet, we rotate the jet axis by  
 1652  $\frac{\pi}{2}$  in positive  $\phi$  direction. We check that there are no other jets closer than  $2R$  to  
 1653 the rotated axis. If there are then background calculation is skipped for this jet.  
 1654 Probability of this happening is 1-2% depending on the jet  $p_T$  bin.

1655 If we don't find other jets in the vicinity we move on to estimate the background.  
 1656 We find all tracks within a cone of radius  $R$  around the rotated axis and calculate  
 1657  $j_T$  of these tracks with respect to the rotated axis. Auto-correlations are added to  
 1658 match effect to jet. (see 4.4.3)

#### 1659 4.4.2 Random background

1660 In the random background method we look at all tracks in the event, except for  
 1661 tracks close to jets found by the jet algorithm. We randomly assign new  $\eta$  and  $\phi$   
 1662 values to all tracks using uniform distributions with  $|\eta| < 1.0$ .  $p_T$  values are kept  
 1663 the same. To increase statistics there is a possibility to create a number of random

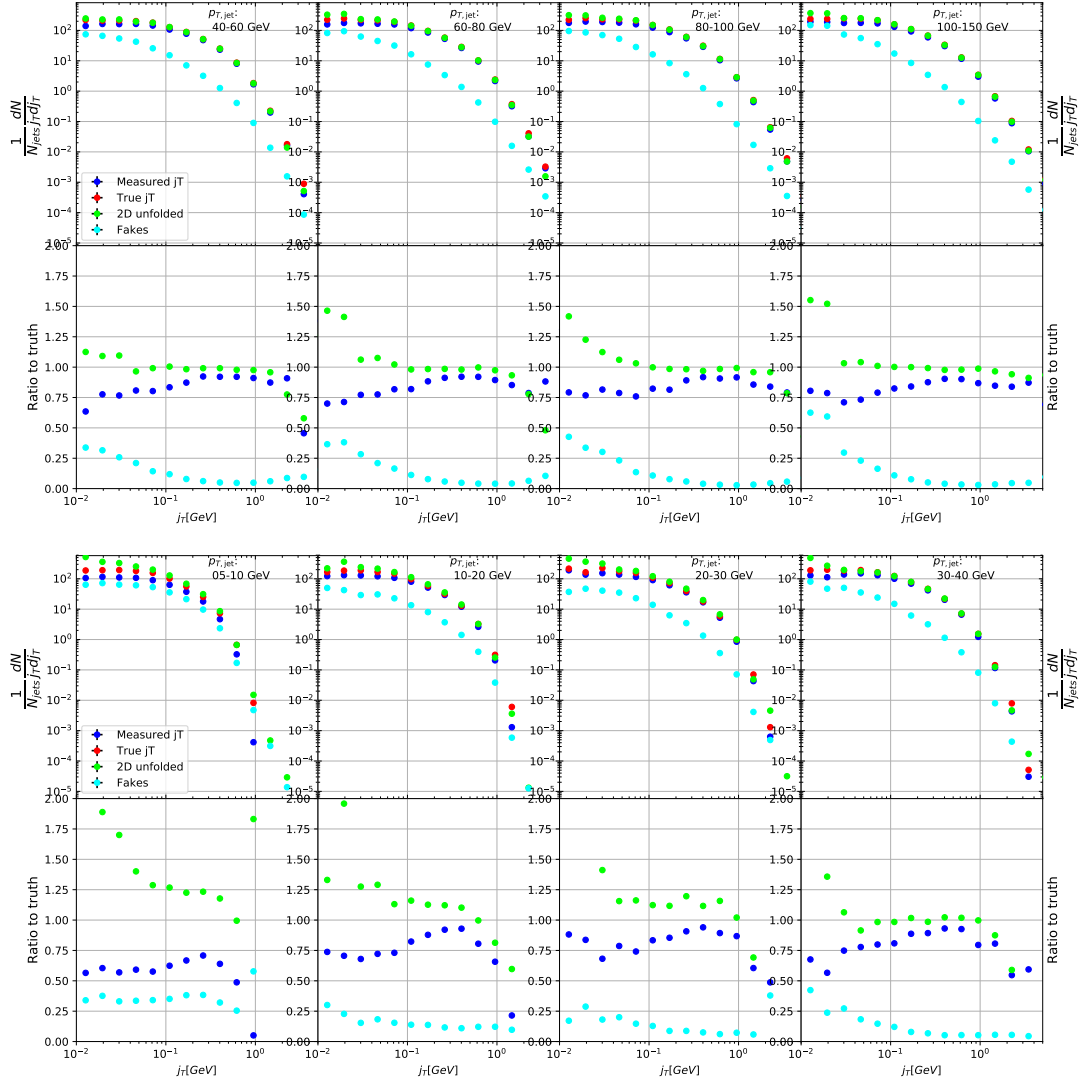


Figure 35: Pythia closure test results. Fake tracks include also tracks that do exist in the true dataset, but for one reason or another were not given  $j_T$  values.  $j_T$  is only calculated for tracks that are associated with jets

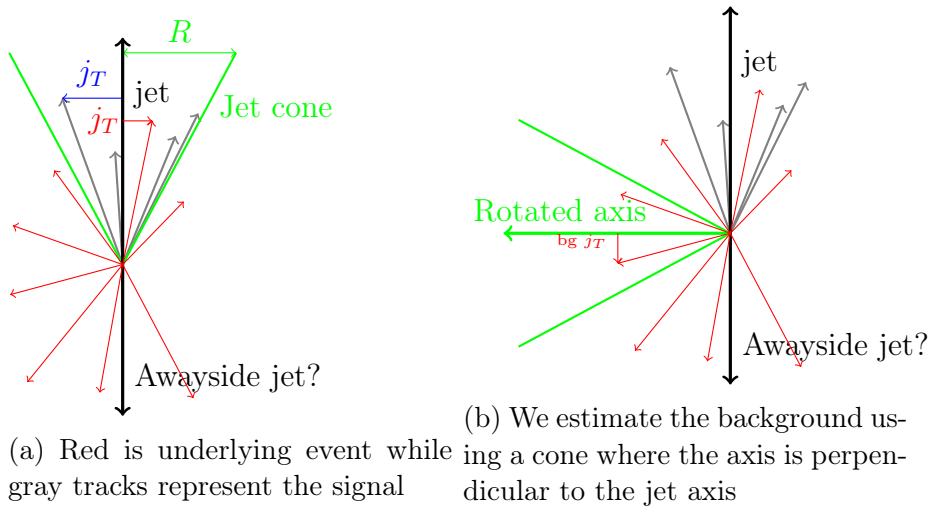


Figure 36: Background estimation

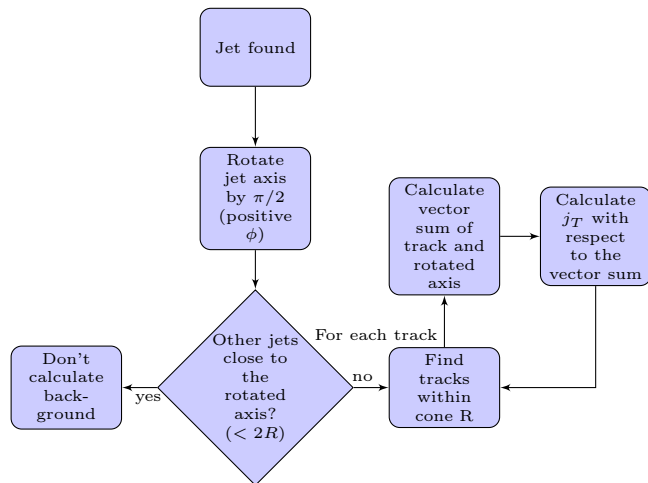


Figure 37: Flowchart representation of the perpendicular cone background procedure

1664 tracks for each actual track. In the analysis we do this 10 times for each track.  
1665 Again the track  $p_T$  value is kept the same.

1666 We create a random jet cone from uniform  $\eta$  and  $\phi$  distributions. Here  $|\eta| <$   
1667 0.25. Now we calculate  $j_T$  of the random tracks with respect to the random cone  
1668 axis. Auto-correlations are added before calculating  $j_T$  (see 4.4.3)

#### 1669 4.4.3 Auto-correlations

1670 Jet axis is simply a vector sum of all its constituents. Thus having an additional  
1671 track in the jet from the underlying event moves the jet axis towards this track.  
1672 Since the axis is now closer to the track, it has a smaller  $j_T$  value. Assuming a  
1673 1 GeV background track at the edge of a  $R = 0.4$  the  $j_T$  value would be 0.5 GeV.  
1674 If this is added to a 5 GeV jet, the  $j_T$  value becomes 0.33 GeV. In a 50 GeV jet it  
1675 would be 0.39 GeV. **CHECK** This is a region where the inclusive  $j_T$  distribution is  
1676 dominated by background. The distribution is also steeply falling. Overestimating  
1677 the background can lead to a situation where the background estimation exceeds  
1678 the inclusive distribution.

1679 To take this effect into account we can't use a fixed axis for background, but  
1680 it has to behave like a jet would when additional tracks are added. Thus before  
1681 calculating  $j_T$  values we make a vector sum of the track and the axis used for back-  
1682 ground, which is either the perpendicular cone axis or the random axis depending  
1683 on the background method. In each case the momentum of this background axis  
1684 is assumed to be the same as the jet which initiated the background estimation.

1685 In pPb data there is on average about one underlying event track in a  $R = 0.4$   
1686 cone. If there would be more, one should consider taking the vector sum of all  
1687 tracks inside the cone. As there is usually only one track and if there are more it's  
1688 unlikely that more than one has high momentum, taking the vector sum track-by-  
1689 track should be enough.

#### 1690 4.4.4 Background methods

1691 Comparison between perpendicular cone and random background in figure 38. The  
1692 advantage of the random background method is the added amount of statistics as  
1693 the procedure can be repeated several times for each event. However, it seems that,  
1694 especially in the highest  $p_{T\text{jet}}$  bins there is some jet contribution left at the high  
1695 end. One should note that the results from perpendicular cone background show no  
1696 observable change between  $p_{T\text{jet}}$  bins. It is a good indication that the background  
1697 is actually dominated by the underlying event over the entire  $j_T$  region.

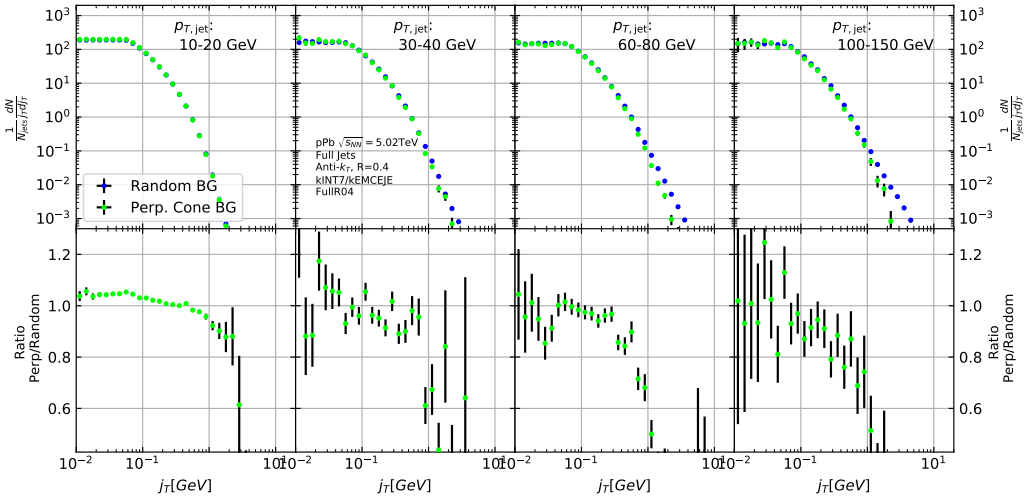


Figure 38:  $j_T$  background with two different methods

## 1698 4.5 Fitting

1699 The resulting signal distribution are fitted with a 2 component function shown in  
 1700 Eq. 46. Gaussian distribution is used for low  $j_T$  and an inverse gamma function  
 1701 is used for high  $j_T$ . The gaussian is taken to have the center at  $j_T = 0$ . In total  
 1702 this gives 5 parameters. The fitting procedure was inspired by the dihadron  $j_T$   
 1703 analysis by ALICE [2]. The complete fitting function is

$$\frac{1}{N_{\text{jets}} j_T \text{d}j_T} \frac{\text{d}N}{\text{d}j_T} = \frac{B_2}{B_1 \sqrt{2\pi}} e^{-\frac{j_T^2}{2B_1^2}} + \frac{B_3 B_5^{B_4}}{\Gamma(B_4)} j_T^{-B_4+1}. \quad (46)$$

1704 To achieve stable results the fitting is performed in two steps. First each  
 1705 component is fitted separately. Gaussian component is fitted to the low end in  $j_T$ .  
 1706 Inverse gamma component is fitted to  $j_T$  above 1 GeV/c. After getting the results  
 1707 from the individual fits they are combined into a single function with initial values  
 1708 from the individual results and an additional fit is performed. Fitting only the  
 1709 gaussian component to the entire distribution produces approximately the same  
 1710 result as the gaussian component in the two-component model.

1711 After getting the fit function  $\sqrt{\langle j_T^2 \rangle}$  (RMS) and yield values are extracted  
 1712 separately from each component. The narrow component RMS is

$$\sqrt{\langle j_T^2 \rangle} = \sqrt{2} B_1,$$

1713 and the wide component RMS value is calculated as

$$\sqrt{\langle j_T^2 \rangle} = \frac{B_5}{\sqrt{(B_4 - 2)(B_4 - 3)}},$$

<sub>1714</sub> where it is required that  $B_4 > 3$ .

<sub>1715</sub> The statistical errors can be calculated with the general error propagation  
<sub>1716</sub> formulas. As a result one gets errors for the narrow component RMS

$$\delta \sqrt{\langle j_T^2 \rangle} = \sqrt{2} \delta B_1 \quad (47)$$

<sub>1717</sub> and for the wide component RMS

$$\delta \sqrt{\langle j_T^2 \rangle} = \sqrt{\left( \frac{(5 - 2B_4) B_5 \delta B_4}{(2(B_4 - 2)(B_4 - 3))^{\frac{3}{2}}} \right)^2 + \left( \frac{\delta B_5}{\sqrt{(B_4 - 2)(B_4 - 3)}} \right)^2} \quad (48)$$

1718

## 5 Systematic errors

1719 **Extend Systematics** The systematic uncertainties in this analysis come from the  
1720 background estimation, the unfolding procedure and the cuts used to select the  
1721 tracks. Tracking uncertainties are estimated from variations of the track selection  
1722 cuts defined in Sec. ???. The resulting variations in RMS are shown in Table  
1723 7. The uncertainties from unfolding and background subtraction are of the same  
1724 magnitude.

1725 The systematics in background estimation were studied using an alternative  
1726 method to extract the background, mainly the random background method. The  
1727 resulting uncertainty is below 5% for the wide component RMS and below 9% for  
1728 the narrow component RMS.

1729 The systematic uncertainty that arises from the unfolding procedure is esti-  
1730 mated by performing the unfolding with two separate methods. Data corrected  
1731 by the iterative unfolding method are used as the results and the SVD unfolding  
1732 method is employed to estimate the uncertainty. In a PYTHIA closure test the  
1733 true distribution was in general found to be between the unfolded distributions  
1734 from the iterative and SVD method. The difference between the methods when  
1735 unfolding data should give a reasonable estimate of the unfolding uncertainty. The  
1736 resulting uncertainty is below 8% for both wide and narrow component RMS.

1737 The different source of the systematic uncertainty are considered as uncorre-  
1738 lated and the values of each source are summed in quadrature. The resulting  
1739 uncertainty is 9 % for the wide component RMS and 12 % for the narrow compo-  
1740 nent RMS.

Table 6: Summary of systematic errors

Systematic	Wide RMS	Narrow RMS
Background	5 %	9 %
Unfolding	8 %	8 %
Tracking	? %	? %
Total	9 %	12%

1741

### 5.1 Background

1742 Fits are performed on both perpendicular cone and random background signals.  
1743 Difference between them is taken as the systematic error. The fits for individ-  
1744 ual bins from the random background method are shown in figure 39. Resulting  
1745 differences between the methods for different components are shown in figure 40.

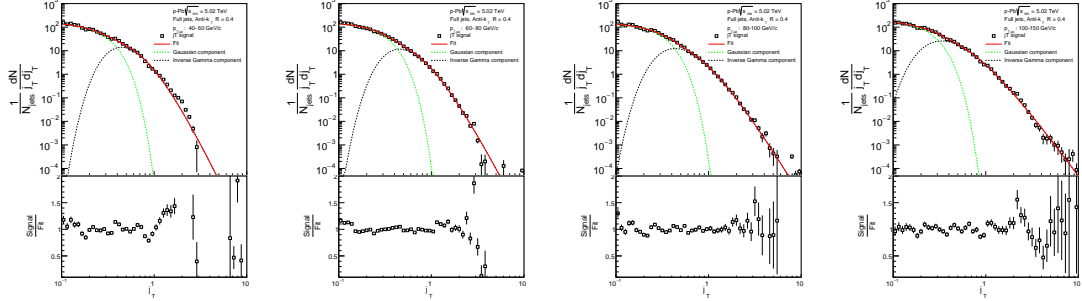


Figure 39:  $j_T$  signal with random background subtraction fits in different jet  $p_T$  bins

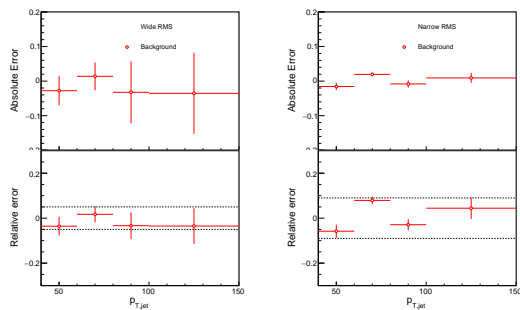


Figure 40: Differences between perpendicular cone and random background subtraction in the resulting RMS values.

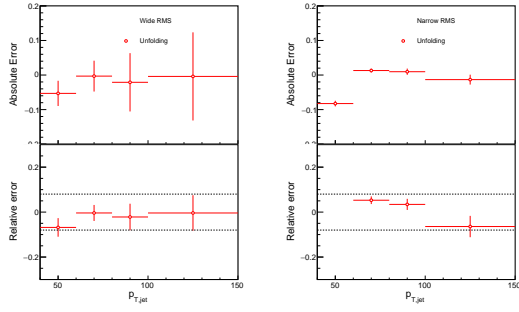


Figure 41: Differences between Bayesian and SVD unfolding in the resulting RMS values

## 1746 5.2 Unfolding

1747 Unfolding is performed using both SVD and Bayesian unfolding. Difference be-  
1748 tween the methods is taken as the systematic error. Since SVD unfolding does  
1749 not have a 2 dimensional options, the unfolding is done bin by bin. The resulting  
1750 distributions after SVD unfolding and background subtraction with the perpen-  
1751 dicular cone method are shown in fig ???. Resulting differences between the methods  
1752 for different components are shown in figure 41.

### 1753 5.2.1 Effect of number of iterations

1754 The iterative unfolding algorithm permits the change of number of iterations.  
1755 The unfolding was carried out using different numbers of iterations. The results  
1756 from these different cases are shown in Fig. 42. The results are compared to the  
1757 default unfolding algorithm with 4 iterations. The difference in results between  
1758 the different cases is mostly less than 2.5%.

### 1759 5.2.2 Effect of different prior

1760 The iterative algorithm requires a prior estimate of the shape of the distribution.  
1761 As a default prior the truth (particle level) distribution is used. To test the effect  
1762 of changing the prior we instead use the unfolded  $j_T$  distribution as prior. The  
1763 results are compared to the unfolding algorithm with the default prior. This is  
1764 shown in Fig. 43 The difference in results between the different cases is mostly less  
1765 than 2.5%.

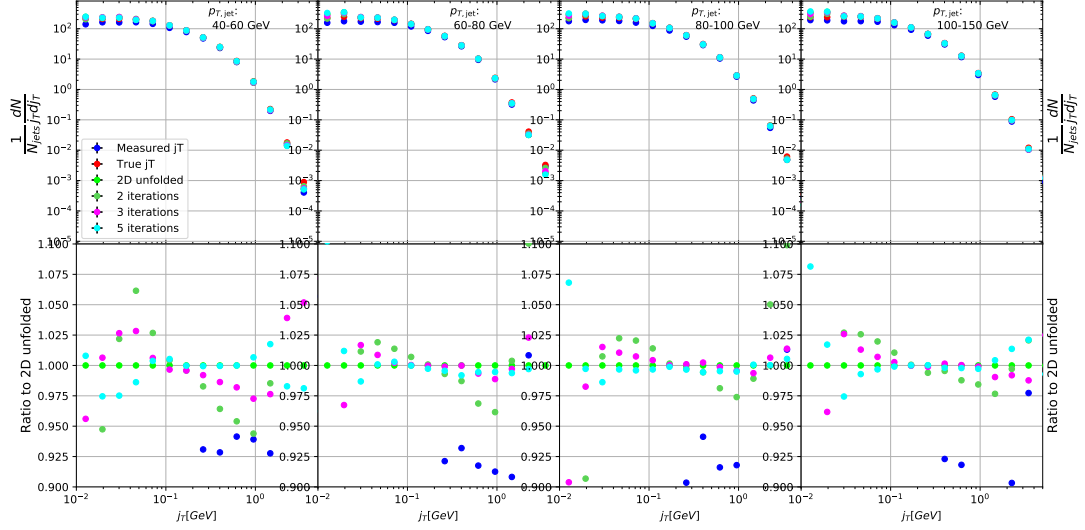


Figure 42: Unfolding with different number of iterations

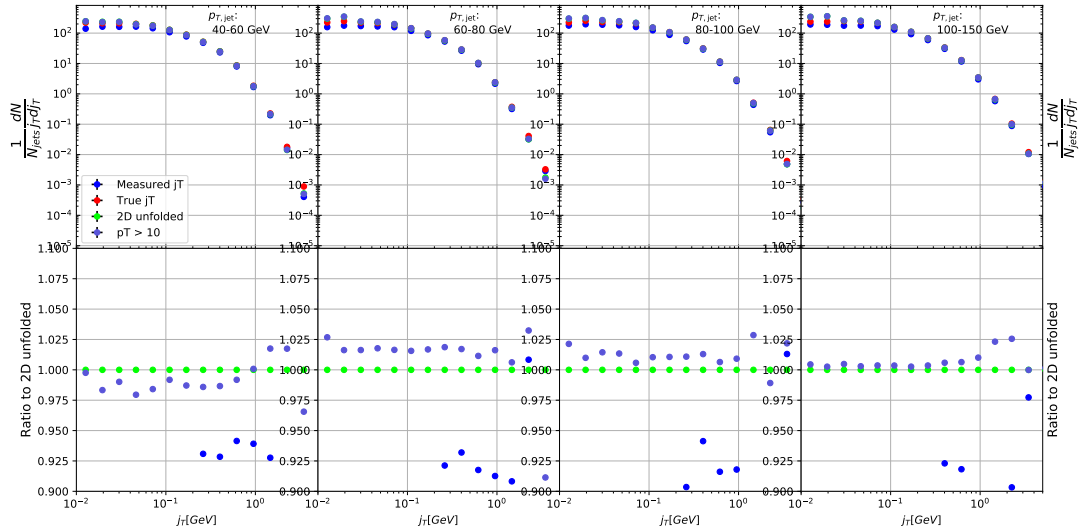


Figure 43: Effect of changing minimum jet  $p_T$  used in unfolding from 5 to 10 GeV

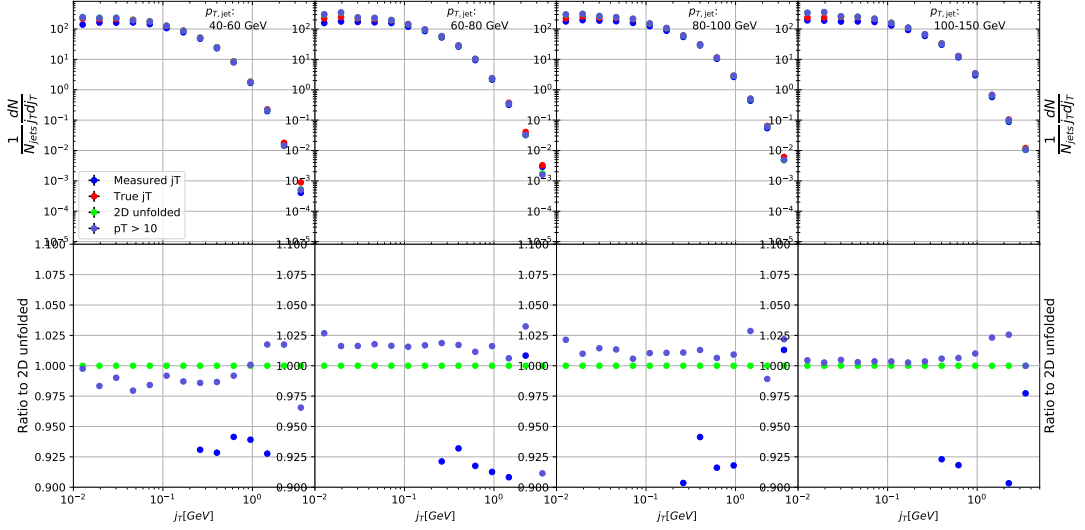


Figure 44: Effect of changing minimum jet  $p_T$  used in unfolding from 5 to 10 GeV

### 1766 5.2.3 Effect of $p_T$ truncation

1767 As an additional check the unfolding is carried out with different  $p_{T\text{jet}}$  truncation  
 1768 values. By default the full range of  $p_{T\text{jet}} > 5\text{GeV}$  is used. As an option the we test  
 1769 the unfolding by only using the response matrix for  $p_{T\text{jet}} > 10\text{GeV}$ . The results of  
 1770 this test are shown in Fig. 44

## 1771 5.3 Tracking

1772 Systematic effects originating from uncertainty in the tracking efficiency are es-  
 1773 timated through a PYTHIA simulation, where an artificial inefficiency of 3% is  
 1774 introduced. i.e. 3 % of tracks are randomly removed from each event.

## 1775 5.4 EMCAL

1776 The analysis uses EMCAL clusters only in the reconstruction of jets. Thus the  
 1777 only way uncertainty in EMCAL performance can affect the results is through  
 1778 modification of jet momentum or axis.

1779 Uncertainty related to the EMCAL energy scale was estimated by scaling clus-  
 1780 ter energies up and down by 2 % in a PYTHIA particle level simulation. Similarly  
 1781 the jet momentum was scaled by  $\pm 2\%$  when determining the jet  $p_T$  bin. In the  
 1782 analysis EMCAL is used only in jet reconstruction, not for calculating  $j_T$ . The  
 1783 only ways EMCAL uncertainty can affect the analysis are changes in jet energy

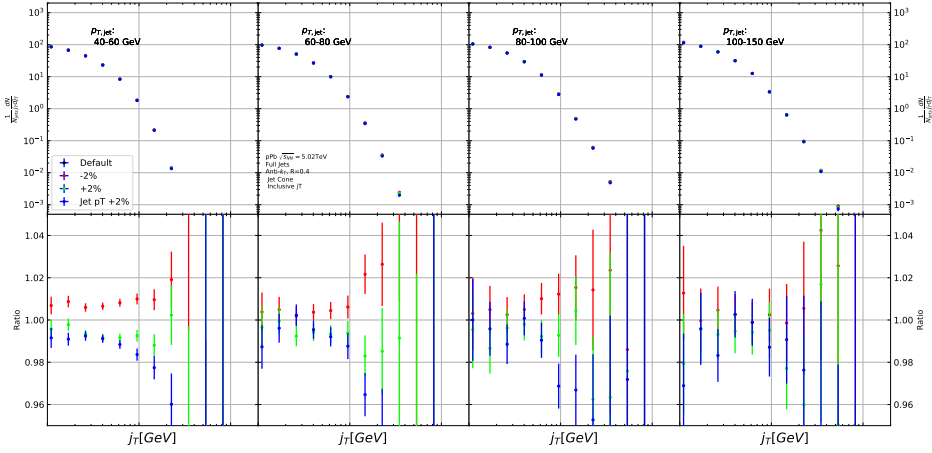


Figure 45: Results from PYTHIA simulations with Cluster energies scale up/down by 2 %. Additionally jet momenta were scaled by 2 % when determining the jet  $p_T$  bin.

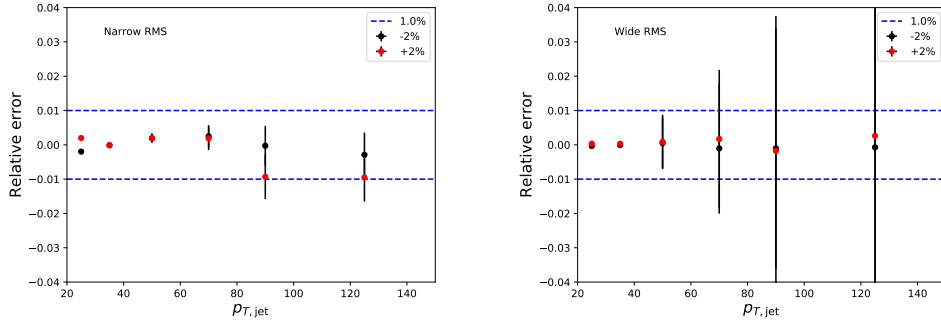


Figure 46: Relative systematic errors resulting from cluster energy uncertainty.

and jet axis. Jet axis shouldn't significantly change, so the main contribution should be changes in jet  $p_T$  bin.

The results are shown in Fig. 45. The resulting systematic uncertainties are shown in Fig. 46. The uncertainty is taken to be 1%.

## 5.5 Summary

There is no tracking and no unfolding uncertainty in the Monte Carlo simulations.

1790 **5.6 Comparison between A and C side**

1791 In 2013 there were issues with tracking. To rule out effects on  $j_T$  distributions a  
1792 study was performed comparing  $j_T$  distributions between A and C side. 1793 Which  
1794 is lead going side and which is proton going No systematic differences were ob-  
1795 served. Figure 49 shows the comparison between inclusive distributions between  
the different sides, both for minimum bias and EMCAL triggered datasets.

1796 **5.7 Subtracted signal**

1797 Results in figure 48. Comparison between signals with different backgrounds in  
1798 figure 49

1799 **5.8 Combining systematics**

1800 Resulting systematic errors are shown in table 7. Systematic errors are combined  
bin-by-bin in quadrature to get the total systematic errors.

Table 7: Summary of systematic errors

Systematic	Wide RMS	Narrow RMS
Background	5 %	9 %
Unfolding	8 %	8 %
Tracking	%	%
EMCAL	%	%
Total	9 %	12%

1801

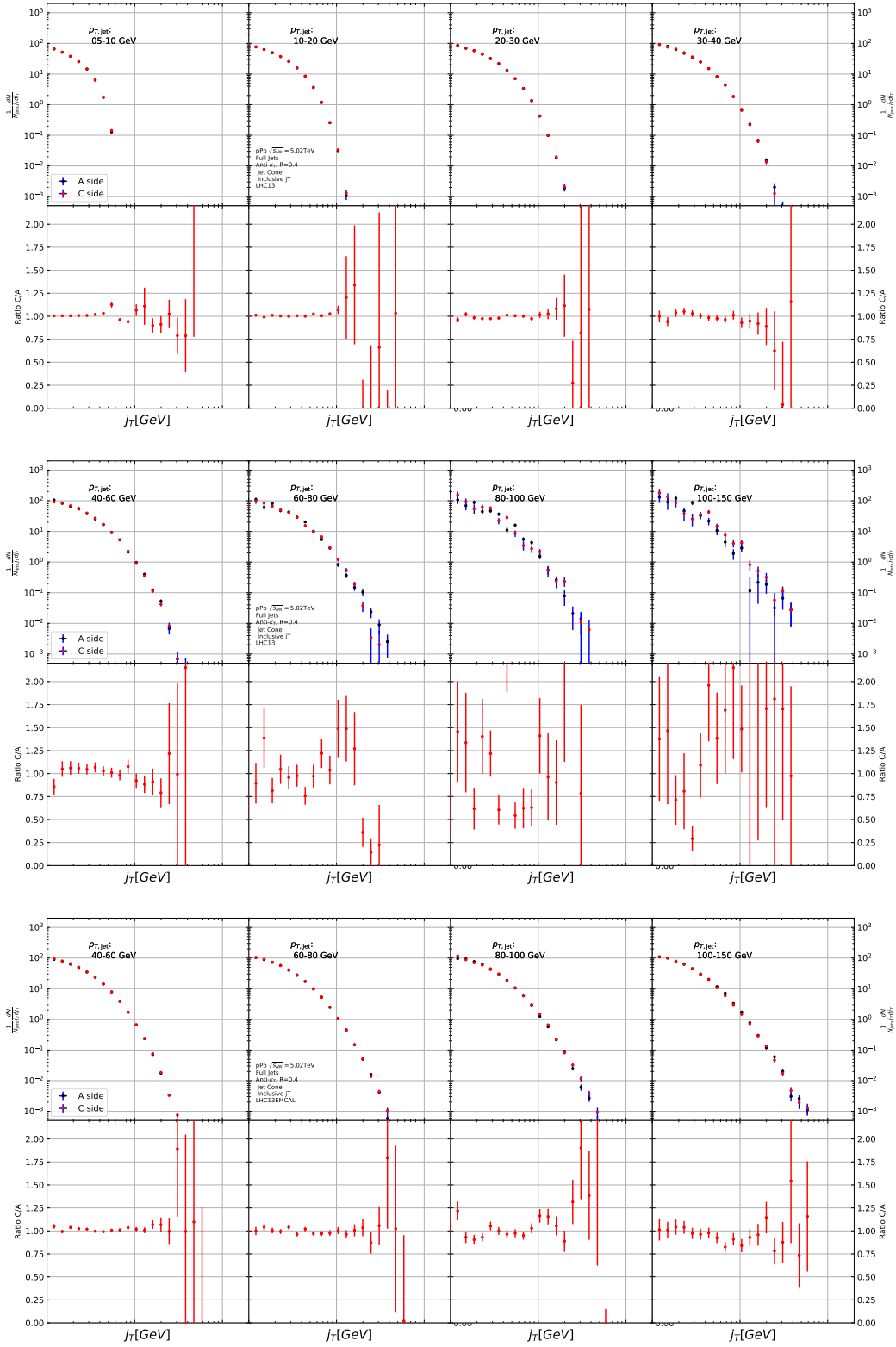


Figure 47: Comparison of inclusive  $j_{T86}$  distributions between A and C side for minimum bias and EMCAL triggered data.

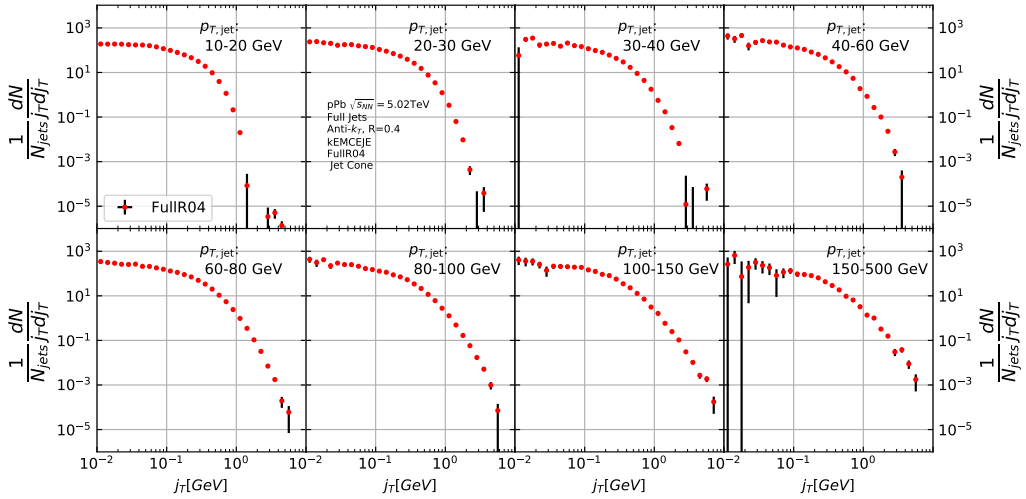


Figure 48:  $j_T$  signal with background subtracted

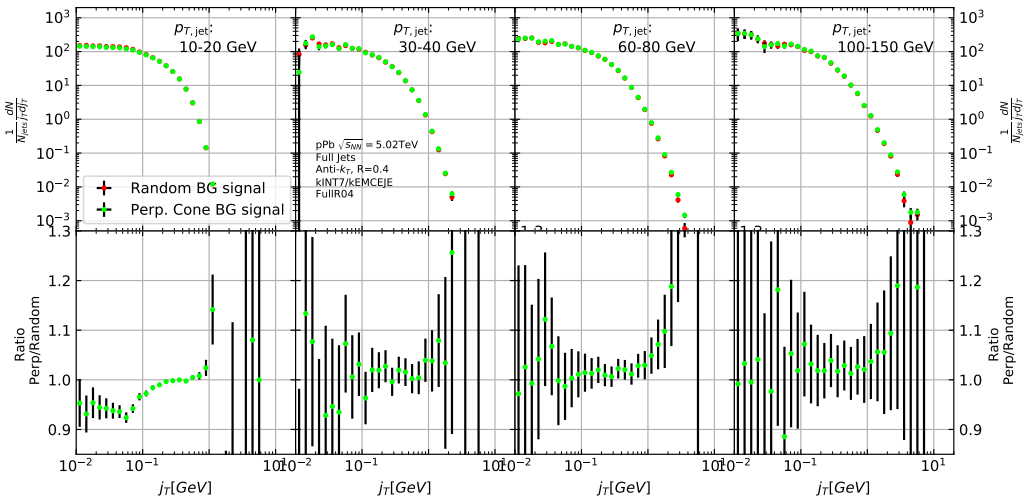


Figure 49: Comparison of the effect of background method on  $j_T$  signal.

## 1802 6 Results

### 1803 6.1 Fitting

1804 Fits of  $j_T$  distributions in different jet  $p_T$  bins with  $p_T > 40\text{GeV}$  are shown in figure  
 1805 50. Additional jet  $p_T$  bins are shown in appendix ???. In lowest jet  $p_T$  bins the  
 1806 jets are mainly combinatorial which makes background subtraction and unfolding  
 1807 difficult and thus the signal can't be trusted.

1808 The fits describe the data well. There is some fluctuation of the order of 10 %  
 1809 around the fit function. At hight  $j_T$  the statistical errors in the signal are large.

#### 1810 6.1.1 RMS values from fitted distributions

1811 RMS results with systematic errors are shown separately in figure 51. Figure 52  
 1812 shows RMS values for both components combined. The figure also includes results  
 1813 from a PYTHIA simulation.

## 1814 6.2 High multiplicity

1815 The analysis was repeated taking only events with high multiplicity. Three dif-  
 1816 ferent multiplicity cuts were used; 10%, 1% and 0.1%. We used ZDC(TODO)  
 1817 as a centrality estimator. As argued in section ?? the zero-degree energy deposit  
 1818 should provide a centrality estimator with minimal bias from jets production. Re-  
 1819 sulting  $j_T$  distributions are shown Fig. 53. As the statistics are limited in the high  
 1820 multiplicity runs, it was hard to achieve stable fits to the distributions, thus the  
 1821 RMS values are not shown.

1822 From the figure one can observe no systematic modification when tighter mul-  
 1823 tiplicity cuts are introduced.

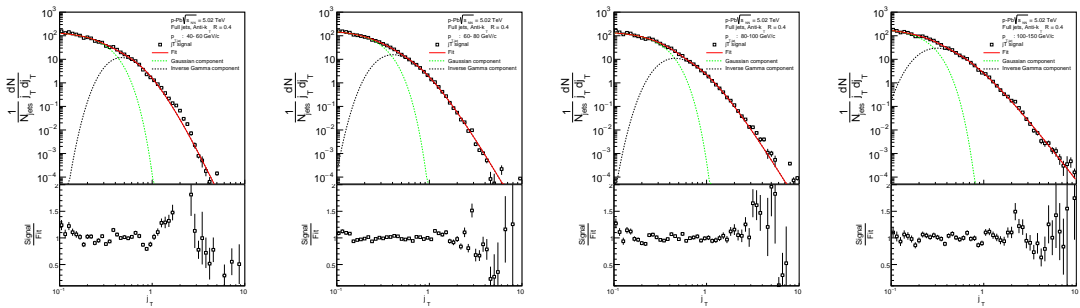


Figure 50:  $j_T$  signal fits in different jet  $p_T$  bins

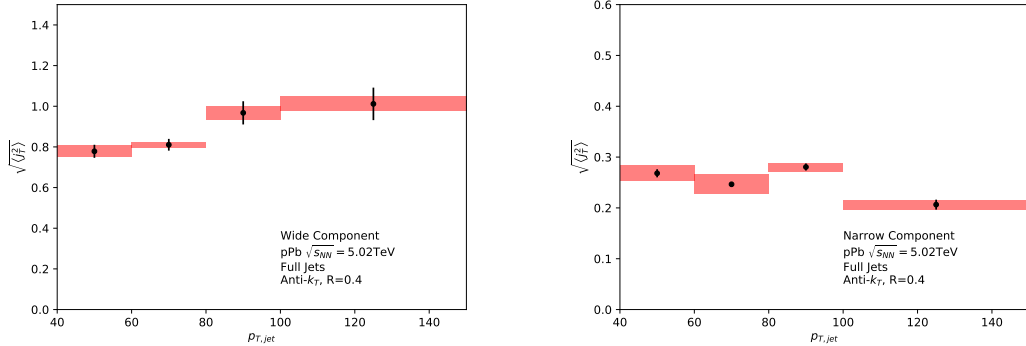


Figure 51: RMS values extracted from the fits for the gaussian (narrow) and inverse gamma (wide) components

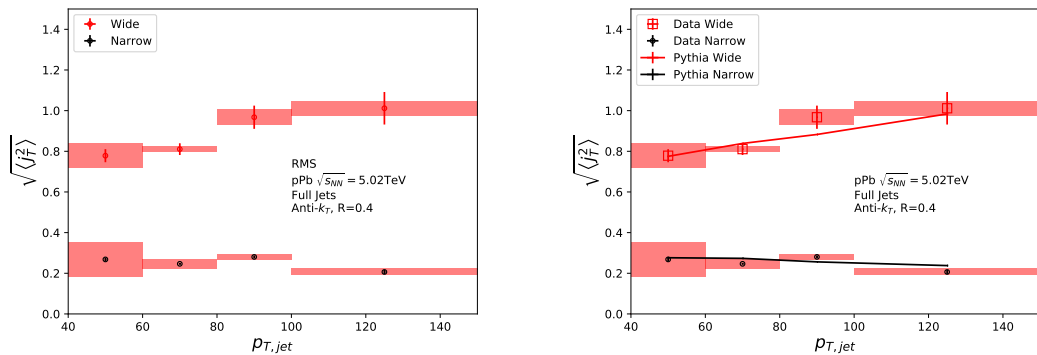


Figure 52: RMS values extracted from the fits for the gaussian (narrow) and inverse gamma (wide) components

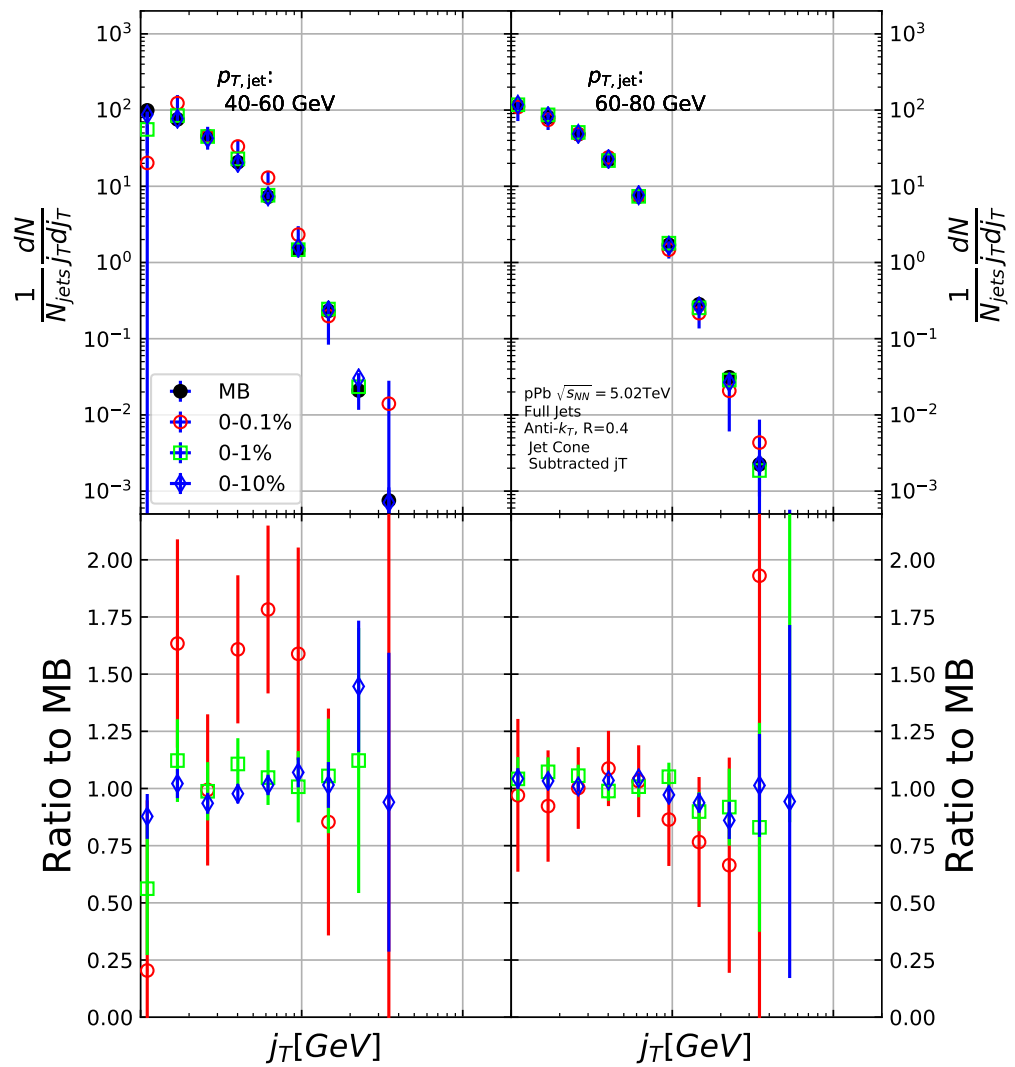


Figure 53:  $j_T$  distributions for high multiplicity p–Pb events

## 1824 7 Discussion

1825 [123, 124]

### 1826 7.1 Dihadron $j_T$

1827 The jet fragmentation transverse momentum  $j_T$  has been studied previously at  
 1828 ALICE with dihadron correlations [2]. The study took the leading hadron in  
 1829 each event and calculated  $j_T$  for any near-side tracks with respect to the leading  
 1830 hadron. Thus there is no kinematical limit to  $j_T$  from the jet cone. In the analysis  
 1831 the background shape is estimated using pairs with large  $\Delta\eta$ . The normalisation of  
 1832 the background is done when fitting the  $j_T$  distribution. The inclusive and signal  
 1833 distributions from the analysis are shown in Fig. 54. The inclusive distribution is  
 1834 fitted with a three component function,

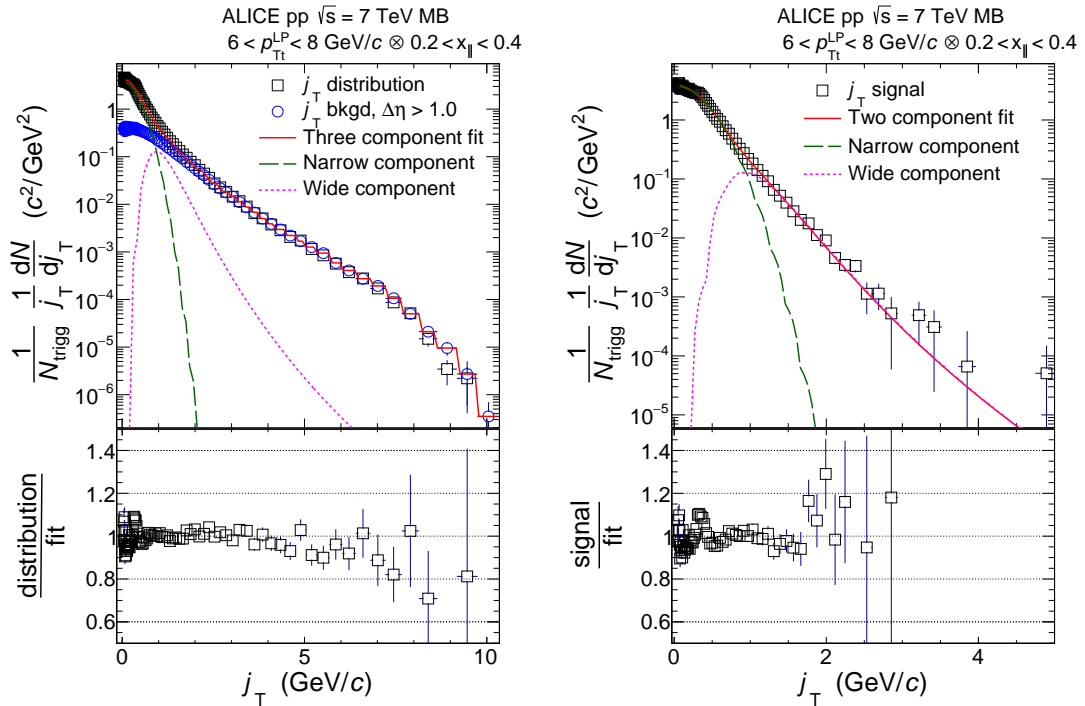


Figure 54: *Left:* Measured  $j_T$  distribution including a three-component fit. The three components describe the background (circular symbols), hadronization (long dashed line), and showering (short dashed line). *Right:* The same  $j_T$  distribution but with background subtracted.

1835 The analysis was the first to introduce this factorisation of  $j_T$  into components.

At  $j_T \approx 0.4\text{GeV}$  there is a small bump in the distribution to fit ratio. This was attributed to cases where the trigger particle decayed after hadronisation. As it is difficult to correct for, this bump is included in the systematic errors of the results.

The RMS results from the fitting in both pp and p–Pb collisions are shown in Fig. 55. Qualitatively the results are similar to jet  $j_T$  results. The RMS value of the wide component has an increasing trend with respect to  $p_{Tt}/p_{Tjet}$ , while the RMS value of the narrow component stays constant. Both components are well described by PYTHIA simulations. As seen in the figures there is no difference between pp and p–Pb results in the dihadron analysis.

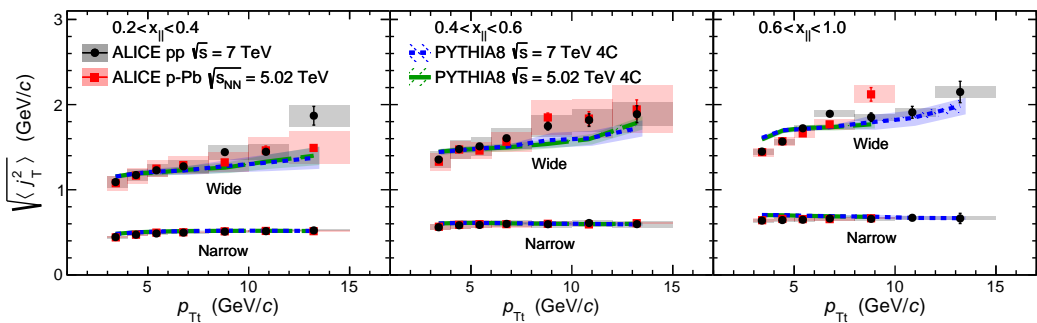


Figure 55: RMS values of the narrow and wide  $j_T$  components in the dihadron correlation analysis. Results from pp collisions at  $\sqrt{s} = 7\text{ TeV}$  (circular symbols) and from p–Pb collisions at  $\sqrt{s_{NN}} = 5.02\text{ TeV}$  (square symbols) are compared to PYTHIA 8 tune 4C simulations at  $\sqrt{s} = 7\text{ TeV}$  (short dashed line) and at  $\sqrt{s} = 5.02\text{ TeV}$  (long dashed line). Different panels correspond to different  $x_{\parallel}$  bins with  $0.2 < x_{\parallel} < 0.4$  on the left,  $0.4 < x_{\parallel} < 0.6$  in the middle, and  $0.6 < x_{\parallel} < 1.0$  on the right. The statistical errors are represented by bars and the systematic errors by boxes. [2]

## 7.2 Comparing to dihadron and jet $j_T$ results

Comparison to RMS values in dihadron analysis [?] are shown in figure 56 Dihadron results from [?]. For comparison the dihadron trigger  $p_T$  bins are converted to jet  $p_T$  bins and vice versa. Bin-by-bin comparison is still not possible, but dihadron analysis gives systematically larger RMS values. This could be caused by several kinematical factors. In jet  $j_T$  analysis the jet cone limits possible  $j_T$  values and thus the width and RMS of the  $j_T$  distributions. The effect of this limitation can be studied by changing the cone size as is described in section 7.2.1.

Comparison to  $j_T$  results from dihadron analysis [?] is shown in figure ???. Trigger  $p_T$  bins used in dihadron analysis are converted to jet  $p_T$  bins using ob-

1856 served average jet  $p_T$  values in leading track momentum bins. Similarly jet  $p_T$  bins  
 1857 are converted to  $p_{T,\text{trigger}}$  bins using average leading track  $p_T$  values in  $p_{T,\text{jet}}$  bins.

1858 The trends are similar in dihadron and jet  $j_T$  results. Wide component RMS  
 1859 values tend to increase with increasing  $p_{T,\text{trigger}}/p_{T,\text{jet}}$ . Narrow component RMS  
 1860 increases slightly in dihadron analysis but not in jet  $j_T$ , WHY? (Depends on  $x_{\parallel}$   
 1861 bin in dihadron)

1862 In general dihadron  $j_T$  gives wider distributions with larger RMS values. In  
 1863 jet analysis the cone size limits width and thus the RMS values. The effect of this  
 1864 limitation can be studied by changing the cone size as is described in section 7.2.1.

1865 Additionally the leading track is an imperfect estimate of the jet/original par-  
 1866 ton. Because the leading track in general is at an angle compared to the jet axis,  
 1867 the resulting  $j_T$  values are different. In practice the jet axis found by the jet finding  
 1868 algorithm tends to minimize the average  $j_T$  of jet constituents. Thus the yield  
 1869 at high  $j_T$  is limited and the RMS values are smaller. The effect of having the  
 1870 leading hadron as reference instead of the jet axis is discussed in section 7.2.2

1871 Lastly the results from the dihadron analysis are done in  $p_{T,\text{trigger}}$  bins. This  
 1872 favours hard jets, i.e. jets where the leading hadron carries a large momentum  
 1873 fraction and the jet multiplicity is small. In  $p_{T,\text{jet}}$  bins jets are more likely to be  
 1874 soft, i.e. small leading momentum fraction and high multiplicity jets.

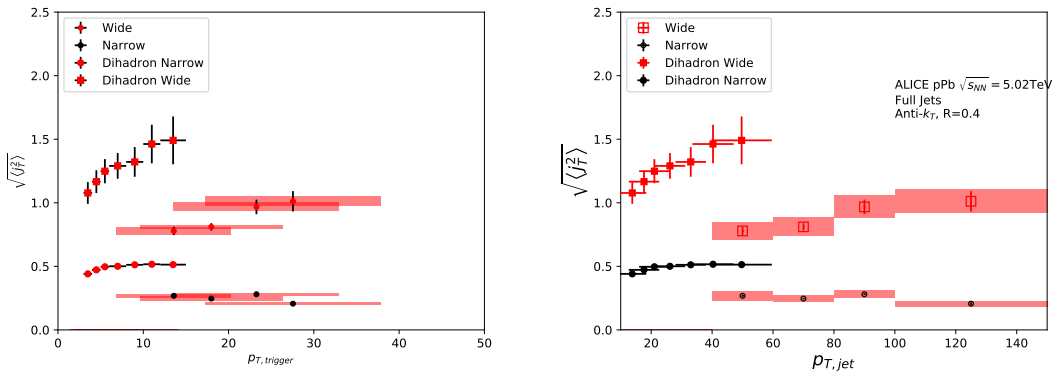


Figure 56: Jet  $j_T$  results are compared to results obtained in the dihadron analysis. Dihadron trigger  $p_T$  bins are converted to jet  $p_T$  bins using observed mean  $p_{T,\text{jet}}$  values in  $p_{T,\text{trigger}}$  bins. Dihadron results are for  $0.2 < x_{\parallel} < 0.4$

### 1875 7.2.1 Different $R$ parameters

1876 The size of the jet cone gives a limit for  $j_T$ . For a track with a fixed momentum  $p$   
 1877 this is a hard limit. This is conveniently seen as  $j_T$  can be given in terms of cone  
 1878 size  $R$  and momentum  $p$  in the small angle approximation limit as

$$j_T \approx p \cdot R \quad (49)$$

1879 Thus for tracks with  $p_{T\text{track}} < p_{T0}$ ,  $j_T < p_{T0} \times R$ .

1880 In practice the effect of cone sizes on  $j_T$  distribution is studied in a PYTHIA simulation.  
 1881 Results of the individual distributions and resulting RMS values from this simula-  
 1882 tion are shown in Fig. 57 and Fig. 58 respectively. Increasing the cone size of jets  
 1883 gives more room for high  $j_T$  tracks. This is seen in the individual  $j_T$  distributions  
 1884 as increased high  $j_t$  production. At low  $j_T$  there is no change.

1885 When looking at RMS values from wide component we see an increase/decrease  
 1886 of about 10% when going from  $R = 0.4$  to  $R = 0.5/R = 0.3$ .

1887 The message from narrow component RMS values is less clear. At low jet  $p_T$   
 the behaviour is similar, but at high  $p_T$  the order is reversed.

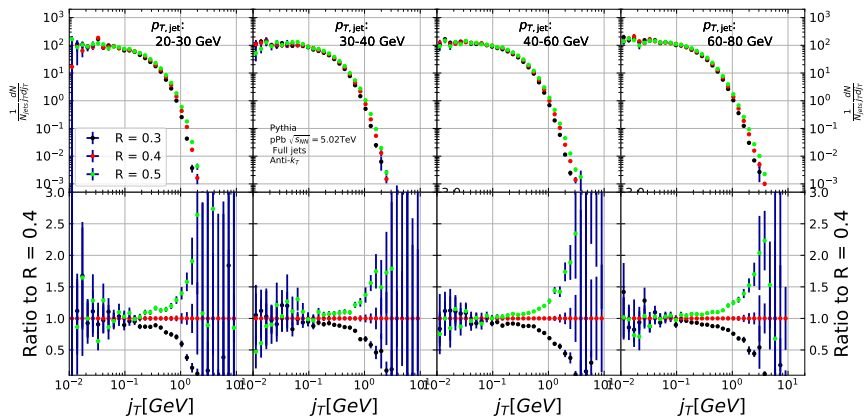


Figure 57: Effect of changing  $R$  parameter in jet finding on  $j_T$  distributions

1888

### 1889 7.2.2 Leading tracks versus jet

1890 The leading track is an imperfect estimate of the jet/original parton. Because the  
 1891 leading track in general is at an angle compared to the jet axis, the resulting  $j_T$   
 1892 values are different. In practice the jet axis found by the jet finding algorithm  
 1893 tends to minimize the average  $j_T$  of jet constituents. Thus the yield at high  $j_T$  is  
 1894 limited and the RMS values are smaller.

1895 A PYTHIA study was performed where  $j_T$  was calculated with respect to the  
 1896 leading track momentum, instead of the jet axis. The results are shown in Fig. 59.  
 1897 The resulting  $j_T$  distributions are significantly wider than  $j_T$  distributions from  
 1898 the typical method. The effect seems to be larger than the effect seen in comparing  
 1899 different  $R$  values.

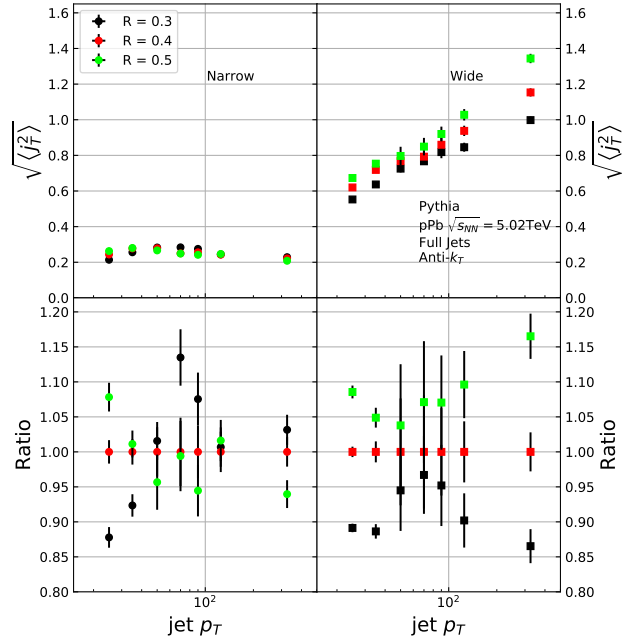


Figure 58: Effect of changing  $R$  parameter in jet finding on narrow and wide component RMS values. Wide component RMS values increase with increasing cone size.

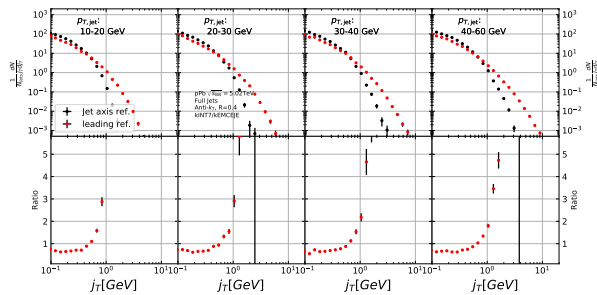


Figure 59: Results of calculating  $j_T$  with respect to the jet axis or the leading hadron. The assumption is that because the leading hadron is an imperfect estimate of the jet axis, low  $j_T$  tracks should on average be shifted to higher  $j_T$

<sub>1900</sub> **8 Summary**

<sub>1901</sub> In this work two distinct  $j_T$  components were extracted for narrow and wide contri-  
<sub>1902</sub> butions using jet reconstruction. RMS values for both components were obtained.  
<sub>1903</sub> The width of the wide component is found to increase for increasing  $p_{T\text{jet}}$ . This  
<sub>1904</sub> is in part explained by the changing kinematical limits when going to higher  $p_{T\text{jet}}$   
<sub>1905</sub> which allows higher  $p_{T\text{track}}$ . Additionally the larger phase space allows stronger  
<sub>1906</sub> parton splitting. The results are qualitatively compatible with previous studies  
<sub>1907</sub> that studied  $j_T$  using two-particle correlations.

## <sup>1908</sup> References

- <sup>1909</sup> [1] ALICE, J. Adam *et al.*, Phys. Rev. **C91**, 064905 (2015), 1412.6828.
- <sup>1910</sup> [2] <https://alice-publications.web.cern.ch/node/3655>, 2018.
- <sup>1911</sup> [3] PHENIX Collaboration, K. Adcox *et al.*, Nucl.Phys. **A757**, 184 (2005), nucl-ex/0410003.
- <sup>1912</sup>
- <sup>1913</sup> [4] STAR Collaboration, J. Adams *et al.*, Nucl.Phys. **A757**, 102 (2005), nucl-ex/0501009.
- <sup>1914</sup>
- <sup>1915</sup> [5] J.-Y. Ollitrault, Phys. Rev. D **46**, 229 (1992).
- <sup>1916</sup> [6] U. Heinz and P. Kolb, Nucl. Phys. **A702**, 269 (2002).
- <sup>1917</sup> [7] E. Shuryak, Prog. Part. Nucl. Phys. **62**, 48 (2009).
- <sup>1918</sup> [8] ATLAS Collaboration, J. Jia, Nucl.Phys.A904-905 **2013**, 421c (2013), 1209.4232.
- <sup>1919</sup>
- <sup>1920</sup> [9] R. A. Lacey *et al.*, (2012), 1207.1886.
- <sup>1921</sup> [10] R. Bjorklund, W. Crandall, B. J. Moyer, and H. York, Phys. Review **77**, 213 (1950).
- <sup>1922</sup>
- <sup>1923</sup> [11] W. Heisenberg, Zeitschrift für Physik **77**, 1 (1932).
- <sup>1924</sup> [12] M. Gell-Mann, Phys. Rev. **125**, 1067 (1962).
- <sup>1925</sup> [13] M. Gell-Mann, Phys. Lett. **8**, 214 (1964).
- <sup>1926</sup> [14] O. Greenberg, Phys. Rev. Lett. **13**, 598 (1964).
- <sup>1927</sup> [15] Crystal Ball Collaboration, D. Williams *et al.*, Phys.Rev. **D38**, 1365 (1988).
- <sup>1928</sup> [16] W. Krolikowski, Nuovo Cim. **A27**, 194 (1975).
- <sup>1929</sup> [17] D. J. Gross and F. Wilczek, Physical Review Letters **30**, 1343 (1973).
- <sup>1930</sup> [18] H. D. Politzer, Physical Review Letters **30**, 1346 (1973).
- <sup>1931</sup> [19] D. J. Gross and F. Wilczek, Physical Review D **8**, 3633 (1973).
- <sup>1932</sup> [20] D. J. Gross and F. Wilczek, Physical Review D **9**, 980 (1974).
- <sup>1933</sup> [21] H. Georgi and H. D. Politzer, Physical Review D **9**, 416 (1974).

- <sup>1934</sup> [22] H. Fritzsch, M. Gell-Mann, and H. Leutwyler, Physics Letters B **47**, 365 (1973).
- <sup>1935</sup>
- <sup>1936</sup> [23] I. Flegel and P. Söding, CERN courier (2004).
- <sup>1937</sup> [24] R. Brandelik *et al.*, Physics Letters B **86**, 243 (1979).
- <sup>1938</sup> [25] J. K. L. MacDonald, Phys. Rev. **43**, 830 (1933).
- <sup>1939</sup> [26] C. Berger *et al.*, Physics Letters B **86**, 418 (1979).
- <sup>1940</sup> [27] J. Collins and M. Perry, Phys. rev. Lett. **34**, 1353 (1975).
- <sup>1941</sup> [28] E. Shuryak, Phys. Reps. **61**, 71 (1980).
- <sup>1942</sup> [29] K. Rajagopal, SLAC Beam Line **31-2**, 9 (2001).
- <sup>1943</sup> [30] P. Kovtun, D. Son, and A. Starinets, Phys.Rev.Lett. **94**, 111601 (2005), hep-th/0405231.
- <sup>1944</sup>
- <sup>1945</sup> [31] R. A. Lacey *et al.*, Phys. Rev. Lett. **98**, 092301 (2007).
- <sup>1946</sup> [32] E. Lofgren, *ACCELERATOR DIVISION ANNUAL REPORTS, 1 JULY 1972 12/31/1974* (, 1975).
- <sup>1947</sup>
- <sup>1948</sup> [33] D. S. Barton, Heavy ion program at bnl: Ags, rhic, in *Proc. 1987 Particle Accelerator Conference, Washington, D.C., March, 1987*, 1987.
- <sup>1949</sup>
- <sup>1950</sup> [34] I. Vitev and M. Gyulassy, Phys.Rev.Lett. **89**, 252301 (2002), hep-ph/0209161.
- <sup>1951</sup>
- <sup>1952</sup> [35] S. Choi and K. S. Lee, Phys. Rev. C **84**, 064905 (2011).
- <sup>1953</sup> [36] A. Kovalenko *et al.*, Status of the nuclotron, in *Proceedings of EPAC Vol. 94*, pp. 161–164, 1994.
- <sup>1954</sup>
- <sup>1955</sup> [37] NA61/SHINE, K. Grebieszkow, PoS **CPOD2013**, 004 (2013).
- <sup>1956</sup> [38] BRAHMS Collaboration, I. Arsene *et al.*, Nucl.Phys. **A757**, 1 (2005), nucl-ex/0410020.
- <sup>1957</sup>
- <sup>1958</sup> [39] B. Back *et al.*, Nucl.Phys. **A757**, 28 (2005), nucl-ex/0410022.
- <sup>1959</sup> [40] S. A. Voloshin, A. M. Poskanzer, and R. Snellings, (2008), 0809.2949.
- <sup>1960</sup> [41] S. A. Voloshin, A. M. Poskanzer, A. Tang, and G. Wang, Phys.Lett. **B659**, 537 (2008), 0708.0800.
- <sup>1961</sup>

- <sup>1962</sup> [42] H. Holopainen, H. Niemi, and K. J. Eskola, Phys.Rev. **C83**, 034901 (2011), 1007.0368.
- <sup>1963</sup>
- <sup>1964</sup> [43] ALICE Collaboration, Phys. Rev. C **88**, 044909 (2013).
- <sup>1965</sup> [44] M. L. Miller, K. Reygers, S. J. Sanders, and P. Steinberg, Ann.Rev.Nucl.Part.Sci. **57**, 205 (2007), nucl-ex/0701025.
- <sup>1966</sup>
- <sup>1967</sup> [45] R. Glauber, Lectures in theoretical physics, 1959.
- <sup>1968</sup> [46] W. Czyż and L. Maximon, Annals of Physics **52**, 59 (1969).
- <sup>1969</sup> [47] A. Białas, M. Bleszyński, and W. Czyż, Nuclear Physics B **111**, 461 (1976).
- <sup>1970</sup> [48] PHENIX Collaboration, S. Afanasiev *et al.*, Phys.Rev. **C80**, 054907 (2009), 0903.4886.
- <sup>1971</sup>
- <sup>1972</sup> [49] J.-Y. Ollitrault, Eur.J.Phys. **29**, 275 (2008), 0708.2433.
- <sup>1973</sup> [50] P. Romatschke, Int.J.Mod.Phys. **E19**, 1 (2010), 0902.3663.
- <sup>1974</sup> [51] L. LD, Izv. Akad. Nauk Ser. Fiz. **17**, 51 (1953).
- <sup>1975</sup> [52] H. Song, S. Bass, and U. W. Heinz, (2013), 1311.0157.
- <sup>1976</sup> [53] H. Niemi, G. Denicol, P. Huovinen, E. Molnar, and D. Rischke, Phys.Rev. **C86**, 014909 (2012), 1203.2452.
- <sup>1977</sup>
- <sup>1978</sup> [54] K. A. *et al.* [ALICE Collaboration], Phys. Rev. Lett **106** (2011), 032301.
- <sup>1979</sup> [55] J.-Y. Ollitrault, Phys.Rev. D **48**, 1132 (1993), hep-ph/9303247.
- <sup>1980</sup> [56] P. Danielewicz and G. Odyniec, Physics Letters B **157**, 146 (1985).
- <sup>1981</sup> [57] P. Danielewicz and M. Gyulassy, Physics Letters B **129**, 283 (1983).
- <sup>1982</sup> [58] T. Abbott *et al.*, Phys. Rev. Lett. **70**, 1393 (1993).
- <sup>1983</sup> [59] S. Voloshin and Y. Zhang, Z.Phys. **C70**, 665 (1996), hep-ph/9407282.
- <sup>1984</sup> [60] E877 Collaboration, J. Barrette *et al.*, Phys.Rev.Lett. **73**, 2532 (1994), hep-ex/9405003.
- <sup>1985</sup>
- <sup>1986</sup> [61] CMS Collaboration, S. Chatrchyan *et al.*, Phys.Rev.Lett. **109**, 022301 (2012), 1204.1850.
- <sup>1987</sup>

- <sub>1988</sub> [62] Y. I. Azimov, Y. L. Dokshitzer, V. A. Khoze, and S. I. Trovan, Zeitschrift für Physik C Particles and Fields **27**, 65 (1985).
- <sub>1990</sub> [63] B. Andersson, G. Gustafson, G. Ingelman, and T. Sjöstrand, Physics Reports **97**, 31 (1983).
- <sub>1992</sub> [64] A. Buckley *et al.*, Phys. Rept. **504**, 145 (2011), 1101.2599.
- <sub>1993</sub> [65] M. Bahr *et al.*, Eur. Phys. J. **C58**, 639 (2008), 0803.0883.
- <sub>1994</sub> [66] ALICE Collaboration, K. Aamodt *et al.*, Phys.Lett. **B696**, 30 (2011), 1012.1004.
- <sub>1996</sub> [67] WA98 Collaboration, M. Aggarwal *et al.*, Eur.Phys.J. **C23**, 225 (2002), nucl-ex/0108006.
- <sub>1998</sub> [68] D. G. d'Enterria, Phys.Lett. **B596**, 32 (2004), nucl-ex/0403055.
- <sub>1999</sub> [69] PHENIX Collaboration, A. Adare *et al.*, Phys.Rev.Lett. **101**, 232301 (2008), 0801.4020.
- <sub>2001</sub> [70] STAR Collaboration, J. Adams *et al.*, Phys.Rev.Lett. **91**, 172302 (2003), nucl-ex/0305015.
- <sub>2003</sub> [71] A. Dainese, C. Loizides, and G. Paic, Eur.Phys.J. **C38**, 461 (2005), hep-ph/0406201.
- <sub>2005</sub> [72] I. Vitev, J.Phys. **G30**, S791 (2004), hep-ph/0403089.
- <sub>2006</sub> [73] C. A. Salgado and U. A. Wiedemann, Phys.Rev. **D68**, 014008 (2003), hep-ph/0302184.
- <sub>2008</sub> [74] N. Armesto, A. Dainese, C. A. Salgado, and U. A. Wiedemann, Phys.Rev. **D71**, 054027 (2005), hep-ph/0501225.
- <sub>2010</sub> [75] T. Renk, H. Holopainen, R. Paatelainen, and K. J. Eskola, Phys.Rev. **C84**, 014906 (2011), 1103.5308.
- <sub>2012</sub> [76] CMS Collaboration, S. Chatrchyan *et al.*, Eur.Phys.J. **C72**, 1945 (2012), 1202.2554.
- <sub>2014</sub> [77] PHENIX Collaboration, S. Afanasiev *et al.*, Phys. Rev. C **80**, 054907 (2009).
- <sub>2015</sub> [78] ALICE Collaboration, K. Aamodt *et al.*, Phys.Rev.Lett. **108**, 092301 (2012), 1110.0121.

- 2017 [79] R. Baier, Y. L. Dokshitzer, A. H. Mueller, S. Peigne, and D. Schiff, Nucl.  
2018 Phys. **B484**, 265 (1997), hep-ph/9608322.
- 2019 [80] W. H. H. Bethe and, Proc.Roy.Soc.Lond. **A146** (1934).
- 2020 [81] L. D. Landau and I. Pomeranchuk, Dokl. Akad. Nauk Ser. Fiz. **92**, 535  
2021 (1953).
- 2022 [82] A. B. Migdal, Phys. Rev. **103**, 1811 (1956).
- 2023 [83] P. Bosted *et al.*, Quantum-mechanical suppression of bremsstrahlung\*, 1993.
- 2024 [84] A. Majumder and M. Van Leeuwen, Prog.Part.Nucl.Phys. **A66**, 41 (2011),  
2025 1002.2206.
- 2026 [85] F. Dominguez, C. Marquet, A. Mueller, B. Wu, and B.-W. Xiao, Nucl.Phys.  
2027 **A811**, 197 (2008), 0803.3234.
- 2028 [86] M. Gyulassy, P. Levai, and I. Vitev, Nucl.Phys. **B571**, 197 (2000), hep-  
2029 ph/9907461.
- 2030 [87] U. A. Wiedemann, Nucl.Phys. **B588**, 303 (2000), hep-ph/0005129.
- 2031 [88] P. B. Arnold, G. D. Moore, and L. G. Yaffe, JHEP **0112**, 009 (2001), hep-  
2032 ph/0111107.
- 2033 [89] X.-N. Wang and X.-f. Guo, Nucl.Phys. **A696**, 788 (2001), hep-ph/0102230.
- 2034 [90] T. Sjostrand, S. Mrenna, and P. Z. Skands, Comput.Phys.Commun. **178**,  
2035 852 (2008), 0710.3820.
- 2036 [91] I. Lokhtin and A. Snigirev, Eur.Phys.J. **C45**, 211 (2006), hep-ph/0506189.
- 2037 [92] N. Armesto, L. Cunqueiro, and C. A. Salgado, Nucl.Phys. **A830**, 271C  
2038 (2009), 0907.4706.
- 2039 [93] K. Zapp, G. Ingelman, J. Rathsman, J. Stachel, and U. A. Wiedemann,  
2040 Eur.Phys.J. **C60**, 617 (2009), 0804.3568.
- 2041 [94] T. Renk, Phys.Rev. **C79**, 054906 (2009), 0901.2818.
- 2042 [95] A. Kurkela and U. A. Wiedemann, Phys. Lett. **B740**, 172 (2015), 1407.0293.
- 2043 [96] J. L. Nagle and W. A. Zajc, Ann. Rev. Nucl. Part. Sci. **68**, 211 (2018),  
2044 1801.03477.
- 2045 [97] E735, T. Alexopoulos *et al.*, Phys. Rev. **D48**, 984 (1993).

- 2046 [98] MiniMax, T. C. Brooks *et al.*, Phys. Rev. **D61**, 032003 (2000), hep-ex/9906026.
- 2047
- 2048 [99] C. Shen, Z. Qiu, and U. Heinz, Phys. Rev. **C92**, 014901 (2015), 1502.04636.
- 2049 [100] PHENIX, A. Adare *et al.*, Phys. Rev. **C94**, 064901 (2016), 1509.07758.
- 2050 [101] C. A. Salgado and J. P. Wessels, Ann. Rev. Nucl. Part. Sci. **66**, 449 (2016).
- 2051 [102] M. Gyulassy, I. Vitev, X.-N. Wang, and B.-W. Zhang, p. 123 (2003), nucl-th/0302077.
- 2052
- 2053 [103] E. Norbeck, K. Šafařík, and P. A. Steinberg, Annual Review of Nuclear and Particle Science **64**, 383 (2014), <https://doi.org/10.1146/annurev-nucl-102912-144532>.
- 2054
- 2055 [104] A. Accardi, F. Arleo, W. K. Brooks, D. D'Enterria, and V. Muccifora, Riv. Nuovo Cim. **32**, 439 (2010), 0907.3534.
- 2056
- 2057 [105] 2019.
- 2058
- 2059 [106] T. ALICE Collaboration *et al.*, Journal of Instrumentation **3**, S08002 (2008).
- 2060 [107] The ALICE Collaboration, Report No. CERN-LHCC-2013-020. ALICE-TDR-016, 2013 (unpublished).
- 2061
- 2062 [108] for the ALICE, C. Zampolli, Particle Identification with the ALICE detector at the LHC, in *Proceedings, PLHC2012: Physics at the LHC 2012 (PLHC2012): Vancouver, BC, Canada, June 4-9, 2012*, 2012, 1209.5637.
- 2063
- 2064
- 2065 [109] ALICE, G. Dellacasa *et al.*, (1999).
- 2066 [110] J. Allen *et al.*, Report No. CERN-LHCC-2010-011. ALICE-TDR-14-add-1, 2010 (unpublished).
- 2067
- 2068 [111] ALICE, K. Aamodt *et al.*, JINST **3**, S08002 (2008).
- 2069 [112] ALICE, B. B. Abelev *et al.*, Int. J. Mod. Phys. **A29**, 1430044 (2014), 1402.4476.
- 2070
- 2071 [113] ALICE, K. Aamodt *et al.*, JINST **5**, P03003 (2010), 1001.0502.
- 2072 [114] J. Alme *et al.*, Nucl. Instrum. Meth. **A622**, 316 (2010), 1001.1950.
- 2073 [115] ALICE, B. Abelev *et al.*, JHEP **03**, 053 (2012), 1201.2423.
- 2074 [116] ALICE, P. Cortese *et al.*, (2008).

- 2075 [117] ALICE Collaboration, *Technical Design Report on Forward Detectors:*  
2076 *FMD, T0 and V0*, 2004.
- 2077 [118] ALICE, B. Abelev *et al.*, Phys. Lett. **B719**, 29 (2013), 1212.2001.
- 2078 [119] M. Cacciari, G. P. Salam, and G. Soyez, Eur. Phys. J. **C72**, 1896 (2012),  
2079 1111.6097.
- 2080 [120] M. Cacciari, G. P. Salam, and G. Soyez, JHEP **04**, 063 (2008), 0802.1189.
- 2081 [121] T. Sjöstrand, S. Mrenna, and P. Z. Skands, Comput. Phys. Commun. **178**,  
2082 852 (2008), 0710.3820.
- 2083 [122] Roounfold: Root unfolding framework, [http://hepunx.rl.ac.uk/~adye/  
2084 software/unfold/RooUnfold.html](http://hepunx.rl.ac.uk/~adye/software/unfold/RooUnfold.html), 2013.
- 2085 [123] CMS, S. Chatrchyan *et al.*, Phys. Rev. **D90**, 072006 (2014), 1406.0324.
- 2086 [124] M. Dasgupta, L. Magnea, and G. P. Salam, JHEP **02**, 055 (2008), 0712.3014.